FURNACES WITH MULTIPLE FLAMELESS COMBUSTION BURNERS

Bart Danon

Furnaces with multiple flameless combustion burners

Bart Danon

Furnaces with multiple flameless combustion burners

Proefschrift

ter verkrijging van de graad van doctor
aan de Technische Universiteit Delft,
op gezag van de Rector Magnificus prof.ir. K.Ch.A.M. Luyben,
voorzitter van het College van Promoties,
in het openbaar te verdedigen op vrijdag 19 augustus 2011 om 15:00 uur
door
Bart DANON
ingenieur in de Chemische Technologie
geboren te Delft.

Dit proefschrift is goedgekeurd door de promotoren:

Prof.dr. D.J.E.M. Roekaerts
Prof.dr.ir. B.J. Boersma

Copromotor: Dr.ir. W. de Jong

Samenstelling promotiecommissie:

Rector Magnificus	voorzitter
Prof.dr. D.J.E.M. Roekaerts	Technische Universiteit Delft, promotor
Prof.dr.ir. B.J. Boersma	Technische Universiteit Delft, promotor
Dr.ir. W. de Jong	Technische Universiteit Delft, copromotor
Prof.dr.ir. T.H. van der Meer	Universiteit Twente
Prof.dr.ir. B. Merci	Universiteit Gent
Prof.dr.ir. C. Vuik	Technische Universiteit Delft
Dr.ir. P. Pronk	Tata Steel
Prof.dr.ir. C.R. Kleijn	Technische Universiteit Delft, reservelid

Published and distributed by: Bart Danon
Printed by: Gildeprint Drukkerijen

ISBN: 978-94-6108-199-5

Printed in the Netherlands

Aan de zeven personen die mij op deze wereld het meest dierbaar zijn:
mijn ouders, broer, vriendin en beste vrienden

Summary

Furnaces with multiple flameless combustion burners

In this thesis three different combustion systems, equipped with either a single or multiple flameless combustion burner(s), are discussed. All these setups were investigated both experimentally and numerically, i.e., using Computational Fluid Dynamics (CFD) simulations.

Flameless combustion is a combustion technology capable of accomplishing the combination of high energy efficiency (by preheating of the combustion air) and low emissions, especially nitrogen oxides (NO_x). These high combustion air preheat temperatures normally account for increased thermal formation of NO_x, however, in flameless combustion, by delayed mixing of the fuel and oxidizer and high internal flue gas recirculation, the rates of these reactions are decreased. Nitrogen oxide plays a key role in acid rain formation and the generation of photochemical smog.

The first setup that has been investigated is a furnace equipped with two regenerative flameless combustion burner pairs, with a thermal power of 100 kW_{th} each, located at the laboratories of Kungliga Tekniska Högskolan (KTH) in Stockholm, Sweden (*Chapter 4*). The objective of this study is to investigate the performance of the furnace operating in two different firing modes, parallel and staggered. The furnace performance is defined as the energy efficiency and the NO emissions. Experimental results show that for parallel firing mode both the efficiency was higher and the NO emissions were lower compared to staggered firing mode. With the use of the CFD simulations, it was shown that in parallel mode the radiative heat transfer was higher due to formation of a larger zone with gases with improved radiative properties and that higher velocities along the cooling tubes, due to lower momentum destruction, led to higher convective heat transfer. Both of these heat transfer methods contributed to the higher energy efficiency in parallel firing mode. Additionally, the lower formation of NO emissions in parallel firing mode was due to the fact that the low-momentum fuel jets merged slower with the high-momentum combustion air jets, resulting in more internal flue gas recirculation and a less intense combustion zone. Moreover, it was found that NO_x was formed via the thermal and N_2O intermediate pathways. No prompt NO was formed, while the reburning pathway resulted

in a reduction of the total NO emissions.

The second setup is a 300 kW_{th} furnace equipped with three pairs of regenerative flameless combustion burners, located at Delft University of Technology (DUT) in the Netherlands (*Chapter 5*). An experimental parametric study was performed, varying the positions of the burners in the furnace (the burner configuration), the firing mode (parallel and staggered), the excess air ratio and the cycle time, with the objective to optimize the furnace performance. Since similar trends in the furnace performance, as for the furnace at KTH, comparing parallel and staggered firing mode, were observed, staggered mode was exempted from further analysis. Additionally, one of the five investigated burner configurations has also been exempted due to a significant lower energy efficiency compared to the other configurations. The experimental results show that the burner positioning and the cycle time had a significant influence on the temperature inside the regenerators, and thus on the preheat temperature of the combustion air. This temperature turned out to be important regarding the CO emissions. Furthermore, it was found that comparing different cases firing in flameless mode, an improved temperature uniformity in the furnace was not reflected by a higher energy efficiency. Finally, a horizontal setup of the firing burners (the three firing burners positioned in a horizontal row) improved the energy efficiency at similar temperature uniformities.

Steady CFD simulations have been performed for this furnace for four different burner configurations firing in parallel mode (*Chapter 6*). During the careful selection of the set of physical models to be used, it was found that, due to relatively low Reynolds numbers in the cooling air flow in the annulus of the cooling tubes, predictions of the heat extraction rates of these cooling tubes were improved by treating the flow in the cooling tubes as laminar. Furthermore, the applied error tolerance of the ISAT procedure was insufficient for accurate species concentration predictions, however, based on analysis of the main species concentrations in the flue gas, this inaccuracy did not influence the overall predictions. It was possible to explain the most important results of the experimental study using the CFD simulations. In the first place, it was found that a recirculation zone between the upper firing burners and the stack in two configurations resulted in a smaller fraction of the flue gases leaving the furnace via the stack compared to the other two configurations. Thus, a larger fraction of the flue gas left the furnace via the regenerating burners, which resulted in higher preheat temperatures of the combustion air. Secondly, the experimentally observed differences in the temperature uniformity between the four configurations could be explained by the presence of less or more pronounced recirculation zones, the latter leading to higher temperature uniformities in the furnace. Finally, it was confirmed that the jets of the burners showed similar merging behaviour for different burner configurations, leading to similar NO emissions, a trend that was also observed in the experiments.

The third setup is a prototype flameless combustion gas turbine combustor (*Chapter*

7). The combustor was fired with various Low Calorific Value (LCV) gases. The influence of several parameters (the fuel composition, the outlet temperature and the inlet nozzle diameter) on the CO and NO emissions has been investigated. In the first place, it was shown that this prototype flameless combustion gas turbine combustor could be operated in flameless mode firing the LCV gases. Moreover, for both pollutants ultra-low emissions (single-digit) have been achieved. In the CFD simulations, different turbulence models and chemistry mechanisms have been compared, leading to a set with models which gave the best results. Comparing the measured and predicted axial temperature profiles in the combustor, it was concluded that the observed discrepancies were within the range of uncertainty in what are optimal values of the model constants. From NO calculations, ultra-low emission combustion was confirmed. Also, it was found that 90% of the NO was formed via the N_2O path, and the remaining 10% via the thermal pathway. No prompt NO was formed, a trend also observed for the KTH furnace.

In conclusion, important knowledge on the behaviour of furnaces equipped with multiple flameless combustion burners has been attained. Especially, the influence on the furnace performance of the firing configuration of the burners and the burner positioning in the furnace will contribute to more successful (industrial) application of this combustion technology in the future. Recommendations for the installation of flameless combustion burners in large industrial-scale furnaces have been proposed. Finally, the shown possibility of firing a (prototype) gas turbine combustor with low calorific value gases in flameless mode, enables the utilization of biomass derived gaseous fuels in existing equipment.

Samenvatting

Fornuizen met meerdere vlamloze verbranding branders

In dit proefschrift worden drie verschillende verbrandingssystemen, uitgerust met een enkele of meerdere vlamloze verbranding brander(s), besproken. Al deze opstellingen zijn zowel experimenteel als numeriek, te weten, met Computational Fluid Dynamics (CFD) simulaties, onderzocht.

Vlamloze verbranding is een verbrandingstechniek die in staat is de combinatie van hoge energie efficiënties (door middel van het voorverwarmen van de verbrandingslucht) en lage uitstoot van verontreinigende stoffen, in het bijzonder van stikstofoxides (NO_x) te realiseren. Deze hoge voorverwarmingstemperaturen van de verbrandingslucht zorgen normaal gesproken voor een toename van de thermische vorming van NO_x, echter met vlamloze verbranding wordt, door het uitgesteld mengen van de brandstof en het oxidatiemiddel en hoge interne rookgas recirculatie, de snelheid van deze reacties verlaagd. Stikstofoxides spelen een belangrijke rol in de vorming van zure regen en in het ontstaan van fotochemisch smog.

De eerste onderzochte opstelling is een fornuis met twee regeneratieve brander paren opererend in het vlamloze verbrandingsregime, met een thermisch vermogen van 100 kW_{th} elk, gesitueerd in het laboratorium van de Kungliga Tekniska Högskolan (KTH) in Stockholm, Zweden (*Hoofdstuk 4*). Het doel van deze studie was het onderzoeken van de prestatie van het fornuis opererend in twee verschillende operatiemodi, parallel en zigzagsgewijs. De prestatie van het fornuis is gedefinieerd als de energie efficiëntie en de uitstoot van NO. De experimentele resultaten laten zien dat in parallelle operatiemodus zowel de energie efficiëntie hoger is als dat de NO uitstoot lager is, vergeleken met de zigzagsgewijze operatiemodus. Met behulp van de CFD simulaties is aangetoond dat in parallelle operatiemodus de warmteoverdracht door straling hoger was ten gevolge van de vorming van grotere zones van gassen met verbeterde stralings eigenschappen en dat hogere snelheden langs de koelbuizen, ten gevolge van lagere impuls vernietiging, resulteerde in hogere convectieve warmteoverdracht. Beide van deze warmteoverdracht mechanismen droegen bij aan de hogere energie efficiëntie in parallelle operatiemodus. Verder bleek de lagere NO uitstoot in parallelle operatiemodus een gevolg van het feit dat

de jets met relatief lage impuls van de brandstof langzamer samenvloeiden met de jets met hogere impuls van de verbrandingslucht, resulterend in meer interne rookgas recirculatie en een minder intensieve verbrandingszone. Verder is gebleken dat de NO_x zowel via het thermische als via het N_2O tussenproduct mechanisme werd gevormd. Er werd geen prompt NO gevormd, terwijl het herverbrandingsmechanisme voor een afname van de totale NO uitstoot zorgde.

De tweede opstelling is een 300 kW_{th} fornuis uitgerust met drie paar regeneratieve vlamloze verbranding branders, gestationeerd bij de Technische Universiteit Delft (TUD) in Nederland (*Hoofdstuk 5*). Een experimentele parametrische studie is uitgevoerd door het variëren van de posities van de branders (de branderconfiguratie), de operatiemodus (parallel en zigzagsgewijs), de luchtovermaatfactor en de cyclus tijd, met het doel om de fornuisprestatie te optimaliseren. Omdat soortgelijke tendensen in de fornuisprestatie, als geobserveerd in het KTH fornuis, bij het vergelijken tussen parallelle en zigzagsgewijze operatiemodus, waar werden genomen, is de zigzagsgewijze operatiemodus weggelaten uit de gedetailleerde analyse. Verder is één van de vijf onderzochte branderconfiguraties ook uitgesloten, vanwege haar significant lagere energie efficiëntie vergeleken met de andere branderconfiguraties. De experimentele resultaten laten zien dat de branderconfiguratie en de cyclus tijd een significante invloed hadden op de temperatuur in de regeneratoren, en zodoende op de voorverwarmingstemperatuur van de verbrandingslucht. Deze temperatuur bleek belangrijk te zijn voor de CO uitstoot. Voorts is gebleken dat, wanneer men verschillende experimenten onder vlamloze verbranding condities vergelijkt, een verbeterde temperatuursuniformiteit niet weerspiegeld werd door een hogere energie efficiëntie. Ten slotte verbeterde een horizontale opstelling van de opererende branders (dat wil zeggen de drie opererende branders gepositioneerd op een rij) verbeterde de energie efficiëntie bij gelijke temperatuursuniformiteit.

Stationaire CFD simulaties zijn uitgevoerd voor dit fornuis voor vier verschillende brander configuraties in parallelle operatiemodus (*Hoofdstuk 6*). Tijdens de zorgvuldige selectie van de fysische modellen bleek dat, aangezien de Reynolds getallen in de koellucht stroom in de annulus van de koelbuizen relatief laag waren, de voorspellingen van de warmteonttrekking van deze koelbuizen verbeterd werden door de stroom in de koelbuizen als laminair te beschouwen. Verder was de toegepaste fout tolerantie voor de ISAT procedure inadequaat voor nauwkeurige concentratie voorspellingen. Het bleek echter dat, gebaseerd op de analyse van de belangrijkste concentraties in het rookgas, deze onnauwkeurigheid geen invloed had op de algehele voorspellingen. Het was mogelijk de belangrijkste resultaten van de experimentele studie te verklaren met behulp van de CFD simulaties. In de eerste plaats bleek dat een recirculatie zone tussen de bovenste branders en de schoorsteen in twee van de configuraties resulteerde in een kleinere fractie van de rookgassen die het fornuis verliet via de schoorsteen, vergeleken met de twee andere configuraties. Een groter deel van de rookgassen verliet het fornuis dus via de regeneratoren,

wat resulteerde in hogere voorverwarmingstemperaturen van de verbrandingslucht. Ten tweede konden de in de experimenten geobserveerde verschillen in de temperatuursuniformiteit tussen de vier configuraties uitgelegd worden door de aanwezigheid van minder of meer duidelijke recirculatiezones, waarbij de laatstgenoemde resulteerde in hogere temperatuursuniformiteiten in het fornuis. Ten slotte werd bevestigd dat de branders gelijksoortig samenvloeiingsgedrag vertoonden voor de verschillende branderconfiguraties, resulterend in vergelijkbare NO uitstoot; een tendens die ook in de experimenten is waargenomen.

De derde opstelling is een prototype vlamloze verbranding gas turbine verbrander (*Hoofdstuk 7*). In de verbrander werden verschillende gassen met lage calorische waarden (LCW) gestookt. De invloed van drie verschillende parameters (de brandstofsamenstelling, de uitlaattemperatuur en de diameter van de inlaatmondstukken) op de CO en NO uitstoot zijn onderzocht. In de eerste plaats werd aangetoond dat deze prototype vlamloze verbranding gas turbine verbrander in vlamloze modus stabiel kon branden op LCW gassen. Bovendien werden voor beide luchtverontreinigende stoffen ultra-lage uitstoot (enkel-cijferige waarden) bereikt. In de CFD simulaties zijn verschillende turbulentie modellen en chemie mechanismen vergeleken, wat leidde tot een set modellen die de beste resultaten gaf. De gemeten en voorspelde axiale temperatuursprofielen in de verbrander zijn vergeleken en er werd geconcludeerd dat de waargenomen discrepanties binnen de marge van onzekerheid vallen van wat de optimale waardes van de model constanten zijn. In de NO berekeningen werd de ultra-lage uitstoot bevestigd. Verder bleek dat 90% van de NO gevormd werd via het N_2O tussenproduct mechanisme en de overgebleven 10% via het thermische mechanisme. Geen prompt NO werd gevormd, een tendens die ook werd waargenomen in het KTH fornuis.

Concluderend, belangrijke kennis over het gedrag van fornuizen met meerdere vlamloze verbranding branders is verkregen. In het bijzonder zal de invloed op de fornuisprestatie van de operatiemodus van de branders en de brander positionering in het fornuis bijdragen aan een succesvolle (industriële) toepassing van deze verbrandingstechniek in de toekomst. Aanbevelingen voor de installatie van vlamloze verbranding branders in grootschalige industriële fornuizen zijn voorgesteld. Bovendien maken in de toekomst de thans bewezen mogelijkheden om een (prototype) gas turbine verbrander te opereren met gassen met een laag calorische waarde in vlamloze modus het gebruik van biomassa-afgeleide gasvormige brandstoffen in bestaande opstellingen mogelijk.

Prologue

Di, coeptis (...) adspirate meis
(*Gods, breath over my undertakings*, Ovidius, Met.I.2-3)

Before you lay the excrement of five years of work, a period which has been a great learning experience for me. Besides the specific knowledge I gained in the field of combustion, the greatest lessons were on the level of personal efficiency, perseverance and theoretical analysis. Furthermore, the time spend at the university as an institution has confronted me with great possibilities and opportunities for a possible career.

This all has been made possible mainly by two persons: Dirk Roekaerts and Wiebren de Jong. In the first place, their endless confidence allowed me to exploit both my academic and personal skills extensively. My thanks for them letting me work in part-time, allowing me to follow an intensive acting curriculum in Amsterdam, are beyond endless. Furthermore, both Dirk en Wiebren encouraged me over the years to adopt a (critical) scientific attitude, which will be a blessing for the rest of my life.

Also, in the last three years I worked intensively together with Teo (Eun-Seong) Cho. The cooperation has been an enormous pleasure, both on the personal as on the professional level, for which I thank him enormously. I wouldn't have come so far as it was not for Teo.

Many persons of the Energy Technology section have contributed either consciously or unconsciously to the realization of this thesis. To all the secretaries, the (mechanical) supporting staff, my office mates and my fellow PhD students I owe my gratitude. In specific, I would like to express my gratitude to Helma Duijndam-Nieuwpoort, Marcin Siedlecki and Jan van Os. These three persons not only helped me whenever I was in need of help, but also managed to conjure a smile on my face whenever I met them. Thank you for these smiles. Voglio ringraziare Mattia per condividere l'ufficio con me e per tutte le lezioni d'italiano. Moreover, there are several other individuals whom I would like to thank in specific for many different reasons: Joachim Wünning, Francesco Ferioli, Daniel Vaz, Luis Arteaga Mendez, Artur Swiderski, Weihong Yang, Duco Bosma, Jasper Ruijgrok, Tjibbe van Dijk, Bert van der Velden, Bart Merci, Karel Laureys, Jim Kok, Peter Hoppesteyn, Luuk Thielen, Erik Heeres and Buana Girisuta. Thank you all!

I have experienced the user committee of my project as a very useful technical framework. I would like to thank all the members of this committee. Also, the institutions that have provided the financial means for the project and my research I would like to thank. These are the Dutch Technology Foundation (STW), the Dutch Flame Foundation (NVV), the European Commission within the sixth framework (project BioPro) and the European Union in the framework of the SUSPOWER project.

However, doing an PhD is not merely a scientific undertaking; the people that coloured my life have also contributed in this way to my work as a scientist. In the first place my parents, whom I would like to thank for making me and for making me the person that I am today. Dank jullie wel, lieve pap en mam! Furthermore, my brother, who has been a great source of inspiration for the path of life that I walk today. My misses, who has completed the puzzle. Then, my closest friends David, Maarten and Pieter. Apart from all the wonderful times we had, have and will have, they have taught me to laugh rather than to cry about ones miseries. It helps. Also many thanks go to my fellow students at de Trap and all the members of improvisation troupe Geen Kunst, who cheered up my life in Delft enormously. For all the Matrici, Singin' viva Matrix. And for my roomies of HBU, ui ui ui! Finally, a cheesy thanks goes to Martijn.

Cui dono lepidum novum libellum?
(*Whom I give this nice new booklet?*, Catullus, Carm.I.1)
To you.

Bart Danon
August 2011

Contents

Chapter 1

Introduction

1.1 Background

Fire has been an important phenomenon throughout human (pre)history. It was not a human invention but humans over time learned mastering and applying it for many purposes, such as heating, cooking, lighting, forging, to name a few. Nowadays, many of these applications of fire (or combustion) are still in use both domestically and industrially. In this thesis the focus is on the industrial application of combustion. Many sectors of modern industry, e.g., electricity generation, steel and glass making, crude oil refining, apply combustion on a large scale and together they use the majority of the total natural energy resources. One particular application of combustion, i.e., the heating of industrial process furnaces, is of special interest here.

Alongside the evolution of the usage of combustion, research in combustion technologies has also been developing over the recent centuries. Especially, over the last decades an increasing interest has been developed worldwide for improving combustion technologies. This development can be roughly split into two periods.

In the first period, directly after the energy crises of the seventies and early eighties of the past century, increasing the energy efficiency was the focus. Combustion engineers improved the energy efficiency by recycling heat from the hot flue gases to the combustion air using heat exchangers. At first, continuous heat exchangers, or recuperators, were mainly used. Later, regenerative heat exchange was applied, where the exchange of heat is achieved by alternately leading the hot flue gas and the cold combustion air over a ceramic heat exchanger, or regenerator. The difference between recuperators and regenerators is thus the method of heat recovery and not a property of the heat exchanger itself. With regenerative heat exchange even higher heat recovery rates can be achieved [1, 2]. Reduction in fuel requirements with regenerative combustion have been reported up to around 30% compared to conventional combustion, and hence similar reductions in carbon dioxide emissions [3, 4, 5].

However, it soon turned out that systems with these high heat recirculation ratios also emitted relatively high concentrations of nitric oxide (NO) and nitrous oxide (NO_2), together abbreviated as NO_x. When these NO_x molecules are released in the air, they may be converted in the presence of oxygen and water to nitric acids (HNO_3). Nitric acids have been implicated in acid rain. The increase in the NO_x emissions for regenerative combustion are due to increased flame temperatures caused by the higher combustion air preheat temperatures, which lead to increased NO_x production via the thermal pathway [6]. Thus, in the second period, roughly from the mid-eighties, when environmental laws on NO_x emissions were getting more stringent, low-NO_x combustion technologies became increasingly important for industrials and combustion researchers. Various combustion methods combining high efficiency and low pollution emissions were developed in these years, e.g., re-burning, oxy-fuel or staged combustion [7]. In the early nineties, a new incentive, i.e., flameless combustion, was among such new combustion technologies [5, 8].

The flameless combustion technique potentially offers enormous advantages compared to conventional combustion methods and even compared to other modern high-efficiency and low-emission combustion technologies. It combines the advantage of high energy efficiency of regenerative combustion with very low NO_x emissions. For that reason, flameless combustion has already been applied, on a small scale, in the industry [9, 10]. Nowadays, additional fundamental and applied research on the behaviour of flameless combustion is needed, so it may become the universally preferred mode of combustion in industrial furnaces in the near future.

1.2 Flameless combustion

Flameless combustion is achieved by separately injecting the fuel and combustion air with high-momentum in a hot and confined environment, e.g., a furnace. In this way, the comburant jets entrain large quantities of the surrounding (inert and hot) flue gases before they mix with each other, as schematically presented Figure 1.1. The strain rates in the high momentum jets are very high, and thus flame extinction would be expected. Therefore, to ensure stable combustion, the temperature of the surroundings in which the comburants are injected should be higher than the self-ignition temperature of the fuel/air mixture.

It is stressed here that the temperature of the surroundings (i.e. the flue gases in the furnace) should be higher than the self-ignition temperature and not the temperature of the preheated combustion air. This is shown in Figure 1.2, where the CO and NO emissions are plotted during the transition of three burners in a furnace changing from flame to flameless firing mode (see for more details Chapter 2). A sampling period of 300 seconds is presented, with the switch to flameless combustion at t = 0 s. The burners in

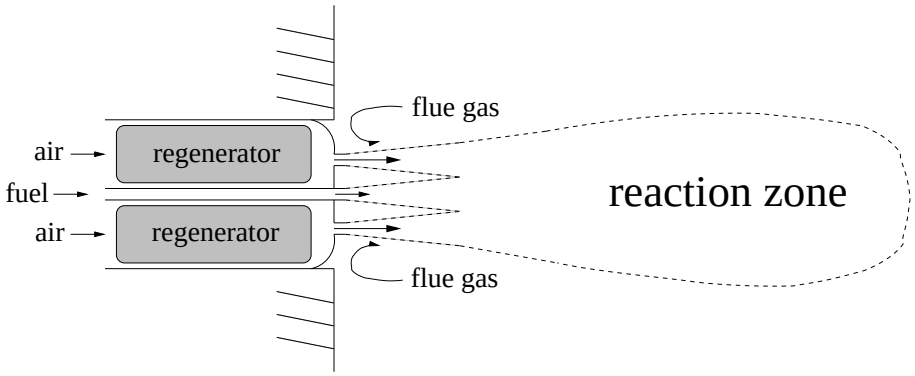

Figure 1.1: Schematic representation of the flameless combustion technique principle.

this system switch automatically to flameless mode at a furnace temperature of 850°C, which is above the self-ignition temperature of the used Dutch Natural Gas and air mixture. At this furnace temperature, the temperature of the preheated combustion air is not yet above the self-ignition temperature (it is around 800°C). However, flameless combustion is achieved, which can be concluded from the drastic decrease in especially the NO emissions after t = 0 s. Moreover, Kumar et al. [11] succeeded in firing a burner in flameless combustion mode using non-preheated combustion air. They concluded that the main requirement for achieving flameless combustion is high recirculation ratios. Also other researchers stressed the importance of the aerodynamic properties of the comburant jets as responsible for the establishment of flameless combustion [12, 13].

The advantages of flameless combustion concerning the main gaseous emissions are also observed in Figure 1.2: both the CO and NO emissions are drastically reduced after t = 0 s. In Chapter 5, where more experimental results of this furnace are presented, it is shown that also at higher furnace temperatures (around 1050°C) and higher combustion air preheat temperatures (around 900°C) these emissions remain relatively low (between 20 and 40 $ppm_v@3\%O_2$, dry for both CO and NO). The observed peaks in the CO concentration are due to the operation dynamics of the on-line gas analyzer.

The decrease in NO emissions is due to the decrease of the maximum (peak) temperatures in the reaction zones. These decreased peak temperatures have been measured by various researchers [14, 15]. Due to these lower peak temperatures, the formation of NO via the thermal pathway is reduced, since the reactions of this mechanism take place at relatively high temperatures [6, 16].

The decrease in the peak temperatures is attributed to the formation of an enlarged reaction zone in flameless combustion, which have been visualized by various researchers by means of measured OH radical concentrations [14, 17, 18]. In this enlarged reaction zone the oxygen concentrations are lower, which is a result of the entrainment of the inert flue gases by the high-momentum jets. Because of these lower oxygen concentrations,

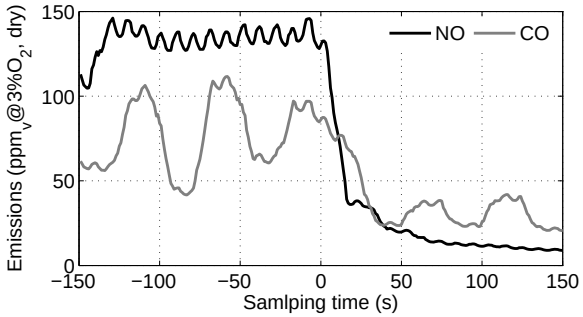

Figure 1.2: Concentrations of CO and NO (ppm_v@3%O_2, dry) in the flue gas of a furnace with three burners changing from flame to flameless firing mode at t = 0 s at a furnace temperature of 850°C.

the combustion reactions are slower than for conventional combustion techniques. Furthermore, the heat generated by the combustion reactions is now divided over more mass, i.e., the mass of the comburant jets and their entrained flue gases. Another advantage of a more distributed reaction zone is more uniform heat transfer rates in the furnace [19].

Finally, Wünning and Wünning performed sound level measurements, reporting that flameless combustion resulted in a significant reduction in noise levels compared to conventional combustion [8].

1.3 Misnomers

The term 'flameless combustion' might need some additional explanation here. Many different misnomers have been proposed in the past few decades for the combustion technique discussed in this thesis. Why has the term 'flameless combustion' been chosen in this thesis? In this section the most widely used misnomers are discussed.

Flameless oxidation (FLOX) was proposed by Wünning and Wünning [8]. This name is close to the one chosen here, but there is one large disadvantage of the name 'flameless oxidation'. This regards the term 'oxidation'. Combustion reactions are indeed oxidation reactions, however, not all oxidation reactions are combustion reactions. Thus, a process as rusting (oxidation of a metal) would be the most obvious 'flameless oxidation' process, i.e., an oxidation reaction without the appearance of a flame.

The name 'excess enthalpy combustion' (EEC) is originally derived from publications of Weinberg in the seventies [20]. Here the word 'excess' is troublesome, it is a comparative, indicating situation A exceeding situation B. However, the comburant jets of a furnace equipped with conventional regenerative burners will have similar enthalpy contents. But the burners are not necessarily firing in flameless combustion mode.

A very widespread name is 'high temperature air combustion' (HiTAC), proposed in Japan, among others by Tsuji et al. [5]. This name is focusing on the fact that this technique can combine high combustion air preheat temperatures with low NO_x emissions, which is indeed an important achievement of the flameless combustion technique. However, as has been stated before, a high preheat temperature of the combustion air is not required to achieve flameless combustion.

Then, 'medium or intense low-oxygen dilution' (MILD) combustion was proposed by Cavaliere et al. [21]. This name is rather confusing; is it 'medium' or 'intense'? What is 'medium' or 'intense'; is it, for instance, 'intense low-oxygen' or 'intense dilution'? In other words, are the adjectives 'medium' and 'intense' related to 'low-oxygen' or to 'dilution'? Actually, the reader should be familiar with the combustion technique to be able to answer these questions.

The last name discussed here is 'colorless combustion' proposed by Gupta et al. [22]. Since the flame is invisible, it is also colorless, indeed. However, the term is not distinctive, there are many other 'non-properties' of this combustion technique.

Additionally, the word 'flameless' of 'flameless combustion' needs to be elucidated a bit further here since it has been the topic of controversies. This requires a specific definition of the term 'flame'. The on-line Cambridge dictionary describes the term 'flame' as 'burning gas (from something on fire) which produces usually yellow light' [23]. The on-line Merriam-Webster dictionary defines a 'flame' as 'the glowing gaseous part of a fire' [24]. Indeed, the term 'flame' refers to the light (or glowing) produced by the reactions and not (merely) to the reactions itself.

In conclusion, this combustion technique can best be called 'flameless combustion', since its main distinctive property is the fact that it emits very low levels of light, visible to the human eye, during the combustion reactions.

1.4 Thesis objectives

Many research areas for investigation of flameless combustion remain open. On the one hand, fundamental issues need to be researched, such as, the stability of the combustion process, NO_x formation, ignition kernels, et cetera. At the same time, the demand from industry, especially from companies already applying flameless combustion, for knowledge on implementation of flameless combustion in large scale furnaces equipped with multiple burners, is increasing. These questions comprise operation during turn-down, effects of the burner multiplicity, fuel flexibility, et cetera.

In this thesis, the objective is to investigate the behaviour of a system (furnace) where multiple regenerative flameless combustion burners are firing. The effect of the relative position of the burners with respect to each other, to the stack and to the heat sink is investigated. Furthermore, the influence of the firing mode, i.e., which burners form a

regenerative burner pair, is studied. These effects are assessed for their furnace performance. The furnace performance is defined as the heat extraction of the cooling tubes (heat sink), the temperature uniformity in the furnace and the emissions (CO and NO) in the flue gas.

In order to achieve these objectives three different setups have been investigated both experimentally and numerically. In the first place, experiments have been performed on an existing furnace equipped with two regenerative flameless combustion burner pairs at Kungliga Tekniska Högskolan (KTH) in Stockholm, Sweden. In this furnace only the influence of the firing mode was investigated, since it was not possible to change the positions of the burners. Secondly, a new multi-burner furnace has been installed at Delft University of Technology (DUT). In this furnace three pairs of regenerative flameless combustion burners were operated, whose positions could be varied. In order to understand and explain the experimental observations made in these furnaces, both furnaces were simulated using Computational Fluid Dynamics (CFD) simulations. Moreover, a prototype flameless combustion gas turbine combustor was fired with a low calorific value gas (simulating for example a biogas) to get more insight in flameless combustion itself and its (fuel) flexibility.

1.5 Thesis outline

In the following two chapters, the results of literature studies on multi-burner regenerative flameless combustion furnace experiments and CFD simulations are presented, respectively. Moreover, Chapter 2 ends with a detailed description of the newly installed multi-burner furnace at DUT, whereas at the end of Chapter 3 the choice of physical models used in the CFD simulations in this thesis is discussed in detail. Subsequently, in Chapter 4, the experimental and numerical results of the furnace at KTH are presented. For the furnace at DUT, the experimental and numerical results are divided over Chapter 5 and 6, respectively. In Chapter 7 all the results, both experimental and numerical, of the investigation on the flameless combustion gas turbine combustor are presented. Finally, Chapter 8 summarizes all the conclusions of the preceding four chapters, including recommendations for future research(ers) and industry.

Chapter 2

Experimental furnaces

This chapter focuses on experimental research regarding flameless combustion in furnace environments. In the first part, an overview of experimental research efforts on (semi-)industrial scale furnaces equipped with (multiple) regenerative flameless combustion burners is presented. In the second part of this chapter, a detailed description is given of the experimental multi-burner flameless combustion furnace that has been built and commissioned at the laboratories of DUT. It is denoted where and how this new experimental setup will satisfy existing deficiencies in the knowledge of regenerative flameless combustion in furnace environments. The experimental results of the DUT furnace are presented in Chapter 5. At the end of this chapter, an overview of the main characteristics and experimental results of the discussed furnaces is given.

2.1 Introduction

Since the introduction of flameless combustion in the early nineties of the last century, many universities and research departments of industry have made efforts in experimentally investigating this new technology. These studies have been performed on many different scales. The smallest scale is the jet-in-hot-coflow setup [15, 25, 26, 27]. In the design of these setups the flame is non-confined, generally in order to have optimal optical access for laser-based measurements. The recirculating flue gases required for flameless combustion are simulated by a flow of flue gas from a separate upstream lean combustor, the so-called coflow. On a slightly larger scale, experimental investigations are performed on laboratory-scale furnaces [12, 13, 14, 18, 22, 28, 29, 30, 31]. These are small furnaces generally fired with a custom made burner. The internal flue gas recirculation is genuine and with the use of high-temperature resistant windows also non-intrusive optical measurement techniques can be utilized in most of these setups. On the largest scale, Weber et al. investigated an industrial size furnace equipped with one commercial flameless combustion burner [32, 33, 34, 35]. However, the air preheating in this burner is not regenerative, but simulated by a vitiated air flow from an auxiliary burner. Also, reports of full industrial scale furnaces equipped with flameless combustion burners have been published, e.g., [36, 37], but these are not discussed in more detail here, as the number of published qualitative measurements is generally marginal. This chapter focuses on (semi-)industrial scale furnaces equipped with (multiple) regenerative flameless combustion burners. Generally, the advantage of this scale is that in these setups actual commercial burners can be operated and investigated using less or more advanced diagnostic equipment.

2.2 Flameless combustion furnaces

In this section an overview is given of the most important and latest experimental studies on (semi-)industrial scale furnaces equipped with (multiple) regenerative flameless combustion burners. In Table 2.1, at the end of this chapter, an overview is presented of the (operational) characteristics of these furnaces. Furthermore, the main results of the experiments that resemble the most the experiments performed on the furnace at DUT are also included.

At Kungliga Tekniska Högskolan (KTH) in Stockholm (Sweden) a 200 kW_{th} HiTAC furnace has been commissioned in 1999 for an extensive research programme [19, 38, 39]. In the furnace two types of flameless combustion burners were installed; one single autoregenerative REGEMAT burner and two pairs of NFK-HRS-DF regenerative burners. Both burners fired LPG and they were not operated simultaneously. The two pairs of regenerative burners could be operated in three different firing configurations and the per-

formance of the furnace has been compared for these firing configurations [40, 41]. Using different intrusive probes the temperature distribution, radiative and total heat flux and local flue gas compositions were measured inside the furnace [40]. Also, flame properties [42] and the performance of the regenerators [2] have been investigated in more detail. In brief, the research at KTH has largely contributed to the general knowledge of flameless combustion in industrial scale appliances.

Another extensive research program was initiated in 2002 at the IFRF research station in IJmuiden, the Netherlands [43]. The heating source in this furnace was one pair of NFK-HRS-DL4 regenerative burners, with a maximal thermal input of 1000 kW_{th}. The inner volume of the furnace was made adjustable from 12 to 20 m^3. In this way the thermal load per volume could be varied. However, in all the reported studies the furnace was operated at its maximum volume. Not only natural gas was fired, but also coke oven gas produced at Corus Steel was used as the fuel [44, 45]. The furnace temperature was taken as the average of eight type K thermocouple measurements in the side walls and five in the roof. The objectives of the furnace experiments were to generate extensive experimental datasets for the development and validation of CFD simulations [44, 45, 46]. For this purpose, also the flow fields in the furnace have been measured with non-intrusive laser measurements (LDA) [47]. Finally, based on the obtained results, a study has been performed on the implementation of the flameless combustion technique in industry [48, 49].

A third large research programme on flameless combustion was performed on a 200 kW_{th} furnace by Pesenti et al. at the Faculté Polytechnique de Mons (FPM) in Belgium [50, 51]. The heat source is one autoregenerative REGEMAT burner firing natural gas. The heat sink consists of water-cooled tubes that slide in and out of the furnace. In this way the thermal load of the heat sink could be controlled. The furnace temperature is defined as the flue gas temperature at 1.9 meter from the burner exit measured with a suction pyrometer. For the in-furnace measurements mainly intrusive probes were used, except for the OH concentration, which was determined by OH self-emission in UV measurements with a CCD camera [51, 52]. A comparison of the experimental data with CFD simulation results was the main objective. In particular the heat transfer, temperature and NO_x concentrations were compared.

Furthermore, at the NKK steel corporation in Japan several slab reheating furnaces with four pairs of regenerative burners were successfully fired with the by-product gas of the steel making factory [53, 54, 55]. The total thermal power input ranged from 2919 to 4640 kW_{th} and the heat sink was a moving slab in the bottom of the furnace. Temperature and gas composition have been measured at several positions inside the furnace intrusively. The obtained results served as validation data for an extensive numerical investigation of the furnaces.

Other studies, in the field of more industrially orientated research, include a study on

flameless combustion in semi-industrial scale furnaces performed at the research department of Gaz de France. A special interest was on the effect of varying the excess air ratio on the burner performance [56]. Additionally, tests have been performed with three different types of commercially available flameless combustion burners [57]. Finally, results (NO_x emissions and production rates) have been presented of flameless combustion burners installed in two actual industrial furnaces [3].

Furthermore, at the Gaswärme-Institut in Germany a research project has been initiated exploring and comparing new emission curbing combustion technologies [58, 59]. The performance of flameless combustion has been compared with conventional and air-staged combustion burners. The flameless combustion burner achieved lowest NO_x emissions at otherwise comparable conditions. Also experiments at furnace temperatures of around 1600°C, i.e., temperatures typical for the glass making industry, have been performed [4].

At the laboratories of burner manufacturer NFK in Japan electrostatic probe measurements were performed on a 1.2 MW_{th} flameless combustion furnace [60]. The reaction region inside the furnace was characterized with these measurements. Many thin reaction zones were observed in the furnace, which is in contrast with the distributed reaction zone, which is generally assumed to be present in flameless combustion.

Hughes et al. performed temperature measurements in a 200 kW_{th} natural gas fired flameless combustion furnace both using an intrusive suction pyrometer and a laser-based system (CARS, [61]). Two types of burners were investigated; a conventional low-NO_x burner and a self-regenerative flameless combustion burner. The results using the pyrometer were consistently lower than the CARS measurements, which was attributed by the authors to the lack of sufficient suction power of the pyrometer. Additionally, it was observed that the oscillations in the temperature were lower when firing a regenerative burner, compared to a recuperative low-NO_x burner. These lower temperature fluctuations resulted in lower emissions of NO_x for the regenerative burner.

Recently, interests are increasing for the fuel and oxidizer flexibility of flameless combustion in industrial scale furnaces. For example, experiments were performed in a single burner 200 kW_{th} propane and pure oxygen fired cylindrical furnace by Krishnamurthy et al. [62]. It was concluded that also in oxy-fuel applications, flameless combustion achieved improved furnace performance compared to conventional combustion.

Colorado et al. investigated a 20 kW_{th} furnace equipped with one self-regenerative burner firing both natural gas and biogas. Most of the reported results are similar for both fuels, except for the thermal performance of the furnace, which is slightly decreased when firing biogas [63].

Thus, it can be concluded that the flameless combustion technique has been extensively investigated over the last decades. Both furnaces with multiple burner pairs and setups with one burner (pair) have been performed. Some researchers have carried out

studies comparing flameless combustion to conventional and other low-emission combustion technologies. Also, the high fuel and oxidizer flexibility has been demonstrated, as will also be addressed in Chapter 7 of this thesis.

In Table 2.1, at the end of this chapter, an overview of the main characteristics and operational conditions of the above-discussed furnaces is given. Additionally, the experimental results that resemble the most the experiments performed on the DUT furnace are summarized, for comparison purposes. In the first row the characteristics and results of the DUT furnace are presented. It is noted that this furnace has a relatively high energy density compared to the other furnaces. Furthermore, the operational furnace temperature is on the lower side. Regarding the results, the NO_x emissions are lower than in most other furnaces. No large differences are observed for the CO emissions. It is noted here that the mentioned efficiencies are unreliable for comparison and thus merely indicative, since very few researchers specify the exact way of computation of this variable.

However, none of these studies investigated the influence of the positions of the burners in the furnace. The positioning of the burners can have a large influence on the furnace performance, especially in a regenerative (transient) environment. Therefore, investigation of the influence of burner positioning, such as burner-burner, burner-heat sink or burner-stack interactions, is required. A large 300 kW_{th} test facility at the laboratories of DUT has been established with three flameless combustion burner pairs and the possibility of changing the position of these burners. For further details on this furnace, see the next section.

2.3 Flameless combustion furnace at DUT

A furnace equipped with three pairs of regenerative flameless combustion burners has been designed, built and commissioned at Delft University of Technology. The burner pairs have a thermal power of 100 kW_{th} each, thus 300 kW_{th} in total. The furnace has inner dimensions of 1500 x 1500 x 1850 mm (length x width x height). The insulation consists of three layers of ceramic fire bricks, together 300 mm thick. In total 18 flanges for the burners are divided over two opposite sides of the furnace (nine each). In this way, it is possible to investigate different burner configurations in the furnace. In Figure 2.1 a sketch of the furnace is presented. Additionally, in Figures 2.2(a) to (c) drawings of the furnace front, back and side(s) are presented, respectively.

The burners were manufactured by Wärmeprozesstechnik GmbH and are of the REGEMAT CD 200 type. Drawings of these burners are presented in Figure 2.3. Each burner has four combustion air/flue gas nozzles around a central fuel nozzle. They can operate in two different modes; flame and flameless mode. In flame mode the air and fuel are mixed before injection and the mixture is injected through the air nozzles only, after ignition by a spark igniter. In flameless mode the combustion air is injected through the air

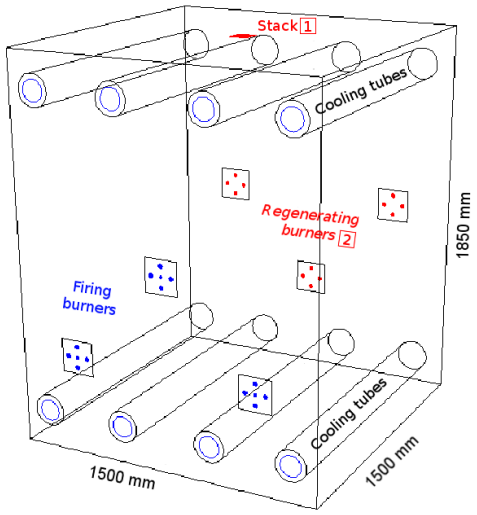

Figure 2.1: Furnace sketch. The boxed numbers 1 and 2 indicate the two sample positions for the flue gas. Sampling position 2 is after the regenerators (at its cold side). All dimensions are in mm.

nozzles and the fuel separately through the fuel nozzle. During heating up of the furnace the burners fire in flame mode. Once the furnace temperature exceeds 850°C (this temperature is above the auto-ignition temperature of the fuel/air mixture) the burners switch to flameless firing mode automatically. See also Figure 2.4 for the differences between flame and flameless mode. Dutch natural gas is used as the fuel, for its composition see Appendix A.

The burners have ceramic honeycomb heat exchangers incorporated. Eighty percent of the flue gas is sucked by a fan via the air nozzles over these honeycombs of the regenerating burners (thus heating them) for regeneration of the heat, while the remaining twenty percent is leaving the furnace via the central stack at the roof. Three burners are firing simultaneously, while the other three burners are regenerating. After a preset time interval of 10 to 30 seconds they switch and the firing burners start regenerating, et vice versa. During the firing period, the combustion air is led over the preheated ceramic honeycomb, thus achieving very high preheat temperatures of the air. The cycle time is defined as the total time of a complete firing and regenerating period together of one burner.

In order to simulate a thermal load, the furnace is equipped with a heat sink consisting of eight single ended cooling tubes; four placed above the burners and four beneath. These cooling tubes consist of two concentric annular tubes each, the inner tube with a diameter of 100 mm and the outer with a diameter of 150 mm. The stainless steel tubes have a thickness of 5 mm. The outer tube penetrates 1400 mm in the furnace, while the inner tube penetrates 1282 mm into the outer tube. Air is used as the cooling medium. The

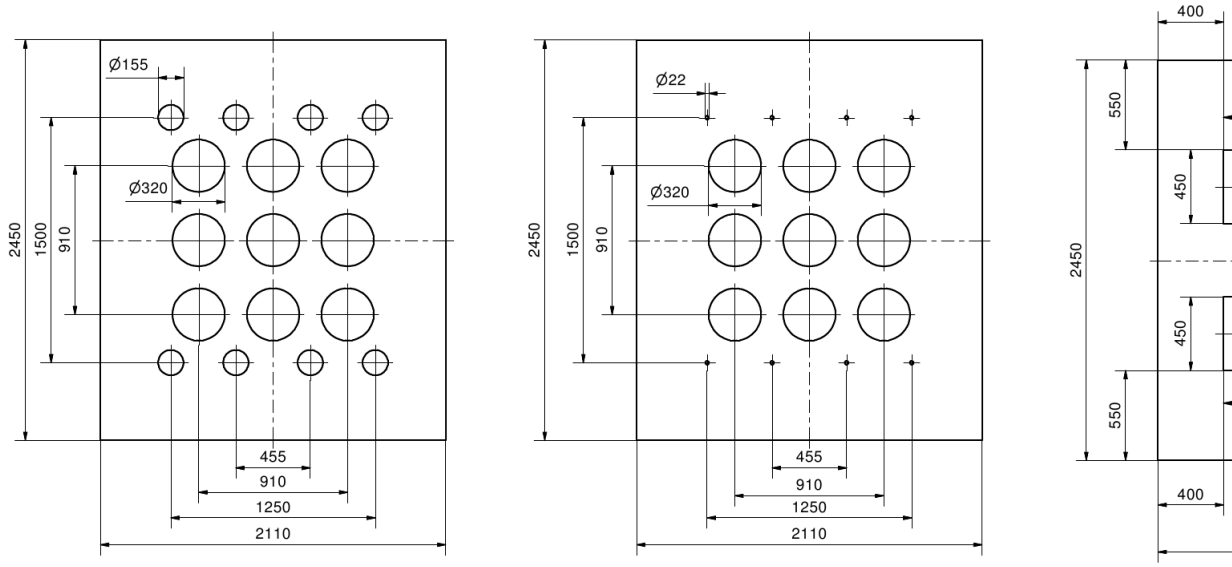

(a) **(b)**

Figure 2.2: (a) Furnace front; the large circles represent the burner flanges, the small circles deno tubes. (b) Furnace back; the large circles represent the burner flanges. (c) Furnace side(s); the t inserts where windows can be installed. The numbers represent outer dimensions in mm.

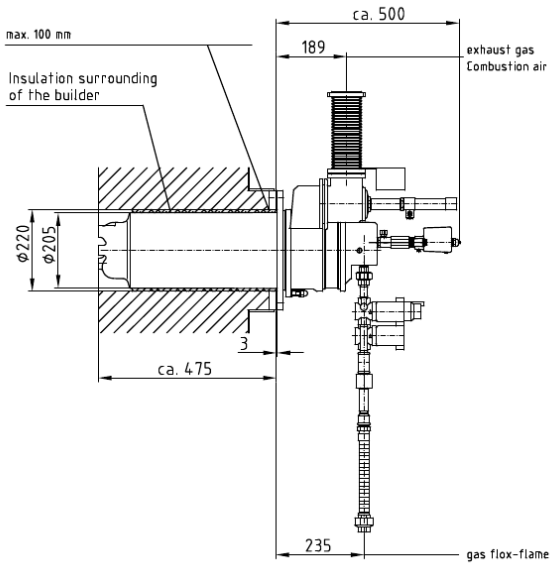

Figure 2.3: Scale drawings of the REGEMAT CD 200 type flameless combustion burner. Left-hand side represents a front view of the burner, displaying the four air/flue gas nozzles and central fuel nozzle. Right-hand side represents a cross section of the burner as built into a furnace wall. All dimensions are in mm.

air enters the inner tube, turns at the end and flows back through the annulus between the inner and outer tube. This setup was chosen to minimize the temperature gradients along the length of the outer tube, thus, creating an as uniform as possible heat extraction distribution.

As a part of the design efforts of the furnace, a separate study has been performed on the maximum thermal cooling capacity of the cooling tubes in the furnace, in order to estimate the required number of cooling tubes. The thermal cooling capacity of one cooling tube has been calculated using a customized engineering model and using an CFD simulation [64]. From the calculations a maximum thermal cooling capacity for one cooling tube was estimated to be around 25 kW_{th}, which in practice turned out to be slightly too optimistic.

During the experiments the temperature at the inside of the furnace walls was measured at various locations with slightly protruding TMG thermocouples type S. These thermocouples have a ceramic shield to reduce errors due to radiation losses and to protect the equipment. One of these temperature measurements, a double-fitted thermocouple in the side wall, was determined to characterize the furnace temperature. The pressure in the furnace was measured with a Kalinsky pressure transmitter type DS2.

The temperature of the cold combustion and cooling air is measured directly after the main air fan. The air is then split threefold; one line goes to the burners (combustion

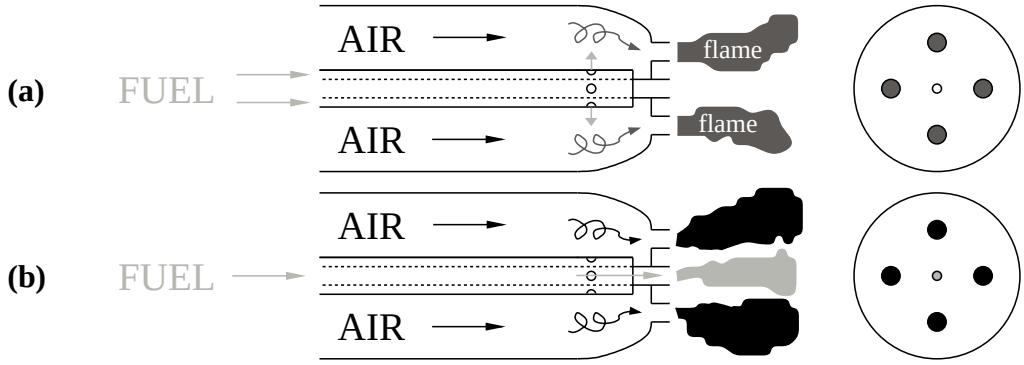

Figure 2.4: Schematic cross-sectional view of burner in different operational modes. Top level (a) represents flame mode; fuel and and air are mixed and introduced both through the air nozzles. The bottom level (b) is flameless mode; fuel and air are introduced separately through the fuel and air nozzles, respectively. Light gray arrows represent the fuel flow, black arrows the combustion air flow.

air) and the two other lines go towards the cooling tubes (cooling air). For every four cooling tubes there is thus one cooling air line. In these two lines the air flow is measured using Höntzsch thermal flow sensors TA10. For the simulation boundary conditions it was assumed that the cooling air was divided equally over the four cooling tubes. At the outlet of every cooling tube the temperature of the cooling air was measured.

All the comburant flows to the burners (fuel and air) are measured with custom made orifice plate flow meters. The conversion factors of the orifice plates are determined theoretically, see for more details Appendix B.

At all burner exits the temperature of the flue gas after regeneration is measured with TMG thermocouples type K. Also, the temperature of the preheated air was measured in two burners (one burner pair). For this purpose a thin thermocouple type S was inserted through the honeycombs of these burners to measure the temperature of the preheated combustion air leaving the regenerator.

As stated earlier, eighty percent of the flue gas is sucked by a fan over the honeycomb heat exchangers of the regenerating burners. This flue gas flow is measured using a Kobold vortex flow meter model PWL positioned after the flue gas fan. To convert this measurement to normal volumetric flow, also the local pressure and temperature are measured.

There are two flue gas sampling positions in the furnace. One is a sampling tube, crossing the diameter of the central stack, with six small sampling holes, in order to achieve an uniform sampling over the stack width, boxed number 1 in Figure 2.1. The second is after the vortex flow meter, thus, in the flue gas that has been regenerated, boxed number 2 in Figure 2.1. The flue gas is sampled by a KNF N024 ST.11E heated diaphragm gas sampling pump. After the sampled flue gas has been dried, by cooling

it down to approximately 2°C in a MAK 10-2 gas conditioner, it is analyzed using a Sick Maihak S710 gas analyzer. The NO and CO concentrations are measured using a MULTOR module based on the NDIR measuring principle. The O_2 concentration is determined paramagnetically with an OXOR-P module. The CO_2 concentration in the flue gas was monitored, but was not stored by the data acquisition system due to hardware limitations.

All the signals of the above-mentioned diagnostic equipment are recorded every second by a data acquisition system designed in Labview. Subsequently, the written raw data was analyzed by a Matlab routine, of which a summary is presented in Appendix B. A full process and flow diagram is presented in Figure 2.5.

As was stated before, the added value of the DUT furnace is its possibility of investigating many different burner configurations in combination with different firing modes. In this context, a *burner configuration* is defined as the position of the burners, i.e., which flange they occupy. The *firing mode* is referred to as which burners form a burner pair. For more details and results, see Chapter 5. Furthermore, the regenerative or cyclic behaviour of the burners can be investigated, since the recording time of the diagnostic equipments is much smaller than the typical cycle times, one second versus 20 to 60 seconds.

Finally, the furnace has been equipped with high temperature resistant quartz windows, allowing advanced in-furnace laser-based measurements in the near future. However, this was out of the scope of this thesis.

2.4 Conclusions

Flameless combustion has been proven to be a superior technique over conventional and over other emission curbing combustion technologies. In the recent years many experimental studies have been performed on flameless combustion, from very small scales for fundamental studies to actual industrial applications. This chapter presented an overview of research efforts on similar (semi-)industrial scale furnaces equipped with (multiple) regenerative flameless combustion burners. The furnace at DUT promises to supply valuable information concerning the influence of the burner configuration and firing mode in furnaces with multiple flameless combustion burners. Finally, in the near future, as high fuel flexibility is becoming more important for combustion techniques, flameless combustion will keep on being an interesting alternative for conventional combustion.

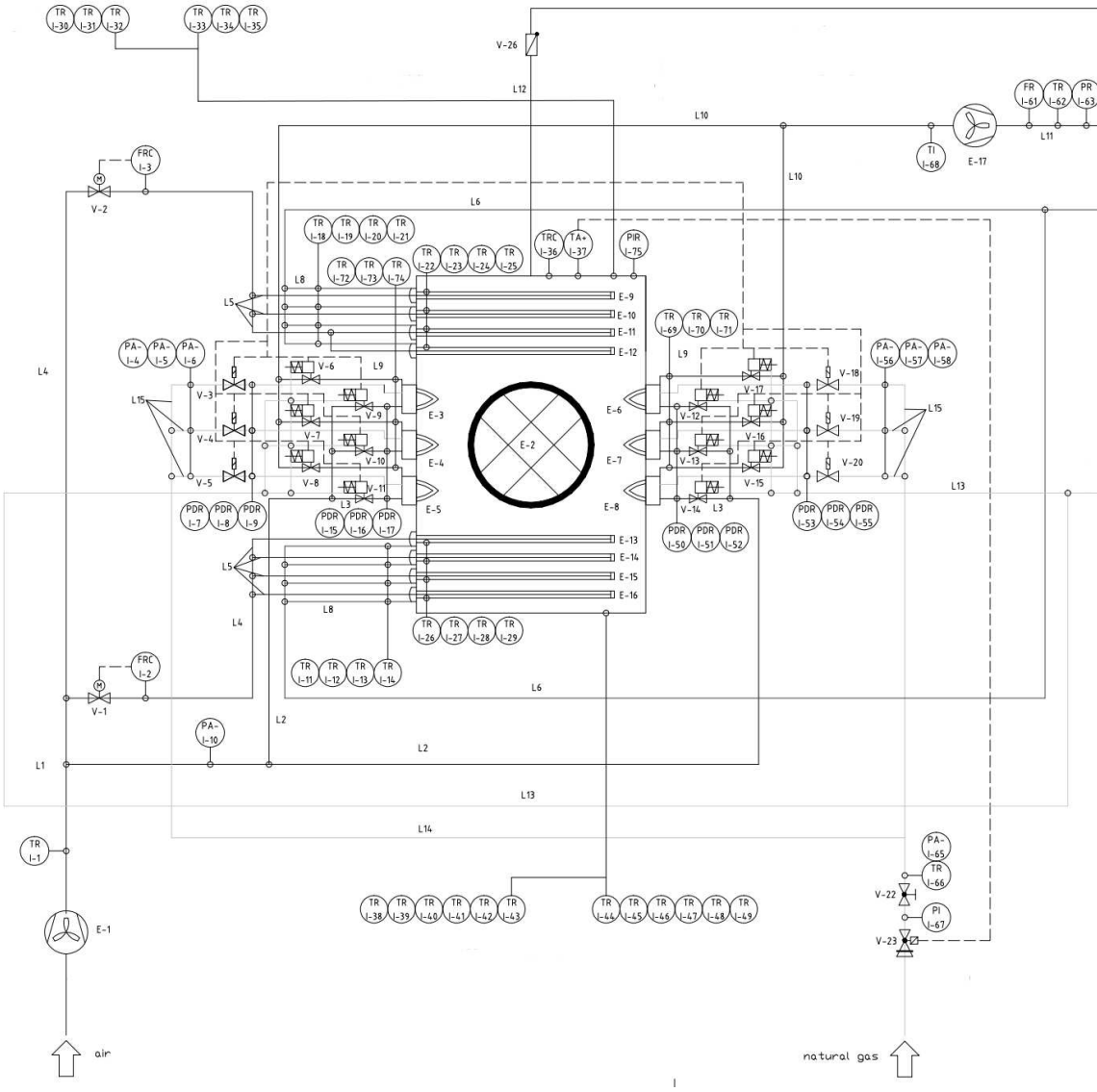

Figure 2.5: Process flow diagram of the furnace at DUT.

nal) characteristics and main experimental results of studies on similar (semi-)industrial scale flame-breviations: n.a. = not available, LPG = Liquefied Petroleum Gas, NG = Natural Gas, DNG = Dutch d Natural Gas, LCF = Low Calorific Fuel. Variables: P_{th} = thermal power, δ_E = energy density, t_{cycle} ratio, T_{furn} = furnace temperature, $T_{preheat}$ = combustion air preheat temperature and η = thermal DUT furnace.

	Fuel	**P_{th}** **(kW_{th})**	**δ_E** **(kW_{th}/m^3)**	**t_{cycle}** **(s)**	**λ** **(-)**	**T_{furn}** **(°C)**	**$T_{preheat}$** **(°C)**	**NO_x** **(ppm_v, dry @3%O_2)**	**CO** **(ppm_v, dry @3%O_2)**	**η** **(-)**
T CD200	DNG	300	72	20	1.15	1050	950	16	4	0.50
-DF	NG	200	27	60	1.1	1100	n.a.	39	2	0.46
-DF	LPG	210	28	60	1.15	1100	1040	55	n.a.	0.65
	LPG	210	28	20	1.15	1100	940	52	n.a.	0.56
-DL4	NG	910	46	60	1.27	1303	1270	94	~30	0.09
	NG	190	63	20	1.15	1090	900	4	n.a.	n.a.
	LCF	2919	30	60	1.15	n.a.	1133	n.a.	n.a.	n.a.
	LCF	3280	34	60	1.27	n.a.	1306	94	n.a.	0.73
	LCF	4640	10	60	1.05	n.a.	1300	n.a.	n.a.	0.66
	NG	200	n.a.	n.a.	1.1	1200	1000	85	n.a.	n.a.
	NG	3200	n.a.	n.a.	1.1	1220	n.a.	163	n.a.	0.21
	NG	300	55	n.a.	1.05	1200	1030	90	n.a.	n.a.
	NG	n.a.	n.a.	n.a.	1.05	1200	920	79	n.a.	n.a.
	LNG	1200	97	40	1.2	n.a.	900	10	n.a.	n.a.
	NG	192	n.a.	20	1.05	n.a.	895	12	n.a.	0.33
	NG	21	n.a.	60	1.2	870	537	3	15	0.70
	LCF	21	n.a.	60	1.2	870	680	2	16	0.68

Chapter 3

Computational Fluid Dynamics

Computational Fluid Dynamics (CFD) is a numerical method for the discretized simulation of continuous fluid flow with the possibility of including chemical reactions. This chapter starts with a discussion of fundamental CFD simulations of flameless combustion. In the middle part, a focus is on reported CFD simulation results of multi-burner (regenerative) flameless combustion furnaces. Then, the simulation approach for the numerical efforts presented in this thesis is discussed. This approach comprises the realizable k-ε turbulence model coupled by the Eddy Dissipation Concept model to a skeletal chemistry mechanism for the combustion of the fuel. Radiation is incorporated using the Discrete Ordinates method. Finally, at the end of this chapter, an overview of the models used in the CFD simulations of the furnaces equipped with (multiple) flameless combustion burner(s), is given.

3.1 Introduction

In Computational Fluid Dynamics (CFD) continuous fluid flow and chemical reactions are simulated in a discretized fashion. A numerical grid (or mesh) of the physical geometry is generated. This grid divides the physical volume in a finite number of cells. A set of transport equations, which describe conservation of mass, momentum, heat and species, are solved. Since direct numerical calculation of many physical phenomena are computationally too demanding for the state-of-the-art computers, many of these phenomena are represented by simplified models.

In the first part of this chapter, fundamental simulation efforts on flameless combustion are discussed, with a focus on simulations of semi-industrial scale furnaces in the second section. In the final part of this chapter, the choice of models used in the CFD simulations in this thesis is presented.

3.2 Simulation of flameless combustion

At the end of the second and in the beginning of the third millennium, the first detailed publications appeared on fundamental CFD simulation efforts regarding flameless combustion. Tabacco et al. [70] were such pioneers, simulating a single flameless combustion burner. In their simulations they used the Eddy Dissipation model [71] and a Probability Density Function (PDF) method assuming chemical equilibrium. Both models overpredicted the peak temperature, since they assume very fast chemistry compared to turbulence, whereas in flameless combustion the chemical and turbulent time scales are similar, $D_a \simeq 1$, with D_a the Damköhler number. Additionally, the NO_x contributors were assessed in the simulations. From the investigated contributors (thermal, prompt, nitrous oxide), it was concluded that nitrous oxide was the largest contributor. Additionally, some NO_x was formed via the thermal pathway, but none via the prompt mechanism.

In 2001 Coelho and Peters [72] presented the results of simulations of a flameless combustion burner. In their simulations they used the steady flamelet combustion model with presumed PDF for the mixture fraction. For the post-process calculation of the NO_x they used an Eulerian Particle Flamelet Model (EPFM). The numerical results have been validated with measured velocity fields and NO_x concentrations. The numerical results were in the same order of magnitude for both the velocity and the NO_x concentrations, however, the results can still be improved.

Murer et al. [73] investigated a single flame 30 kW_{th} flameless combustion furnace for several settings of the excess air ratio and furnace temperature (controlled by the heat extraction rate). The simulations incorporate a set of basic physical models. Combustion is modeled by a combination of the Eddy Dissipation model and Finite Rate chemistry (the ED/FR approach) with a two-step chemistry mechanism. The temperatures at the

furnace walls, which serve as the main validation method, were overpredicted, especially in the first half of the flame. The authors observed that the reaction zone is moving away from the burner outlet with decreasing furnace temperature.

Galletti et al. [74, 75] have simulated a recuperative 13 kW_{th} flameless combustion burner. A comparison between an 2D and 3D grid for the simulation of the burner was performed. The authors found that the 2D (axisymmetric) simulation overpredicted the recirculation in the burner. Furthermore, a comparative study was performed on turbulence and radiation models. The constant $C_{\varepsilon 1}$ of the standard k-ε turbulence model was increased from its standard value of 1.44 to 1.6. In Equation 3.1 the transport equation of the rate of dissipation of turbulent kinetic energy (ε) as solved in Fluent is presented [76],

$$\frac{\partial}{\partial t}(\rho\varepsilon)+\frac{\partial}{\partial x_i}(\rho\varepsilon u_i)=\frac{\partial}{\partial x_j}\left[\left(\mu+\frac{\mu_t}{\sigma_\varepsilon}\right)\frac{\partial\varepsilon}{\partial x_j}\right]+C_{\varepsilon 1}\frac{\varepsilon}{k}(G_k)-C_{\varepsilon 2}\frac{\varepsilon^2}{k}\rho+S_\varepsilon \qquad (3.1)$$

where ρ is the density, u the velocity, μ the viscosity, σ_ε is the turbulent Prandtl number for ε, k the turbulent kinetic energy, G_k represents the generation of turbulent kinetic energy due to the mean velocity gradients, $C_{\varepsilon 1}$ and $C_{\varepsilon 2}$ are modeling constants and S_ε is a (user-defined) source term. Thus, by increasing the constant $C_{\varepsilon 1}$ the dissipation rate generation term incorporating the generation of turbulent kinetic energy due to the mean velocity gradients is increased. The authors confirmed that this adjustment increased the recirculation in the burner, compared to the otherwise underpredicted recirculation when using the standard value of $C_{\varepsilon 1}$. Similar effects were observed in the simulation of a prototype flameless combustion gas turbine combustor, see Chapter 7. Finally, the authors note some differences between the models for radiation and spectral properties of the gases, e.g., the gray gas assumption overpredicts the temperatures.

In 2006 a flameless combustion combustor has been simulated using Large Eddy Simulation (LES) [77]. The results showed that LES can be a promising tool for the numerical study of flameless combustion. The method was, however, computationally very demanding, and a look-up table for the chemistry had to be set up to reduce the computational times.

Additionally, many studies have been performed specifically on comparing different combustion and/or chemistry mechanisms for the simulation of flameless combustion. In 2008 Kim et al. [78] compared the results for different global chemistry mechanisms in combination with the EDC model for turbulence chemistry interaction. Their conclusion was that the four-step global mechanism of Jones and Lindstedt [79] was able to predict the temperature profile correctly, but overpredicted the intermediate CO and H_2 concentrations. The authors also concluded that the EDC model was suitable for the calculation of flameless combustion processes.

Panne et al. [80] compared several combustion models (Eddy Dissipation (ED) model, combined ED/FR approach, Burning Velocity model) for the simulation of a flameless

combustion gas turbine combustor. These models were combined with two chemistry mechanisms, an one-step and two-step mechanism. While the authors refrained from drawing hard conclusions, the ED/FR approach combined with the two-step mechanism seemed to perform better. Finally, the Burning Velocity model was regarded as not suitable for the simulation of flameless combustion.

Finally, De et al. performed a detailed study on the capability of the set of models, as used in this thesis and described below, of simulating the experimental results of a jet-in-hot-coflow setup, which emulates flameless combustion [81]. It was shown that the realizable k-ε performed better than other two-equation turbulence models. Also, simulations using (the below-mentioned) constant values for the viscosity and the species mass diffusivities showed no significant differences with simulations with a temperature dependent viscosity or using multi-component diffusion. The largest difference, compared to the experiments, was that the ignition was predicted to occur too early. Finally, a limitation of the use of the EDC model with a skeletal chemistry mechanism was demonstrated for flows with low turbulence Reynolds numbers. Overall, the set of models was well capable of predicting flameless combustion.

3.3 Simulation of flameless combustion furnaces

Concurrently, the above-mentioned insights have been implemented in larger scale CFD simulations of flameless combustion furnaces. In this section these efforts are discussed in more detail, with again a focus on furnaces with multiple (regenerative) burners. At the end of this chapter, an overview is presented of the CFD simulations (and their incorporated physical models) of these furnaces, see Table 3.1.

The semi-industrial furnace at the Kungliga Tekniska Högskolan (KTH) has been simulated extensively with the STAR-CD CFD package [82, 83]. Besides the standard k-ε turbulence model, several combustion models have been investigated, of which the combined ED/FR approach turned out to give better results. A two-step chemical mechanism for the combustion of the fuel (LPG, i.e., propane), with CO as an intermediate, was used. Thermal radiation is calculated with the Discrete Ordinates method. The temperature in the cooling tubes was estimated using empirical equations based on measured temperatures. For the prediction of the formation of NO_x only the thermal and prompt pathways were incorporated. Most of the presented numerical results are for the autoregenerative burner setup [84, 85]. But also the results of CFD simulations of the experiments with the two regenerative burner pairs have been presented [86]. For the validation of the simulations measured heat fluxes, wall temperatures and in-furnace species concentrations were used. The validation results were reasonable, however the in-furnace temperatures, which these models are known to overpredict, were not compared. The different firing modes with the two burner pairs were investigated numerically and the main differences

observed in the experiments were reproduced in the simulations. However, the analysis of these results was mostly focused on the fundamental properties of flameless combustion, and less on the observed and reproduced differences. Finally, in 2008, Rudnicki et al. made an effort on doing transient simulations of the three different firing modes. Preliminary results have been presented [87], but since no validation against experimental data was provided, the quality of the simulations is hard to verify.

In 2004 Hekkens et al. simulated the experiments performed with the IFRF furnace using the Fluent CFD package [88, 89, 90]. Again, the standard k-ε turbulence model was applied. However, three different combustion models were applied; two PDF methods, assuming chemical equilibrium and laminar flamelets, and the Eddy Break-Up (EBU) model. In this last model a two-step chemistry for the combustion of methane was used. Radiation was incorporated using the Discrete Ordinates method. After detailed comparison of the numerical and experimental results, it turned out that the EBU model performed best regarding the species concentration predictions inside the furnace. The PDF methods were unable to correctly predict the temperatures inside the furnace, which can be explained by the fact that they assume (too) fast chemistry. However, also the EBU model overpredicted the peak temperatures inside the furnace, although two model constants in this model had been tuned for flameless combustion purposes using previous IFRF measurements.

The flameless combustion furnace at the Faculté Polytechnique de Mons has been simulated by Lupant et al. using the Fluent CFD package [51, 52, 91]. The standard k-ε turbulence model is applied. The value of the constant $C_{\varepsilon 2}$ was decreased from its standard value of 1.92 to 1.8, in order to improve the spreading rate of the round jets. See also Equation 3.1 for the transport equation of ε incorporating this model constant. The modification of the model constant $C_{\varepsilon 2}$ in the turbulence model improved the prediction of the delay in the reaction. Combustion modeling is done using both the PDF method assuming chemical equilibrium and the combination of Eddy Dissipation model and Finite Rate chemistry. Again, as in the simulations for the IFRF furnace by Hekkens et al., two model constants in the ED/FR approach were manipulated in order to improve the results. An one-step chemistry mechanism has been used for the combustion of methane. Radiative heat transfer is modeled with the Discrete Ordinates approach. NO_x modeling is performed incorporating the thermal and prompt pathways only. Validation of the simulations is performed by comparison of the measured heat transfer, temperatures and species concentrations inside the furnace and the NO_x levels in the flue gas. Reasonable agreement is achieved for the heat fluxes, however, all simulations overpredicted the temperature inside the furnace. This difference was decreased in the ED/FR model when the model constants were adjusted. In a subsequent step, the inlet temperature of the combustion air was lowered, which improved the results. However, it remains unclear how the exact combustion air temperature is calculated and if this adjustment was phys-

ically justified. The disagreement in the temperatures inside the furnace also makes the NO_x predictions unreliable. Although the maximum concentrations of O_2 were predicted rather well, the concentration was dropping too fast after this maximum. This indicates that the combustion reactions are too fast, which also explains the too high predicted temperatures.

Finally, the regenerative reheating furnace at NKK was simulated by Ishii et al. using the Fluent CFD package [53, 54, 55, 69, 92]. Again, the standard k-ε model for turbulence is used. For the modeling of the combustion the PDF method assuming chemical equilibrium is applied. Radiation is incorporated using the P-1 model. Besides these standard set of models, a wide variety of models was compared in [92]. Firstly, the standard and Renormalization Group (RNG) k-ε models and the Reynolds Stress Model (RSM) were compared, concluding that the differences in the results did not justify the usage of computationally more expensive models than the standard k-ε. This result is in accordance with the results observed in the combustor simulations, see Chapter 7 of this thesis. Also, no significant changes in the results was observed for the variation between standard or non-equilibrium wall functions and β- or δ-shaped PDF's. It was concluded that the characteristic length of the cells is preferred above the mean beam length for the path length used in the model for the absorption coefficient of the gas mixture. The NO predictions are based on the thermal, prompt and reburning models. In [54] the simulations are validated against in-furnace temperature measurements. The agreement is reasonable outside the combustion zone. Inside the combustion zone the temperatures are fairly overpredicted, as was observed also in the other simulations using an PDF method. After the validation of the simulation, several numerical investigations were performed. Besides a numerical investigation for design purposes [55], in [53] results are presented on the influence of variation of the air and fuel injection velocities on the NO emissions. The authors conclude that this velocity ratio has a strong influence on the NO production rate in the furnace. Finally, the importance of the three investigated NO pathways were investigated [69]. It was concluded that the reburning model did not contribute to the total NO emissions, since the fuel has low contents of methane. Furthermore, the authors stress the importance for accurate NO calculations of the PDF form used to incorporate the turbulence-chemistry interactions and the method of determining the O radical concentrations.

Mancini et al. have performed many simulations focusing on the formation of NO_x of experiments performed at the IFRF with a single flameless combustion burner. Mancini identified (as Hekkens did [90]) the prediction of the entrainment of the jets as the main problem in CFD simulations of flameless combustion [93]. In order to get around this problem, a simulation consisting of a network of perfectly stirred reactors (PSR) has been set up, incorporating detailed chemistry. The recirculation (or entrainment) was imposed based on experimental results [94, 95]. Comparison of their model with CFD

simulations [96] were performed, with a focus on the formation of NO_x. The prediction of prompt NO formation is significant in the PSR simulation, whereas little importance of this pathway is predicted by the CFD simulations. Furthermore, Mancini states that CFD simulations are not able to predict the strong reburning processes in flameless combustion, however, this will be contradicted in the next chapter. The benefit of this PSR simulation is the possibility of applying detailed chemistry, which improves the results significantly. However, the PSR simulation is highly empirical, i.e., many parameters should be known on beforehand, such as the entrainment values inside the furnace, for good simulation results.

Generally, it can be concluded that combustion models assuming fast chemistry are not applicable for the simulation of flameless combustion. Also, the importance of a careful choice of chemical mechanism can be concluded. Based on the above discussed simulation results and their validation, various combinations of physical models for the simulation of flameless combustion have been investigated, see also Chapter 7. This investigation resulted in a preferred (default) set of models, which have been used in the different simulation efforts in this thesis, see also Chapters 4, 6 and 7. In the next section the choice of this set of models is further explained.

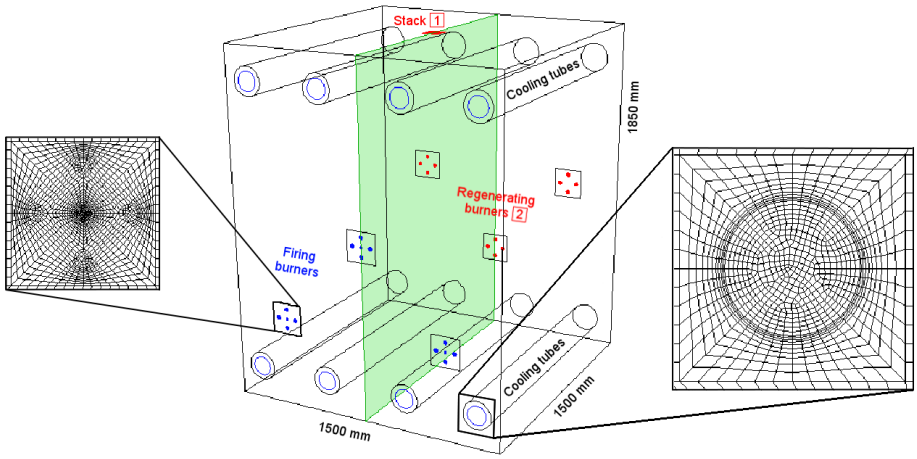

Figure 3.1: Furnace sketch, representing burner configuration C5 firing in parallel mode. The boxed numbers 1 and 2 indicate the two sample positions for the flue gas. The vertical symmetry plane is indicated by the filled (green) plane. All dimensions are in mm. The two inserts show enlarged frontviews of the mesh around a burner (lefthand side) and a cooling tube (righthand side). The total mesh contains approximately 1.5 million hexahedral cells.

3.4 Flameless combustion simulation setup

In this section the choice of physical models as used in the CFD simulations presented in this thesis is discussed.

Mesh

Three-dimensional meshes were generated, containing approximately 500.000 to 1.5 million hexahedral cells, depending on the physical domain. Exploiting (axi)symmetry of the domains, to reduce the computational time, only parts of the physical domains were meshed. In Figure 3.1 a sketch is presented of the furnace at DUT, with the shaded plane the vertical symmetry plane and in the two enlargements the mesh around the burners and the cooling tubes.

Solver

The CFD simulations were performed with the commercial code Fluent (versions 6.3.26 [76]). The implicit pressure based steady solver was used with Green-Gauss node based interpolation for all simulations.

Turbulence

All the above-mentioned studies use the standard k-ε turbulence model. However, it was decided to use the realizable k-ε model for the turbulence closure in these simulations. On the one hand, this model has been shown to give improved results, compared to the standard k-ε model, for the prediction of (round) jets [97], as is the case in these burners. On the other hand, in comparative preliminary simulations the realizable k-ε model performed better than the standard or the RNG k-ε models. In Equation 3.2 the transport equation for ε as solved in Fluent for the realizable k-ε model is presented,

$$\frac{\partial}{\partial t}(\rho\varepsilon)+\frac{\partial}{\partial x_j}(\rho\varepsilon u_j)=\frac{\partial}{\partial x_j}\left[\left(\mu+\frac{\mu_t}{\sigma_\varepsilon}\right)\frac{\partial\varepsilon}{\partial x_j}\right]+\rho C_1 S\varepsilon-\rho C_2\frac{\varepsilon^2}{k+\sqrt{\nu\varepsilon}}+S_\varepsilon \qquad (3.2)$$

where C_2 is an additional model constant and C_1 and S are calculated from the values of k and ε. Apart from some other improvements compared to the standard k-ε model, it is noted that in the realizable k-ε model the generation term $[\rho C_1 S\varepsilon]$ does not depend on the generation of k. Therefore, better predictions of velocity profiles in the jet have been achieved [97] and improved predictions of the recirculation caused by the jets can be expected.

In the simulations of the combustor in Chapter 7 the Reynolds Stress Model (RSM) was also investigated. The RSM solves six transport equations for the Reynolds stresses

and one transport equation for the dissipation rate ε (Equation 3.1), thus increasing the computational effort by the addition of five transport equations compared to the (realizable) k-ε models. The RSM model produced comparable results as the realizable k-ε model. Also, it turned out that the RSM underpredicted the recirculation rate of the jets. Therefore, the model constant $C_{\varepsilon 1}$ was increased from its standard value of 1.44 to 1.6. This constant is scaling the dissipation rate generation term incorporating the generation of turbulent kinetic energy (k) due to the mean velocity gradients, see also Equation 3.1. The adjustment of the constant proved that the actual results of the experiments could be reproduced by tuning this constant. Since the extra computational effort of the RSM became significant in the larger furnace computations, it was chosen to use the realizable k-ε model in these simulations.

Chemistry

For the combustion of the fuel the mechanism of Smooke et al. for the combustion of methane was applied, see [98]. This so-called skeletal mechanism consists of 16 species (resulting in 16 transport equations to be solved) and incorporates 46 reactions. The Arrhenius kinetic parameters are presented in Appendix C. It is noted here that a mechanism for the combustion of methane only is used. Actually, the fuel in the furnaces (Chapters 4 to 6) was natural gas, which also contains small amounts of higher hydrocarbons (mostly ethane to hexane). Thus, the natural gas in the furnace simulations is replaced by a simulation fuel, containing only methane as the fuel component, also replacing the higher hydrocarbons present in natural gas, in such way that the heat release per unit mass stays equal. For more details on the derivation of the simulation fuels, see Appendix A. Furthermore, the water content in the combustion air was also calculated, see Appendix D.

Turbulence-chemistry interaction

The turbulence-chemistry interaction is taken into account by using the Eddy Dissipation Concept (EDC) model [99]. The EDC model has been successfully applied for various turbulent and flameless combustion applications [100, 101]. Parente et al. compared results for flameless combustion with different turbulence-chemistry interaction models and chemistry mechanisms [102]. They concluded that the EDC model combined with a skeletal or full chemistry mechanism performed best. Additionally, Stefanidis et al. [103] also compared the EDC model with the Eddy Break-Up (EBU) model. They stress the main disadvantage of the EBU model, i.e., too fast reaction rates for the oxidization of the fuel. This disadvantage is especially undesired for flameless combustion applications, since in flameless combustion the reaction rates are relatively low. Finally, in another study [78] on the use of different chemistry mechanisms for the simulation of flameless combustion, the EDC model was used in all the test cases, since it was considered by the

authors as a very suitable model for the simulation of flameless combustion.

Radiation

Radiative heat transfer is accounted for using the Discrete Ordinates method and the Weighted Sum of Gray Gases Model (WSGGM) for the absorption coefficient of the gas mixture. For the used path length in the WSGGM both the mean beam length and the cell size has been investigated. Both characteristic lengths have proponents and opponents in the literature. In a brief comparison between two simulations of the KTH furnace using these two characteristic lengths, no large differences were observed in the final results. The choice of path length was therefore made depending on the specific goals of the simulations. For example, in the simulations of the KTH furnace (Chapter 4) a focus is on the radiative properties of the gas mixture, thus the cell size is chosen as the characteristic length. The emissivity of steel was set to 0.8 and that of the firebrick insulation to 0.68.

Material properties

The density of the mixture is calculated by the multicomponent incompressible ideal gas law. The molecular viscosity and thermal conductivity of the gas mixture are taken constant at $1.72\text{x}10^{-5}$ kg/ms and 0.0241 W/mK, respectively. The mass diffusivity is calculated by Fick's law with a constant and identical mass diffusion coefficient of $2.88\text{x}10^{-5}$ m^2/s for all species. Finally, the heat capacities are determined per species with a temperature dependent piece-wise polynomial provided by Fluent, and for the mixture with the mixing law.

NO_x chemistry

The formation of NO has been studied in post-processing mode. In post-processing mode none of the transport equations are calculated (thus the values of all the physical quantities remain equal), except for the transport equation(s) of the process of interest, in this case the formation of NO. The main advantage of this method is the enormous reduction of computational times. Calculations have been performed both simultaneously and separately for different NO pathways; the thermal NO, prompt NO, nitrous oxide (N_2O) intermediate and NO reburning mechanisms. By additionally performing simulations with the mechanisms separately it was verified that all mechanisms yielded realistic rates and the relative contributions of the different mechanisms could be investigated. Thermal NO is calculated using the extended Zel'dovich mechanism [6] with O and OH radical concentrations taken from the computed species concentrations. Prompt NO is incorporated by using the modified De Soete model [104, 105]. The N_2O intermediate mechanism [106] is calculated including a separate transport equation for the N_2O concentration. For the

prediction of the reburning of NO, the work of Bowman is followed [107]. Here, the CH radical concentration is computed based on the CH radical partial equilibrium. Finally, the fluctuations in the mean temperature and O_2 concentration have been included in the mean reaction rate of NO by a two-variable PDF which is assumed to be a two-moment beta function. However, the influence of these fluctuations on the total NO formation rate have been investigated and turned out to be small.

3.5 Conclusions

Flameless combustion in setups on many different scales has been extensively simulated using CFD software over the last decades. In general it can be concluded that many of the more simple combustion models result in too high prediction of the combustion reaction rates for flameless combustion. Thus, combustion models, including a more sophisticated description of the turbulence-chemistry interactions, are required. Moreover, it was found from the literature study that more elaborated chemistry mechanisms significantly improved the quality of the predictions for flameless combustion. Based on these findings, combined with the results of the numerical study in Chapter 7, a carefully selected set of physical models was determined and shown to be adequate for the simulation of flameless combustion (in large furnace environments).

stion furnace CFD simulations and their incorporated physical models. Abbreviations: n.a. = not zation Group, RSM = Reynolds Stress Model, ED = Eddy Dissipation, FR = Finite Rate, EDC = Eddy Probability Density Function, DO = Discrete Ordinates, DTRM = Discrete Transfer Method, P-1 = nics expansion, t = thermal NO, p = prompt NO, r = reburning NO, n = nitrous oxide intermediate. ce.

CFD Package	**Turbulence**	**Chemistry**	**Turbulence-Chemistry Interaction**	**Radiation**	**NO**
Fluent	realizable k-ε	16 species	EDC	DO	-
Fluent	realizable k-ε	16 species	EDC	DO	t,p,r,n
STAR-CD	k-ε	2-step	ED/FR	DTRM	t,p
STAR-CD	k-ε	2-step	ED/FR	DTRM	t,p
Fluent	RSM	n.a.	EDC	DO	-
Fluent	k-ε	2-step	β-PDF-equilibrium, -flamelets, ED/FR	DO	-
Fluent	k-ε	1-step, 2-step	β-PDF-equilibrium, ED/FR	DO	t,p
Fluent	k-ε	15 species	β-PDF-equilibrium	P-1	t,p,r
Fluent	k-ε, RNG k-ε, RSM	15 species	β-PDF-, δ-PDF-equilibrium	P-1, DTRM	t,p,r

Chapter 4

Firing modes in furnace with four burners

Combustion in a furnace equipped with two flameless burner pairs, with a thermal power of 100 kW_{th} each, has been investigated experimentally and computationally. The objective of this study is (1) to observe differences in the performance of the furnace operating in two different firing modes, parallel and staggered, and (2) to explain these differences using detailed CFD simulations. Besides the permanent measurements of temperature, flow and pressure, in-furnace probe measurements of temperature, oxygen and emissions (NO and CO) have been performed. Experimental results show that the efficiency of the furnace was higher in parallel mode compared to staggered mode, 48% and 41% respectively. The values of CO emitted were equal for both firing modes. However, in parallel mode the NO_x production was 39 $ppm_v@3\%O_2$, whereas in staggered mode 53 $ppm_v@3\%O_2$ NO_x was produced. Considering both efficiency and emissions, parallel firing mode performs better than staggered mode.

Next, CFD simulations of the furnace were performed in order to explain the observed differences. The simulations were validated with the in-furnace measurements. It was confirmed that the furnace firing in parallel mode achieved a higher efficiency. The radiative heat transfer was higher due to formation of a larger zone with gases with improved radiative properties. In addition, higher velocities along the cooling tubes, due to lower momentum destruction, led to higher convective heat transfer. Also, the lower production of NO_x in parallel mode was reproduced by the simulations. This is due to the fact that in parallel mode the fuel jets are merging slower with the combustion air jet, leading to less intense combustion zones. Thus, lower peak temperatures and radical concentrations are achieved, and the NO_x production via the thermal and N_2O pathways was lower.

The contents of this chapter have been published in *Combustion Science and Technology*, Emission and efficiency comparison of different firing modes in a furnace with four HiTAC burners, B. Danon, A. Swiderski, W. de Jong, W. Yang and D.J.E.M. Roekaerts, 2011;183(7):686-703.

4.1 Introduction

Flameless combustion, also known as High Temperature Air Combustion (HiTAC [5]), flameless oxidation [8] or MILD combustion [21], potentially offers enormous advantages compared to conventional combustion methods because it establishes a more uniform temperature distribution with lower emissions and higher efficiencies. For that reason it may become the preferred mode of combustion in industrial furnaces.

Many publications on experimental work regarding single flame semi-industrial furnaces are available [46, 50, 58]. Also experimental work has been reported on three flame [108] and four flame [54] furnaces, the latter with a fixed firing configuration. In the present work a semi-industrial 200 kW_{th} furnace equipped with two pairs of flameless combustion burners has been studied. The focus of this study is on the observation and explanation of differences in the efficiency and emissions (NO and CO) of the furnace firing either in parallel or staggered mode. Previously, this furnace has been experimentally investigated firing Liquefied Petroleum Gas [2, 41, 42]. In the present experiments the furnace was fired with natural gas instead.

For the explanation of the observed differences in the experiments, Computational Fluid Dynamics (CFD) simulations have been performed. In many previous CFD simulations of furnaces, combustion has been modeled using the Eddy Break Up (EBU) model in combination with simple reaction kinetics [83, 86, 89] or by fast chemistry/assumed PDF calculations [53, 55, 90]. Since the Eddy Dissipation Concept (EDC) model seems to be a promising model for the simulation of flameless combustion [109], in the present simulations the EDC model combined with a skeletal chemistry mechanism has been applied. Using these detailed CFD simulations, it was possible to explain the observed differences in performance between the two different firing modes.

4.2 Experimental setup

Experiments have been performed on a flameless semi-industrial test facility at Kungliga Tekniska Högskolan (KTH) in Stockholm, Sweden. The internal dimensions of the furnace are 1600 x 1600 x 2900 mm, for width, height and length, respectively. The firebrick insulation is 300 mm thick. In the furnace side walls two pairs of regenerative NFK-HRS-DF burners (manufactured by Nippon Furnace Koygo Kaisha) are installed. These burners have two fuel nozzles, separated 0.185 m from each other, with a central rectangular air nozzle in the middle, see also Figure 4.1(a). Each burner pair has a thermal capacity of 100 kW_{th}. The furnace is cooled with air flowing through four horizontal cooling tubes, made of a special temperature resistant kanthal alloy, see also Figure 4.1(c).

The burners have ceramic honeycomb heat exchangers incorporated. The flue gas is sucked by a fan via the air nozzles over these honeycombs (thus heating them) for regen-

eration of the heat. Two burners are firing simultaneously, while the other two burners are regenerating. After a time interval of 30 seconds they switch and the firing burners start regenerating, et vice versa. Different firing modes, i.e., selection of burners firing simultaneously, can be chosen.

The fuel consists of 90%-vol methane, 9%-vol higher hydrocarbons up to hexane and 1%-vol inerts (CO_2 and N_2) and has an LHV of 39.5 MJ/m_n^3. The wall temperature measured in the middle of the roof of the furnace was defined as the furnace temperature (T_{furn}). This temperature was kept constant at a preset value by varying the amount of cooling air flowing through the cooling tubes.

4.3 Diagnostic equipment

Besides the continuous measurements of temperature, pressure and inlet gas flows, detailed in-furnace temperature, oxygen and emission concentration data have been acquired. The temperature inside the furnace is measured using a suction pyrometer probe, while for the species analyses gas was sampled using a water-cooled sampling probe.

Permanent thermocouples, type K and S, are placed in the roof and in one of the side walls of the furnace. In burner A, see Figure 4.1 (b), the temperature of the air and flue gas entering and exiting the regenerator is monitored with a type S and type R thermocouple, respectively. Also the outside wall temperature is measured. In order to be able to calculate the heat extraction of the cooling tubes, the flow rates and temperatures of the cooling air flows are measured. The furnace efficiency is defined as the heat extracted by the cooling tubes divided by the total heat input.

The suction pyrometer probe has a ceramic tip, with a length of 180 mm and a hole on the side (diameter 10 mm) to suck the gases in. In the ceramic tip a type S thermocouple is mounted. This device has an error of about $10 - 15$ K at these temperatures.

The sampling probe, used for the species analysis, has a tip with a length of 150 mm. On the top of this tip there is a hole with 2.5 mm diameter through which the gases are sampled. The probe itself was cooled with cold water, whereas the tip was cooled with warm water (around 60°C). In Table 4.1 the species analysis techniques are presented. The error presented in the Table is the maximum possible error.

Table 4.1: Species analysis techniques.

Species	Analyzer	Technique	Range	±	Unit
O_2	M&C PMA 25	Paramagnetic	0–30	0.4	%-vol
CO	Maihak Multor 610	NDIR	0–30	0.6	%vol
CO	Sick GME 64	NDIR	0–1000	22	ppm
NO_x	Tecan CLD 700 EL ht	Chemiluminescence	0–1000	10	ppm

The probes were inserted using an automated traversing system. With this system the position could be controlled remotely and very accurately ($\pm$ 1 mm). During the experiments, on various positions inside the furnace the probe measurements were performed. In Figure 4.1 the topview (b) and sideview (c) of the furnace are depicted. The encircled numbers in Figure 4.1(b) represent the holes where the probes were inserted in the furnace. The different heights at which measurements were performed are presented in Figure 4.1(c).

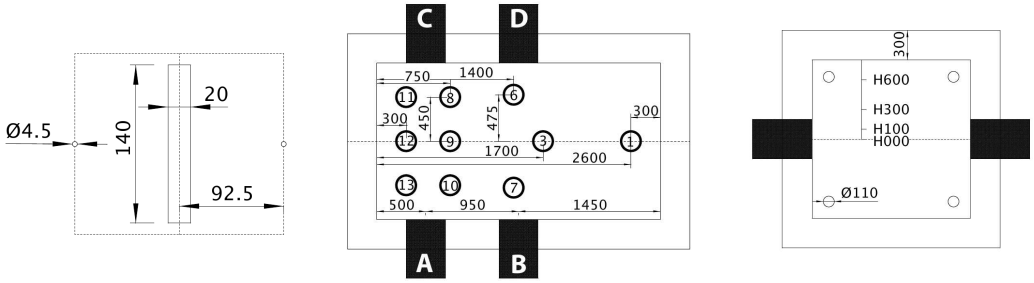

(a) (b) (c)

Figure 4.1: Burner frontview (a), with central rectangular air nozzle and two round fuel nozzles. Furnace topview (b) with encircled numbers indicating the probe insertion positions. Furnace sideview (c) with indication of probe measurement heights and cooling tube diameter and positions. All dimensions are in mm.

All signals, both permanent and in-furnace, were logged to a computer every two seconds with a Keithley 2701 Ethernet Multimeter system. The experimental results are obtained by first averaging the measurements at discrete time steps in the cycle for ten entire cycles. Subsequently, the last eight seconds (then steady state had been reached) of a half cycle, i.e. a firing or regenerating period, have been averaged.

4.4 Experimental campaign

In this work a comparison is made between two different firing modes, parallel and staggered, see also Figure 4.2. Other operational parameters were kept constant; the excess air ratio (λ) was 1.1 $\pm$ 0.05, the thermal power input was 200 $\pm$ 7 kW_{th} and the furnace temperature 1100 $\pm$ 5 °C. The cooling air is controlled such that the furnace temperature is constant.

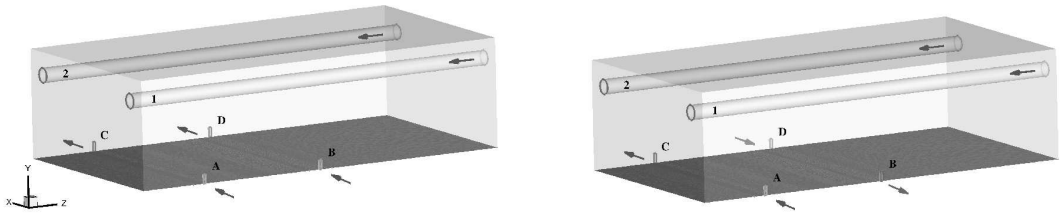

(a) Parallel (b) Staggered

Figure 4.2: Sketch of upper half of the furnace, showing the firing modes. The dark gray plane in the bottom represents the symmetrical midplane of the furnace. (a) Parallel: A and B firing, while C and D regenerating, et vice versa. (b) Staggered: A and D firing, while B and C regenerating, et vice versa. The cooling tubes are numbered 1 and 2. The arrows indicate the flow direction of the comburants and the cooling air.

4.5 Numerical setup

A three-dimensional mesh of the furnace was generated using Gambit 2.3. The mesh contains approximately 750,000 hexahedral cells. Exploiting the symmetry of the furnace with respect to the midplane through the burners, to reduce the computational time, only half of the furnace is meshed.

Steady simulations were performed with Fluent 6.3. The implicit pressure based steady solver was used with Green-Gauss node based interpolation.

For turbulence closure the realizable k-ε model was used. This model is shown to give improved results, compared to the standard k-ε model, for the prediction of jets [97], as is the case in these burners. For the combustion of the natural gas a skeletal mechanism (16 species, 46 reactions) for the combustion of methane was applied [98]. The natural gas is simulated with a simulation fuel, containing only methane, also replacing the higher hydrocarbons present in natural gas, in such way that the heat release per unit mass stays equal, see also Appendix A. The chemistry-turbulence interaction is taken into account by using the Eddy Dissipation Concept model [99]. Radiative heat transfer is accounted for using the Discrete Ordinates method and the cell-based Weighted Sum of Gray Gases model for the absorption coefficient of the gas mixture. The emissivity of steel was set to 0.8 and that of the firebrick insulation to 0.68.

The density of the mixture is calculated by the multicomponent ideal gas law. The molecular viscosity and thermal conductivity are taken constant. The mass diffusivity is calculated with the constant dilute approximation. Finally, the heat capacities are determined per species with a temperature dependent piece-wise polynomial, and for the mixture with the mixing law.

The heat losses through the walls were incorporated by calculating the convective

and radiative heat flux to the environment. For a realistic value of the effective thermal conductivity of the walls, the predicted furnace temperature agreed with the measured furnace temperature. Enhanced wall functions are combined with a two-layer model for the near-wall modeling.

The NO formation has been studied in post-processing mode. Calculations have been performed both simultaneously and separately for thermal NO, prompt NO, N_2O intermediate and NO reburning mechanisms. Thermal NO is calculated using the extended Zel'dovich mechanism with O and OH radical concentrations taken from the computed species concentrations. Prompt NO is incorporated by using the modified De Soete model [104, 105]. The N_2O intermediate mechanism [106] is calculated including a separate transport equation for the N_2O concentration. For the prediction of the reburning of NO, the work of Bowman is followed [107]. Here, the CH radical concentration is computed based on the CH radical partial equilibrium. The fluctuations in the mean temperature and O_2 concentration have been included in the mean reaction rate of NO by a two-variable PDF which is assumed to be a two-moment beta function. The influence of the fluctuations on the total NO formation rate have been investigated and turned out to be small.

4.6 Results and Discussion

4.6.1 Experimental results

The obtained results for the furnace operating in parallel and staggered mode are presented in Table 4.2. In the last column the variance (σ^2) of the variables is presented, a value not available for the cooling air flow rate (ϕ_{cool}), since this was not kept constant. It is observed that in parallel mode, at the same furnace temperature, more heat is extracted by the cooling tubes, compared to staggered mode.

Table 4.2: Main results for parallel and staggered firing modes.

Variable	Parallel	Staggered	σ^2
T_{furn} (°C)	1101	1099	1
ϕ_{fuel} (m_n^3/h)	17.0	17.0	0.2
ϕ_{air} (m_n^3/h)	192.4	193.7	1.5
ϕ_{cool} (m_n^3/h)	628.6	501.8	n.a.
T_{coolin} (°C)	31	31	0.1
$T_{coolout}$ (°C)	390	407	1
Q_{cool} (kW)	91.2	76.4	n.a.

In Figure 4.3 pie charts of the calculated heat balances for the two firing modes are presented. The 'Efficiency' is defined as the cooling tube heat extraction and the 'Flue

gas losses' are the sensible heat of the flue gas after regeneration. The 'Other losses' consist mainly of wall losses, but also losses to the (cold) probes, losses through cracks, etc. All the heat flows were divided by the total heat input, based on the LHV of the fuel. The efficiency of the furnace in parallel mode is 48%, whereas in staggered mode the efficiency is 41%.

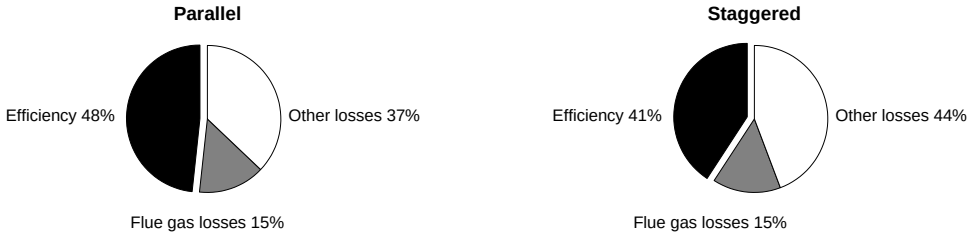

Figure 4.3: Heat balances for the furnace in both firing modes.

In Table 4.3 the composition of the flue gas during the two firing modes is presented. It is noted that for similar operation conditions (i.e. combustion air and fuel flow rates, T_{furn}) the NO_x emissions differ substantially between the two firing modes. In parallel mode 39 $ppm_v@3\%O_2$ of NO_x is produced, versus 53 $ppm_v@3\%O_2$ in staggered mode. Comparable values and trends has been observed previously in this furnace firing LPG [41, 86], however, further investigation on the sources of these differences in NO concentration is required. No significant differences could be observed in the CO emissions.

Table 4.3: Species concentrations in the flue gas (on dry basis).

Variable	Parallel	Staggered
O_2 (%-vol)	1.9	2.1
CO ($ppm_v@3\%O_2$)	2	2
NO_x ($ppm_v@3\%O_2$)	39	53

Concluding, parallel firing mode shows lower NO_x emissions combined with higher efficiency, and is therefore preferred over staggered firing mode. The same trends have also been observed in this furnace with LPG [86] and with natural gas in the multi-burner furnace, see Chapter 5. with different burners [110].

4.6.2 CFD validation

In Figure 4.4 the predicted values for temperature and O_2 concentration inside the furnace are compared with the measured values. The hole number is denoted on the *x*-axis, with four points per hole, representing the four different heights, from low to high, where

measurements were performed, see also Figure 4.1(b) and (c). No measurements were performed in hole 1.

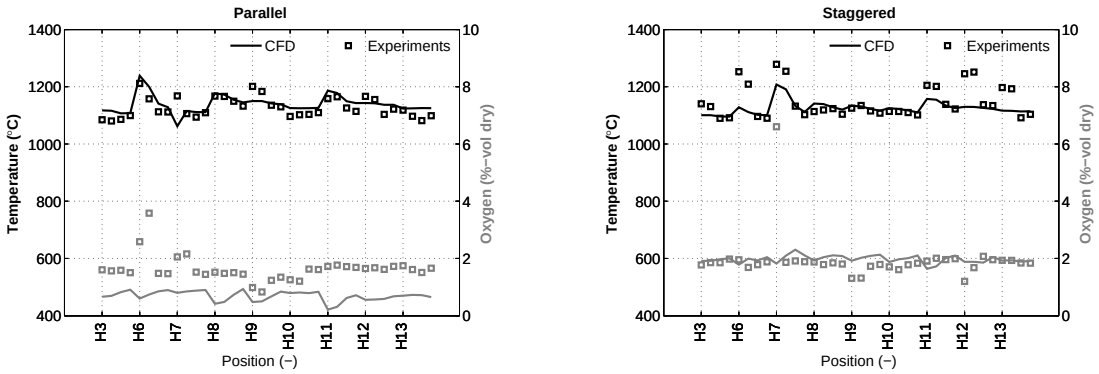

Figure 4.4: Comparison between the steady state experimental and simulated results for parallel and staggered mode. Squares represent the experiments, solid lines the CFD simulations. Oxygen concentrations (%-vol dry) are in gray and temperatures (°C) are in black.

The predicted temperatures inside the furnace agree well with the measured values. Also, the trend in the temperature agrees reasonably.

For the staggered case, the O_2 concentrations agree well with the measurements. However, in parallel mode, the predicted O_2 concentrations are consistently lower than the measured values. This is due to air leakage. During the experiments in parallel mode, the furnace pressure dropped significantly below zero for two seconds every cycle. Since it is known that there are openings and cracks in the furnace, during these periods of negative pressure, ambient air leaks into the furnace. This air leakage was proven by simple calculations to be large enough to explain the observed differences, see also Appendix E. In staggered firing mode the negative pressure peaks were negligible.

In Table 4.4 the heat balance of the experiments and simulations are compared. The heat extracted by the cooling tubes in the simulations is lower than the experimental values. This non-extracted heat is leaving the furnace partly via the walls and partly as sensible heat of the flue gas. This remains an unresolved issue in the simulations. However, it is noted that the trend in the results for parallel and staggered firing mode do agree, showing that essential aspects of the change of firing mode are captured.

It was concluded that the CFD simulations are validated sufficiently for the purpose of investigating the observed differences in efficiency and emissions for the different firing modes.

Table 4.4: Heat balance comparison between experiments and simulations.

	Parallel		Staggered	
	Experiment	CFD	Experiment	CFD
Cooling tubes (kW)	91.2	67.4	76.4	61.9
Flue gas losses (kW)	29.9	50.0	30.7	48.5
Wall losses (kW)	70.0	77.3	83.9	83.1
Total (kW)	191.1	194.7	191.0	193.5

4.6.3 Efficiency comparison

From analysis of the CFD simulations, the increased efficiency in parallel mode turned out to be mainly due to increased radiative heat transfer, and to a smaller extent to increased convective heat transfer.

Table 4.5: Cooling tube comparison between parallel and staggered firing mode.

	Parallel	Staggered
Tube wall temperature (K)	1332	1322
Furnace maximum gas temperature (K)	1814	1890
Mean velocity magnitude 1 mm from tube wall (m/s)	0.67	0.55
Hot side heat transfer coefficient (W/m^{2}K)	16.3	15.0

In order to evaluate the convective heat transfer to the cooling tubes, the important parameters regarding convective heat transfer are presented for the cooling tubes in Table 4.5. The mean tube wall temperatures of the cooling tubes in both firing modes are almost equal. Thus, the convective heat extraction in parallel mode is higher due to the increased velocity along the tubes, resulting in a higher heat transfer coefficient. The differences in velocity can be related to the rate of momentum destruction in the furnace. In Figure 4.5, where the momentum along the centre line of the burner pairs is presented, it can be observed that in staggered mode more momentum is destroyed by the opposing jets, leading to lower velocities in the furnace.

For comparison of the radiative heat transfer, the mean radiative heat extraction (RHE) by cooling tube 1 and 2 (see Figure 4.2), plotted along the tubes, is presented in Figure 4.6. Note here that an increased RHE means a lower or more negative value. Additionally, the normalized emissive source term, defined in Equation 4.1, was considered [111],

$$\mathrm{R_e} = \frac{\alpha}{\alpha_\mathrm{r}} \left(\frac{T}{T_\mathrm{r}} \right)^4 \tag{4.1}$$

where α is the absorption coefficient (m^{-1}), T the temperature (K) and the subscript r

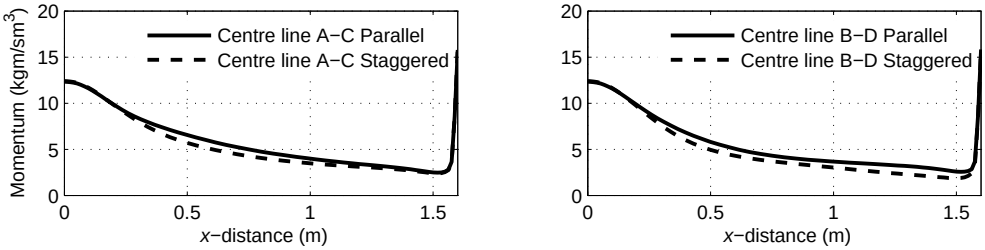

Figure 4.5: Momentum per unit volume (kgm/sm^3) on the centre lines of burner pairs A-C and B-D for both firing modes.

denotes reference values ($\alpha_r = 1\text{m}^{-1}$, $T_r = 298\text{K}$). In Figure 4.7 contours of higher values of the normalized emissive source term ($R_e \geqslant 750$) in the furnace midplane for both firing modes are presented. These zones indicate where most radiative energy is emitted by the hot gases. The centre line of cooling tube 1 is the lower gray line in Figure 4.7 and cooling tube 2 the upper gray line. The *z*-distance increases from left to right in Figure 4.7.

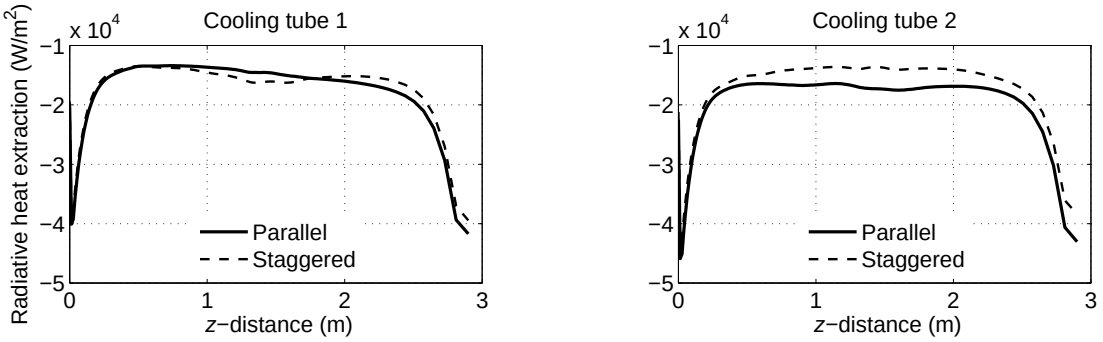

Figure 4.6: Mean radiative heat extraction (W/m^2) along the cooling tubes.

In Figure 4.6 it is observed that cooling tube 1 has comparable radiative heat extraction (RHE) for both firing modes. It is noted that an increase in the RHE is observed in staggered mode around *z*-distance 1.5 m, which is due to the location of high R_e in this location, see Figure 4.7. Note that the central air nozzles of burners B and D are at *z*-distance 1.45 m, see also Figure 4.1(b).

For cooling tube 2 the RHE is higher for parallel mode along the entire length of the tube. This is confirmed in Figure 4.7 by the location of the higher values of R_e in parallel mode underneath this cooling tube. Additionally, there is no distinct increase visible in the RHE at *z*-distance 0.5 m (centre line of burners A and C) for staggered mode in cooling tube 2. This is due to flow direction of the cooling air. Because the cooling air is entering at *z*-distance 2.9 m and then travels towards 0 m, the RHE decreases with decreasing *z*-distance due to the increasing temperature of the cooling air. The expected increase in

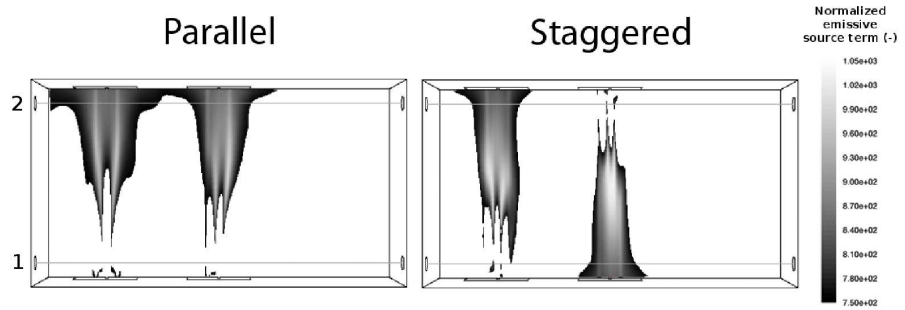

Figure 4.7: Higher values of the normalized emissive source term (-) on the furnace midplane. The horizontal gray lines denote the centre lines of the cooling tubes, cooling tube 1 is the lower and cooling tube 2 is the upper line.

RHE of cooling tube 2 in staggered mode at *z*-distance 0.5 m cancels with the decrease due to this phenomenon.

Overall, it is observed in Figure 4.6 that in parallel mode more radiative heat is extracted by the cooling tubes. This is confirmed in Figure 4.7 by an overall larger zone with high values of the emissive source term R_e in parallel mode. In staggered mode higher maxima in the R_e are observed in the centre of the furnace, however, these maxima are located further from the cooling tubes.

Finally, the normalized absorptive source term [111], as defined in Equation 4.2, was considered,

$$R_a = \frac{\alpha}{\alpha_r} \left(\frac{(G/4\sigma)^{1/4}}{T_r} \right)^4 \tag{4.2}$$

where G is the incident radiation (W/m^2) and σ the Stefan-Boltzman constant (W/m^{2}K^4). The contours of the absorptive source term are presented in Figure 4.8. The zones with highest absorptive source term are the fuel jets. This is because these jets are relatively cold and have high methane contents. In the rest of the furnace there are no other distinct zones with high absorptive source term.

Concluding, the efficiency is higher in parallel mode, due to an overall larger zone with high emissive source term close to the cooling tubes and less momentum destruction.

4.6.4 Emission comparison

In Table 4.6 the measured and simulated values for the concentration of NO_x in the flue gas are compared.

The simulated values for NO_x are slightly overpredicted. However, their order of magnitude do agree. Also, in the simulations, as in the experiments, parallel firing mode

Figure 4.8: Normalized absorptive source term (-) on the furnace midplane.

Table 4.6: NO_x concentrations in the experiments and the simulations.

	Unit	Parallel	Staggered
Experiment	ppm_v@3%O_2 dry	39	53
Simulation	ppm_v@3%O_2 dry	48	86

produces less NO_x than staggered. The production of NO_x via the thermal, prompt, N_2O intermediate and reburning pathways were investigated both separately and simultaneously.

About half of the NO_x was formed via the thermal pathway, whereas the other half was produced via the N_2O intermediate pathway. No NO_x was formed via the prompt pathway, however the reburning pathway did result in a reduction of the emissions.

This is noteworthy, since both the prompt NO and NO reburning mechanisms occur in fuel-rich zones, where CH_i radicals react with N_2 and NO, respectively. Since the fuel and air are introduced separately, a fuel-rich zone is present in front of the fuel nozzles. The reason that in these zones no NO is formed via the prompt mechanism but NO is reburning, is the temperature dependence of the chemical reactions. In Figure 4.9 the reaction rates for prompt NO and NO reburning are plotted versus the local temperature. Indeed, it is noted that at lower temperatures the NO reburning mechanism shows higher reaction rates than the prompt NO mechanism.

Mancini et al. investigated quite extensively the NO formation in a single-burner flameless combustion furnace [96, 95]. In different CFD simulations they find either mainly thermal NO or mainly prompt NO. Based on a Reactor Network Model (RNM), tuned with experimental recirculation data, they find the NO reburning mechanism to be important for flameless combustion conditions, as has been found in this chapter. However, Mancini observed in the RNM large quantities of NO formed via the prompt mechanism. This observation disagrees with the present results and could be due to overpredic-

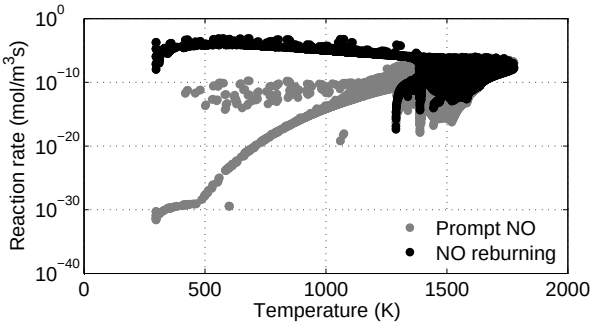

Figure 4.9: Rate of formation of prompt NO and rate of destruction for NO reburning (mol/m^{3}s) versus the local temperature (K). Data are values of all grid cells of the furnace midplane.

tion of the local temperatures in the RNM model, see also Figure 4.9. Moreover, Mancini did not observe any NO formation via the N_2O intermediate pathway, which disagrees with both the present results and previously reported results [112].

In Figure 4.10 the NO_x formation is presented on lines at x/d = 12, where x is the distance from the burner nozzles and d is the hydraulic diameter of the air nozzle (0.035 m). It was found that at this distance from the burner nozzles the production of NO_x was at its maximum. The central air nozzles of burners A and C are at z-distance 0.5 m, and at 1.45 m for burners B and D, see also Figure 4.1(b). It is observed that the total NO_x production is higher in staggered firing mode.

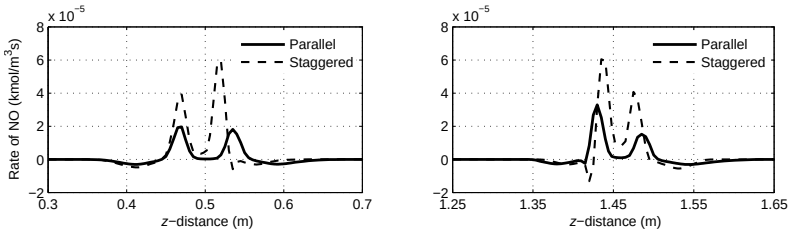

Figure 4.10: Total rate of formation of NO (kmol/m^{3}s) on lines at x/d = 12.

For further investigation, the temperature and the OH radical mole fraction are presented in Figure 4.11 over the same lines at x/d = 12. The vertical lines denote the centre lines of the nozzles; the middle line for air and the outer two lines for the fuel nozzles.

As expected, higher peaks in both the temperature and OH mole fraction are present in staggered mode. Additionally, it is observed that these peaks in staggered mode are closer to each other. This indicates that the combustion zone is smaller and more intense in this mode.

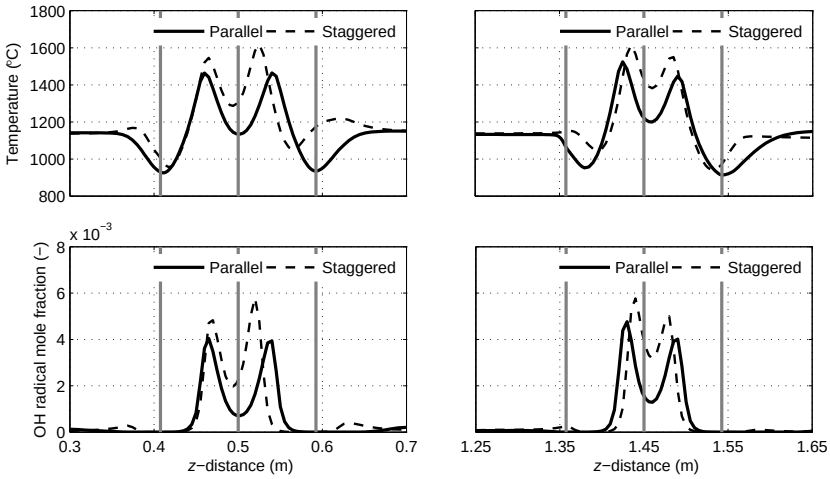

Figure 4.11: Temperature (°C) and OH radical mole fraction (-) on lines at x/d = 12.

In order to explain these more intense combustion zones in staggered mode, the velocity magnitude vectors are plotted on the furnace midplane in Figure 4.12. In these vector plots it is observed that the fuel jets in staggered mode are merging faster with the central air jet. The merging of the comburants jets plays an important role in the establishment of flameless combustion behaviour.

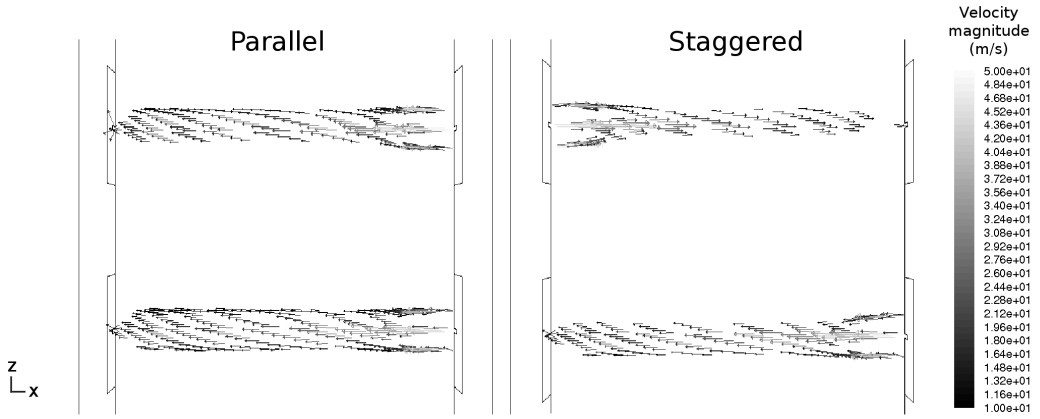

Figure 4.12: Velocity magnitude (m/s) in vector view on the furnace midplane. Burners A and C are the lower burners, B and D the upper.

The interaction of multiple parallel jets with different Reynolds numbers, the strong-jet/weak-jet problem, can be divided into three zones [113, 114]. The first zone is called the 'converging zone', where recirculation in between the jets occurs. This zone extends downstream until all velocities in between the jets are non-negative. The second zone,

the 'merging zone', continues until the velocity peak of the jet with the lower Reynolds number disappears, i.e., the point of confluence (x_c). Further downstream, the 'mixing zone', is where the multiple jets have merged and behave like one jet.

No clear differences were observed in the size of the converging zones for the different firing modes. In Figure 4.16, the velocity in the *x*-direction (i.e. the direction of injection) is plotted at several distances from the nozzles of burner A in order to identify the point of confluence. It is noted that the point of confluence of the fuel nozzle on the right side is different for the two firing modes. In staggered mode, the point of confluence is around *x*/d = 9 for this fuel jet, whereas in parallel mode it is around *x*/d = 12.

Grandmaison et al. [115] derived a mathematical model for the strong-jet/weak-jet interaction. Using this model, the point of confluence of a single fuel jet and the central air jet has been calculated to be around 14 *x*/d, for both parallel and staggered mode. This value agrees in order of magnitude with the experimental values, however, the difference between the two firing modes was not reproduced. Thus, it is shown here that the interaction of the burners influenced the actual position of the point of confluence.

Additionally, Grandmaison also derived an expression for the amount of entrainment to the jets as a function of the distance of the point of confluence from the burner outlets. In Figure 4.13 the point of confluence divided by the air nozzle diameter (d) is plotted versus the momentum flux ratio of the jets and the entrainment to the jets, for the theoretical case of one air and one fuel jet. The ratio of momentum flux in these burners is around 0.1. It is observed in the Figure that for both the air and the fuel jet a longer distance to the point of confluence results in more entrainment.

Summarizing, in this particular case, the observed shorter distance to the point of confluence (due to burner interactions) of the fuel jet in staggered mode results in less entrainment, which leads to higher NO formation rates. Also compare Figure 4.10 and Figure 4.16 at *x*/d=12 and between *z*-distance 0.5 and 0.55 m. For the other burner pair comparable differences were observed.

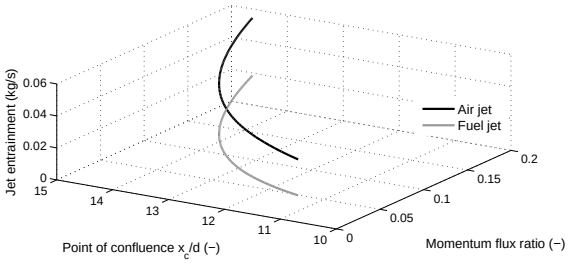

Figure 4.13: Distance of the point of confluence (x_c/d) versus the momentum flux ratio (-) and the jet entrainment (kg/s). Values are for the theoretical case of one fuel jet computed with the strong-jet/weak-jet model of Grandmaison [115].

In order to illustrate the correlation between the jet merging behaviour and the NO production, the maximum reaction rate of NO at *x*/d = 12 is plotted versus the location of the point of confluence (x_c) divided by the air nozzle diameter (d) for all fuel nozzles in Figure 4.14. It is observed that the slower the fuel jet merges with the air jet (higher values of x_c), the less NO is formed. The correlation seems to be linear, although more data would be required to verify this.

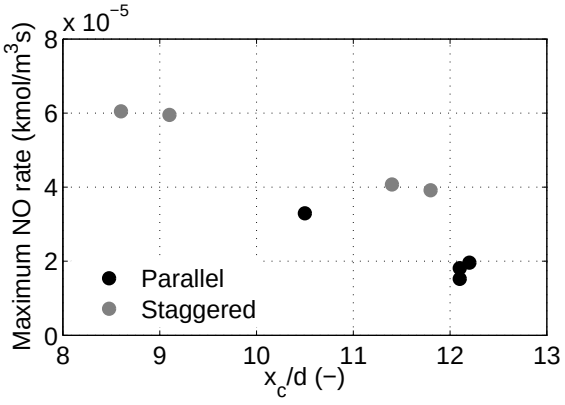

Figure 4.14: Maximum reaction rate of NO at x/d = 12 versus the location of the point of confluence x_c/d (-) for all fuel jets.

Additionally, the recirculation ratios [8], i.e. the mass flow of the sum of the inlet and recirculated gases over the mass flow of the inlet gases, for the air nozzles of the burners for both firing modes are presented in Figure 4.15. As expected, the recirculation ratio in staggered mode is lower than in parallel mode, confirming that less flue gases are internally recirculated.

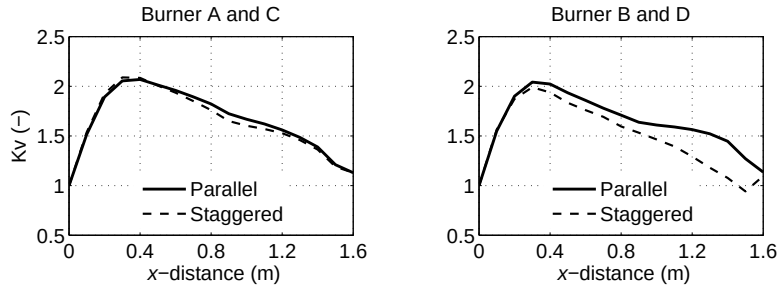

Figure 4.15: Recirculation ratios (-) for air nozzles for both firing modes.

Concluding, the slower merging of the comburant jets in parallel mode allows higher recirculation ratio and leads to a less intense combustion zone, with lower peak temperatures and oxygen availability, and thus lower production of NO_x.

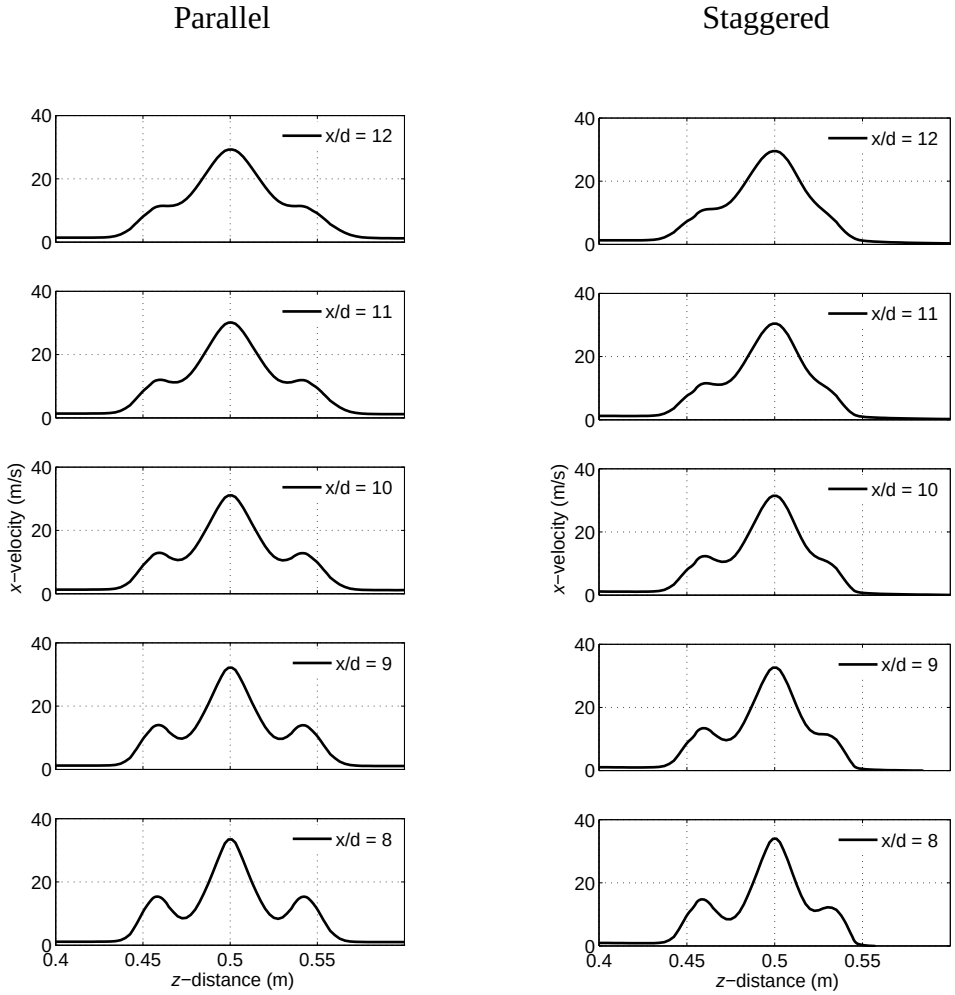

Figure 4.16: Predicted x-velocity (m/s) on several lines on the furnace midplane from the nozzle exits of burner A perpendicular to the direction of injection.

4.7 Conclusions

A furnace with two flameless burner pairs was investigated operating in two different firing modes, parallel and staggered. The focus of this study was on the (1) observation and (2) explanation of the differences in efficiency and emission production between the different firing modes in the furnace. No significant differences were observed for CO emissions. In the experiments it was shown that parallel firing mode led to higher heat transfer to the cooling tubes (i.e. efficiency) and lower NO_x emissions.

Detailed CFD simulations were performed in order to explain the observed differences. It was concluded that a larger zone with a high emissive source term in parallel mode improved the radiative heat transfer to the cooling tubes. Combined with a lower rate of destruction of momentum, leading to an increase in convective heat transfer to the cooling tubes, the total efficiency was higher in parallel mode. Additionally, in staggered mode, due to the interaction between the burners, the distance to the point of confluence was shorter, resulting in less entrainment to the jets. Thus, higher peak temperatures and radical concentrations were present in the combustion zone, and higher production of NO_x via the thermal and N_2O intermediate pathways in staggered mode were observed.

Chapter 5

Parametric study on multi-burner furnace

A parametric study on a 300 kW_{th} furnace equipped with three pairs of regenerative flameless combustion burners has been performed. Each burner pair has a rated thermal power of 100 kW_{th} firing Dutch natural gas. The objective of the study was to optimize the furnace performance, i.e., to maximize the cooling tube efficiency and minimize the CO and NO emissions. In the study the following parameters were varied: the positions of the burners in the furnace (burner configuration), the firing mode (parallel and staggered), the excess air ratio (λ) and the cycle time (t_{cycle}). Also, the influence on the furnace performance of the jet momentum of the combustion air and the temperature uniformity in the furnace were studied.

It was concluded that staggered firing mode is disadvantageous, since it results in significantly higher NO emissions than parallel firing mode. Also, out of the five investigated burner configurations one has been exempted, since its cooling tube efficiency was significantly lower compared to the other configurations. Furthermore, a horizontal setup of the firing burners improved the cooling tube efficiency at a fixed temperature uniformity. Also, for the burner configurations with the firing burners positioned closer to the regenerating burners and further from the stack, the temperatures in the regenerators were higher, leading to higher combustion air preheat temperatures. The temperature in the regenerators was also influenced by the cycle time; higher cycle times leading to higher (peak) temperatures in the regenerators. Finally, this temperature in the regenerators was shown to be more decisive for the final amount of CO emitted than the excess air ratio or the jet momentum. In all experiments, due to differences in path length of the mean flow, higher CO emissions were measured in the flue gas from the regenerators compared to in the flue gas from the stack. These two trends in the CO emissions were not observed for the NO emissions.

The contents of this chapter have been published in *Applied Thermal Engineering*, Parametric optimization study of a multi-burner flameless combustion furnace, B. Danon, E.-S. Cho, W. de Jong and D.J.E.M. Roekaerts, 2011;31(14-15):3000-3008.

5.1 Introduction

Energy efficiency and clean combustion are two main issues in fossil fuel utilization. Control of nitrogen oxides (NO_x) has been a major issue in designing combustion systems, since NO_x plays a key role in acid rain formation and the generation of photochemical smog. Flameless combustion, also known as Flameless Oxidation (FLOX) [8], High Temperature Air Combustion (HiTAC) [5] or Moderate or intense low-oxygen dilution (Mild) combustion [21], is a promising combustion technology capable of accomplishing the combination of high efficiency and low emissions. It is based on delayed mixing of fuel and oxidizer and high flue gas recirculation. High momentum injection of the separated fuel and air flows entrain the flue gas through internal recirculation, thus diluting the oxygen concentration in the combustion zone. This leads to a more distributed heat release rate of the chemical energy, avoiding high peak temperatures and reducing the thermal formation of NO [16].

Since the introduction of flameless combustion in the early nineties of the last century, many universities and research departments of industry have made efforts in experimentally investigating this new technology. These studies have been performed on many different scales, from small jet-in-hot-coflow setups up to full industrial size furnaces. However, before wide industrial application of this technology can be established, more in-depth knowledge of its behaviour in industrial scale environments needs to become available, especially in (regenerative) multi-burner systems. The most important previous experimental studies that include multi-burner regenerative systems are discussed below.

At the fall of the second millennium, a 200 kW_{th} HiTAC furnace has been commissioned at the Kungliga Tekniska Högskolan, Stockholm, Sweden [39]. In the furnace two pairs of NFK-HRS-DF regenerative burners firing natural gas and LPG were installed [42]. The two pairs of regenerative burners could be operated in three different firing configurations and the performance of the furnace has been compared extensively for these firing configurations [41, 67, 86].

In 2002 an extensive research program was performed at the IFRF research station in IJmuiden, the Netherlands [49]. The heating source in the furnace was one pair of NFK-HRS-DL4 regenerative burners, with a maximal thermal input of 1000 kW_{th}. Several types of fuel were investigated (natural gas, coke oven gas), while the objectives of the experiments were to generate extensive experimental datasets for the development and validation of CFD simulations.

A third large research project on regenerative flameless combustion was performed on a 200 kW_{th} furnace at the Faculté Polytechnique de Mons, Belgium [52]. One autoregenerative REGEMAT burner firing natural gas was used as the heating source. A comparison of the experimental data with CFD simulations was the main objective. In particular the heat transfer, temperatures and NO_x concentrations were compared.

Furthermore, at the NKK steel corporation in Japan, a slab reheating furnace with four pairs of regenerative burners was successfully fired with the by-product gas of the steel making factory [54, 55]. The total thermal power input was 2919 kW_{th} and the heat sink was a moving slab in the bottom of the furnace. Also here, the obtained results served as validation data for CFD simulations of the furnace.

As can be concluded, although the above mentioned experimental studies are performed on furnaces equipped with either a single autoregenerative burner or multiple regenerative burner pairs, none of them investigated the influence of the positions of the burners. The positioning of the burners can have a large influence on the furnace performance, especially in a regenerative (transient) environment. Therefore, investigation of the influence of burner positioning, such as burner–burner or burner–stack interactions, is required.

In this chapter results are presented of an experimental campaign on a furnace equipped with three pairs of regenerative flameless combustion burners. An important degree of freedom in the experiments was the positioning of the three burner pairs. The objective is to investigate and, where possible, optimize the multi-burner furnace performance for the variation of four parameters. These parameters are the burner configuration, the firing mode, the excess air ratio and the cycle time. The optimization of the furnace performance is defined as the maximization of the cooling tube efficiency and minimization of the CO and NO emissions.

5.2 Experimental setup

A furnace equipped with three pairs of regenerative flameless combustion burners has been designed, built and commissioned at Delft University of Technology. In Figure 5.1 a sketch of the furnace is presented. Each pair of regenerative flameless combustion burners has a rated thermal power of 100 kW_{th}, thus 300 kW_{th} in total. The fuel fired is Dutch natural gas, which has a net (lower) calorific value of 31.669 MJ/m^3 and consists of around 81%-vol CH_4, 3%-vol C_2H_6, 1%-vol other higher hydrocarbons, 14%-vol N_2 and 1%-vol other inert gases [116]. The burners were manufactured by WS Wärmeprozesstechnik GmbH and are of the REGEMAT CD 200 B type. Each burner has four combustion air/flue gas nozzles (d=20 mm) around a central fuel nozzle (d=12 mm).

The burners can operate in two different modes, i.e., flame and flameless mode. In flame mode the air and fuel are mixed in the burner before injection and the mixture is injected through the air nozzles only. An electric spark igniter is used in flame mode for ignition. In flameless mode the combustion air is injected through the air nozzles and the fuel is injected separately through the fuel nozzle. In this mode no igniter is necessary because the temperature in the furnace is above the self-ignition temperature of the fuel/air mixture. During the heating up of the furnace the burners fire in flame mode. Once the

temperature in the furnace exceeds 850 °C (which is above the self-ignition temperature of the fuel/air mixture) the burners switch to flameless firing mode automatically. In this chapter only results from the burners firing in flameless mode are presented.

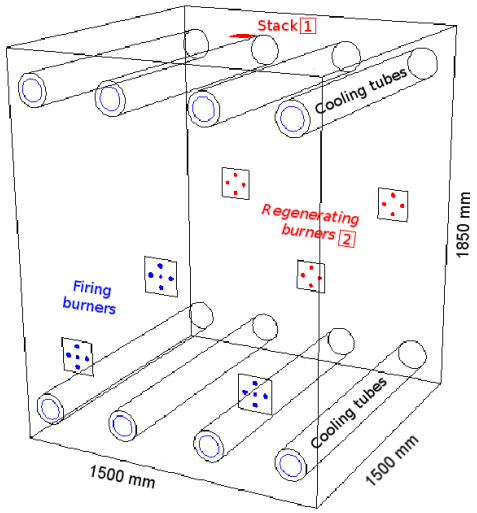

Figure 5.1: Furnace sketch. The boxed numbers 1 and 2 indicate the two sample positions for the flue gas. Sampling point 2 is after the regenerators. All dimensions are in mm. The sketch represents burner configuration C5 firing in parallel mode (see also Table 5.1).

The furnace has inner dimensions of 1500 x 1500 x 1850 mm (length x width x height). The insulation consists of three layers of ceramic bricks, together 300 mm thick. During the experiments the wall temperature of the furnace was measured at various locations with slightly protruding thermocouples type S. Additionally, the temperature of the regenerated flue gases and the cooling air was measured with thermocouples type K. The measurement error of these thermocouples is around 2–5 K. One of these measurements, a double-fitted thermocouple in the side wall close to the reaction zones, was determined to characterize the temperature in the furnace. Also, the temperature of the preheated air was measured in two burners (one burner pair). The fuel and combustion air flow rates are measured by custom-made orifice plate differential pressure meters. The combustion air flow rate is controlled by manual valves, allowing the variation of the excess air ratio.

Heat recirculation of the hot flue gases is achieved by regeneration. Eighty percent of the flue gases is sucked by a fan via the air nozzles of the regenerating burners over a ceramic honeycomb, while the remaining twenty percent leaves the furnace directly via the central stack at the roof. During regeneration the sucked flue gas traverses the ceramic honeycomb heat exchangers situated inside the burners. The inlet temperature is between 800 and 900 °C and the outlet temperature is between 110 and 140 °C, under steady state conditions. The volume flow of all the regenerated flue gas is measured using a vortex

flow meter.

The thermal load is simulated by a cooling system which consists of eight single-ended cooling tubes, four placed at the bottom of the furnace and four at the top. Every cooling tube consists of two concentric tubes; the cooling air enters the inner tube, turns at the end and flows back through the annulus between the two tubes. This design was made to minimize the temperature gradients along the length of the outer tube, thus, creating an as uniform as possible heat extraction distribution. The cooling air flow is measured using thermal mass flow meters and its inlet and exit temperatures are measured with type K thermocouples.

Additionally, a Sick Maihak S710 gas analyzer monitors the flue gas composition in two positions, i.e., in the stack and after the regenerators, see also Figure 5.1. Using NDIR the concentrations of the pollutants (CO and NO) are determined. The average error in these emission measurements is $\pm$ 7 ppm. In the same positions the O_2 concentration is determined paramagnetically for normalization purposes, with an accuracy of around $\pm$ 0.4 %-vol. All the data are stored by a data acquisition system every second.

In total eighteen flanges for the burners are divided over two opposite sides of the furnace (nine each). In this way, it is possible to investigate different burner configurations in the furnace.

5.3 Experimental campaign

Many different parameters were varied. In Table 5.1 all different parameters and their variation are summarized. The 'burner configuration' is defined as the physical position of the burners. The 'firing mode' is defined as which burners form a firing-regenerating pair. In parallel mode three burners fire at the same side, while in staggered mode two burners fire at one side and one burner at the opposing side, see also Table 5.1. Finally, the 'cycle time' (t_{cycle}) is defined as the total time of a complete firing and regenerating period of one burner.

The thermal performance of the furnace is characterized by the cooling tube efficiency, which is calculated by the difference in the sensible heat of the incoming and outflowing cooling air, which is subsequently divided by the total power input based on the net (lower) calorific value of the fuel.

The reported values of λ are a representation of the measured O_2 concentration in the flue gas from the stack. The O_2 concentration has been converted to λ with the following equation,

$$\lambda = \frac{20.9}{20.9 - [O_2]} \tag{5.1}$$

where $[O_2]$ is the molar oxygen percentage on dry basis.

Table 5.1: Overview of the experiments. The burner configurations are depicted by the two sidewalls of the furnace with burner flanges (large circles), with numbers 1 to 6 the positions of the burners and the small circles denoting the positions of the cooling tubes. In parallel firing mode burners 1-2-3 fire simultaneously while 4-5-6 regenerate, et vice versa. In staggered firing mode burners 1-3-5 are firing while 2-4-6 regenerate, et vice versa.

Burner configuration		**Firing mode**	**Cycle time (sec)**	**Excess air ratio (-)**
C1	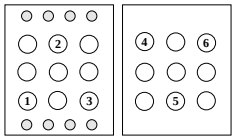	parallel staggered	20, 40, 60	1.05–1.35
C2	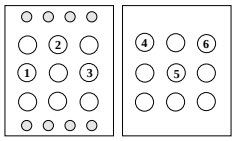	parallel staggered	20, 40, 60	1.05–1.35
C3	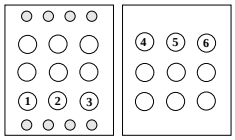	parallel staggered	20, 40, 60	1.05–1.35
C4	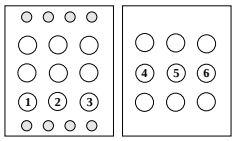	parallel staggered	20, 40, 60	1.05–1.35
C5	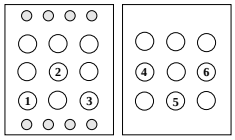	parallel staggered	20, 40, 60	1.05–1.35

The spatial temperature uniformity (T_u) is defined as in the following equation,

$$T_u = 1 - \sqrt{\frac{1}{N}\sum_{i=1}^{N}\left(\frac{(T_i - \bar{T})}{\bar{T}}\right)^2} \tag{5.2}$$

where N is the total number of temperature measurement positions, T_i is the temperature in the ith position and $\bar{T}$ is the mean of all the temperature measurements. The value of the T_u is between 0 and 1, where the value 1 indicates a perfectly uniform furnace. In the furnace the wall temperatures were measured with type S thermocouples in 18 different positions. Of these thermocouples, 12 are positioned in the unused burner flanges (see the empty circles in Table 5.1), while the remaining six are evenly divided over the other two side walls of the furnace.

The presented data are averages of a five to ten minutes period of steady state operation and a round number of cycles.

5.4 Results and Discussion

In this section the experimental results are discussed discriminated by the variation in the following parameters; the firing mode, the burner configuration, the excess air ratio (λ), the combustion air momentum, the cycle time (t_{cycle}) and the spatial temperature uniformity (T_u). For every parameter the influence on the cooling tube efficiency and the emissions are assessed.

Before proceeding to the parametric results, a remark is made on the emission measurements. In Figure 5.2 the measured concentrations in the flue gas in the stack and from the regenerators are presented. The presented data is from configuration C3, but similar results were found for the other configurations. For these two flue gas sampling locations, see the boxed numbers in Figure 5.1.

The values of NO in both flue gas streams are comparable to each other and to values measured in other flameless combustion furnaces [28, 41, 49]. However, for the CO concentrations large differences are observed between the two flue gas streams. In the stack flue gas, no significant amounts of CO are detected, whereas in the regenerator flue gas small amounts of CO are detected. This is explained by the difference in pathlength of the mean flow; the pathlength of the mean flow of the gases from a firing burner is shorter to a regenerating burner compared to its pathlength to the stack. Due to the longer pathlength to the stack, more CO is allowed to be converted to CO_2 before leaving the furnace. It is concluded from these observations that the distance between the firing and regenerating burners in the present furnace is too short for the size of the burners.

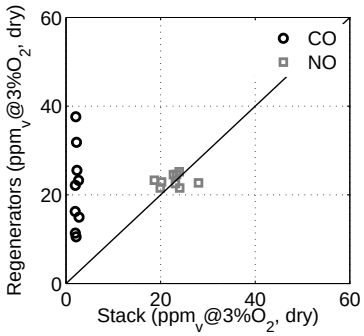

Figure 5.2: Emission measurements ($ppm_v@3\%O_2$, dry) in the flue gas from the stack and from the regenerators for burner configuration C3 firing in parallel mode.

In the parametric results below, the presented CO concentrations are the measured concentrations in the regenerator flue gas. The presented NO concentrations are the average of the measured concentrations of both flue gas streams.

5.4.1 Firing mode

In this section the two different firing modes, i.e., parallel and staggered, are compared. For details about these firing modes see Table 5.1.

In Figure 5.3(a) and (b) the cooling tube efficiency and the temperature uniformity are presented, respectively. Firstly, it is observed in Figure 5.3(b) that in staggered firing mode the temperature in the furnace is less uniform compared to the cases firing in parallel mode. However, considering Figure 5.3(a), these lower temperature uniformities do not result in lower cooling tube efficiencies. Actually, there are no significant differences in the cooling tube efficiency between the two firing modes.

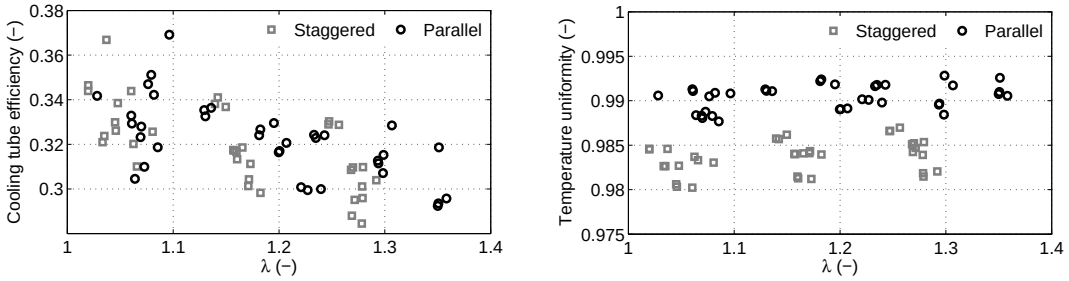

(a) (b)

Figure 5.3: (a) Cooling tube efficiency (-) and (b) temperature uniformity (-) for the different firing modes for all burner configurations, values of λ and cycle times.

It is noted here that the values of the cooling tube efficiency are lower than those of other furnaces, e.g., cooling tube efficiencies in KTH furnace are between 0.41 and 0.48 [67]. This is due to the fact that the burners in the KTH furnace use all the flue gases for regeneration, whereas the present burners use only 80%-wt of the flue gases for regeneration. The remaining 20%-wt of the flue gases is leaving the furnace at high temperature via the central stack.

In Figure 5.4(a) and (b) the CO and NO emissions are compared, respectively. For the CO emissions, there are no significant differences between the two firing modes. However, it can be observed in Figure 5.4(b), that the NO emissions in staggered mode are systematically higher than in parallel mode, for all the experiments. This difference in NO emissions for different firing modes has also been reported previously [41, 86] and has been discussed in the previous chapter. The increase in NO formation in staggered

mode is caused by a shorter distance between the comburant nozzles and the point of confluence of the comburants. This shorter distance allows less flue gas to be entrained before the fuel and oxidizer mix [67].

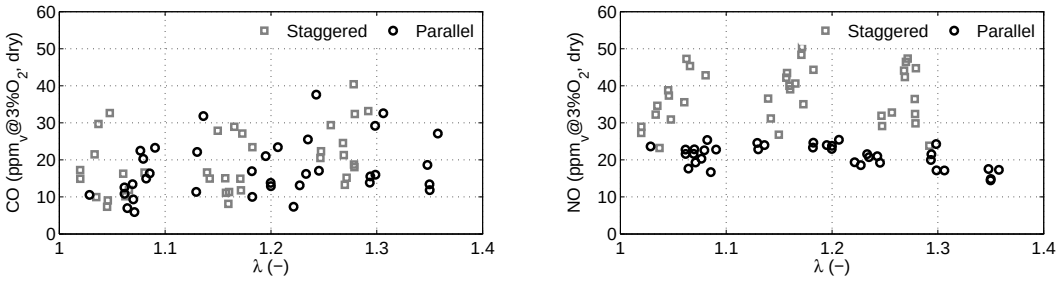

Figure 5.4: (a) CO and (b) NO emissions ($ppm_v@3\%O_2$, dry) for the different firing modes for all burner configurations, values of λ and cycle times.

It is concluded that in staggered firing mode, comparable cooling tube efficiencies are achieved as in parallel firing mode. However, regarding the emissions, staggered mode produces more NO at comparable thermal performance. Therefore, staggered firing mode is regarded as disadvantageous and is excluded from the following discussions.

5.4.2 Burner configuration

In Figure 5.5 the cooling tube heat extraction rates for all the configurations are compared. It is shown that configuration C2 has a significantly lower cooling tube heat extraction compared to the other burner configurations. This is due to the fact that in configuration C2 all the burners are positioned in the upper two rows in the furnace, see also Table 5.1. Due to this fact, there are less flue gases flowing through the lower part of the furnace (note that the central stack is in the furnace roof), resulting in significant lower heat extraction by the lower cooling tubes. Based on these results it was decided to exclude configuration C2 from further investigation.

In Figure 5.6(a) and (b) the preheat temperature of the combustion air and the exit temperature of the regenerated flue gas are presented. A difference in these temperatures is observed for burner configurations C1 and C3 on the one hand, and configurations C4 and C5 on the other hand. The temperatures are consistently lower for C1 and C3, over the whole range of λ compared to C4 and C5. There are two explanations for the observed lower preheat and exit temperatures in configurations C1 and C3. In the first place, a shorter distance between the upper level burners and the stack in the roof in configurations C1 and C3, causes relatively more flue gas to flow towards the stack. This difference was

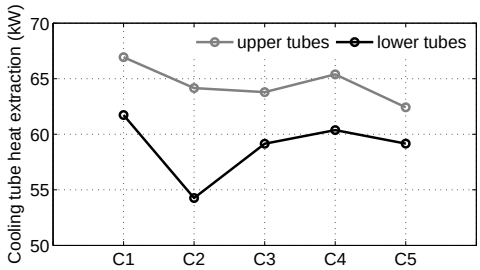

Figure 5.5: Cooling tube heat extraction (kW) versus all burner configurations for parallel firing mode, λ = 1.1 and t_{cycle} = 20 sec.

confirmed by the measured values of the flue gas flow from the regenerators. Due to this burner–stack interaction, less flue gas is available for regeneration. Secondly, in these cases, the flue gases from a firing burner on the lower level, travelling to a regenerating burner on the higher level, have a longer pathlength, and thus a longer residence time in the furnace. This burner–burner interaction results in more heat exchange with the cooling tubes and furnace walls.

Finally, the differences in cooling tube efficiencies and CO and NO emissions between the remaining four burner configurations were too small compared to the influence of parameters that could not be controlled, such as the ambient temperature or the preheating time of the furnace, to draw solid conclusions.

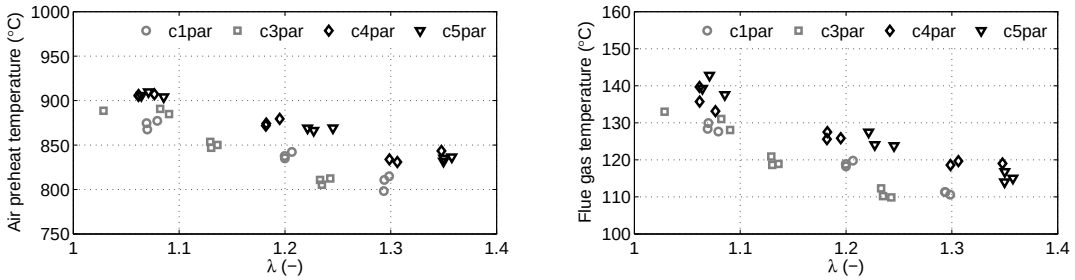

(a) (b)

Figure 5.6: (a) Combustion air preheat temperatures and (b) regenerated flue gas exit temperature (°C) for parallel firing mode and all values of λ and t_{cycle}.

5.4.3 Excess air ratio

In Figure 5.7 the cooling tube efficiency is shown versus the excess air ratio λ for all burner configurations and cycle times. It is observed that the cooling tube efficiency

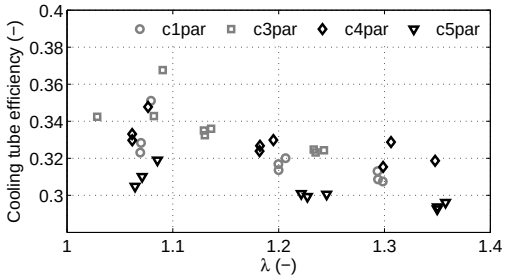

Figure 5.7: Cooling tube efficiency (-) versus λ (-) for parallel firing mode and all burner configurations and cycle times.

shows a decreasing trend with increasing λ. This is explained by the fact that the increase in λ is achieved by increasing the combustion air mass flow, at constant fuel flow. Thus, more inert gases from the air (mainly N_2) are introduced in the furnace, resulting in a lower energy content per unit mass flue gas and thus lower efficiencies.

The increase in the combustion air flow also influences the regenerative preheating of the combustion air. In Figure 5.6(a) in the previous section, it can be observed that for an increasing value of the λ, the preheat temperature of the combustion air is decreasing. As a result, also the exit temperature of the regenerated flue gas is lower, as shown in Figure 5.6(b).

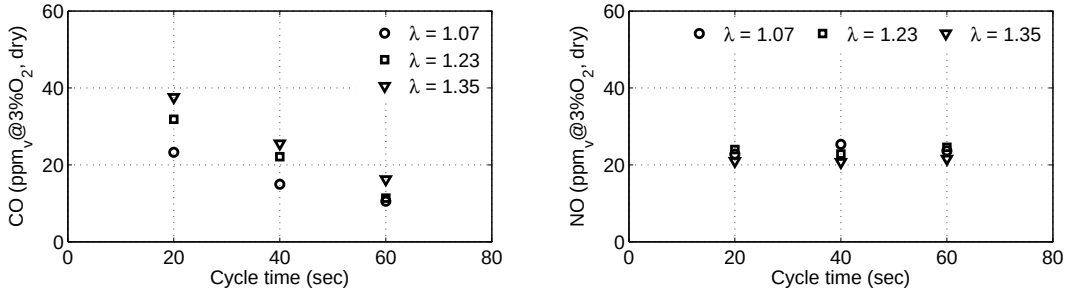

(a) (b)

Figure 5.8: (a) CO and (b) NO emissions ($ppm_v@3\%O_2$, dry) versus the cycle time for C3 configuration in parallel firing mode, for all values of λ.

In Figure 5.8(a) and (b) the CO and NO concentrations are presented for the C3 parallel experiment, respectively. The presented data is from configuration C3, but similar results were found for the other configurations. It is observed in (a) that higher values of λ causes slightly higher CO emissions. However, these differences are smaller than the effect of the cycle time, see for a discussion regarding the cycle time below. This

unexpected trend of increasing CO emissions at increasing λ (a higher λ implies higher concentrations of O_2 and thus less CO) is explained by the temperatures of the combustion air and flue gas. As shown in Figure 5.6(a) and (b), the air preheat temperature and regenerated flue gas exit temperature decrease with increasing λ. It is noted here that due to the increased combustion air mass flow at higher values of λ also the residence time will be shortened, however, these differences will be relatively small. Thus, two opposing effects are influencing the conversion of CO to CO_2; increased O_2 concentration is enhancing the reactions, whereas lower temperatures are slowing down the reactions. In these experiments the temperature has a stronger effect on the reactions, which is in accordance with what has been reported in the literature [117]. Finally, regarding Figure 5.8(b), the NO emissions are not correlated to the value of λ, at least not within the investigated range.

In conclusion, considering both the cooling tube efficiency and the CO emissions, a value of λ closest to unity is optimal. It is noted here that the observed differences in the CO emissions are strongly related to the regenerative preheating of the combustion air.

5.4.4 Combustion air momentum

In the literature it is mentioned that flameless combustion is achieved by high internal flue gas recirculation, which in turn is realized by discrete high momentum injection of the comburants [5, 8]. The momentum of the combustion air jet is calculated by Equation 5.3,

$$G = \frac{RT_{\text{preheat}}(\Phi_{\text{m,air}}^{\text{burner}})^2}{p^{\circ} M_{\text{air}} A_{\text{n}}} \tag{5.3}$$

where G stands for jet momentum (N), R is the universal gas constant (J/molK), T_{preheat} is the temperature of the preheated combustion air (K), $\Phi_{\text{m,air}}^{\text{burner}}$ the mass flow of combustion air (kg/s), p° the pressure in the furnace, which is atmospheric, (Pa), M_{air} the molecular weight of air (kg/mol) and A_{n} the area of the air nozzles (m^2). Note that since the mass flow and temperature of the fuel jet are equal for all experiments the fuel jet momentum is also equal for all cases and the trends in the air jet momentum are equal to the trends in the momentum ratio. In these burners the average inlet velocity of the combustion air and fuel jets is around 100 and 30 ms^{-1}, respectively.

Firstly, the parameters influencing the jet momentum are discussed. In Figure 5.9(a) and (b) the combustion air jet momentum is presented as a function of the air mass flow and the air preheat temperature. As expected from the equation, the jet momentum is increasing for increasing air mass flow. Contrarily, the jet momentum is decreasing with increasing air preheat temperature, i.e., decreasing air mass flow or λ. Thus, the air mass flow has a stronger influence on the jet momentum, which is confirmed in the equation, where the air mass flow is squared.

Secondly, the effect of the air jet momentum on the furnace performance is investi-

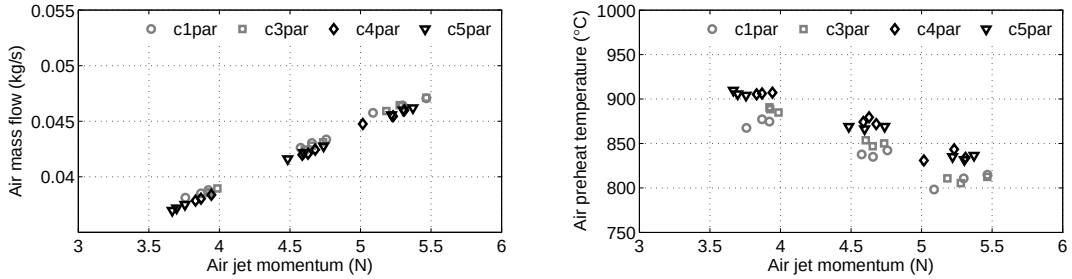

(a) (b)

Figure 5.9: Correlation between the combustion air jet momentum (N) and (a) the mass flow (kg/s) and (b) the preheat temperature (°C) of the combustion air for all configurations firing parallel mode and all values of λ and cycle time.

gated. In Figure 5.10 the cooling tube efficiency is presented versus the combustion air jet momentum. It is noted that the efficiency is decreasing for an increase in the jet momentum. This is in accordance with the trend observed for the cooling tube efficiency as a function of the λ, see also Figure 5.7. Actually, in this case the trend is even more pronounced, since the jet momentum incorporates both the effects of the air mass flow, i.e., the λ, and the preheat temperature.

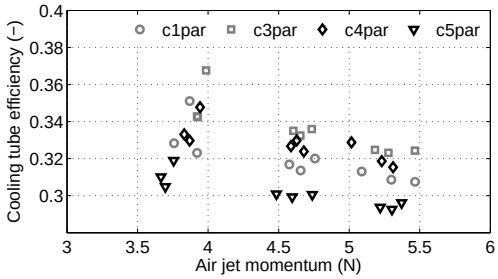

Figure 5.10: Cooling tube efficiency (-) versus air jet momentum (N) for all configurations firing parallel mode and all values of λ and cycle time.

In Figure 5.11(a) and (b) the emissions of CO and NO as a function of the jet momentum are presented, respectively. The CO emissions are increasing with an increasing jet momentum. Although an increasing jet momentum indicates increased oxygen concentration and increased internal flue gas recirculation (two effects enhancing the CO to CO_2 conversion), still the decrease in the air preheat temperature has the largest influence on this conversion. It is concluded that in this furnace the preheat temperature of the air is an important parameter for the emission of CO.

The NO emissions show no significant correlation with respect to the jet momentum.

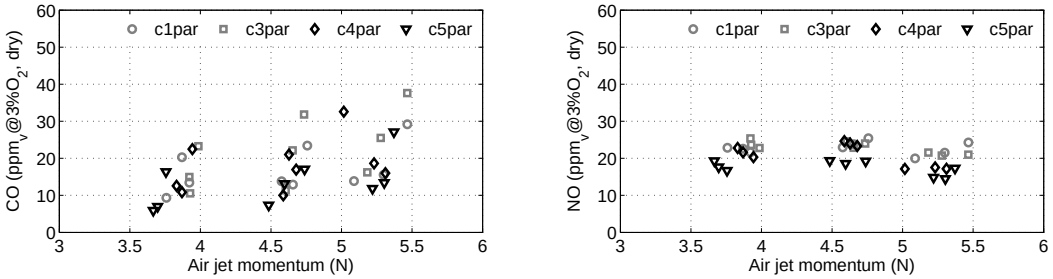

(a) (b)

Figure 5.11: (a) CO and (b) NO emissions ($ppm_v@3\%O_2$, dry) versus combustion air jet momentum (N) for all configurations firing parallel mode and all values of λ and cycle time.

Since the NO emission values are also low, it shows that the 'flamelessness' of the burners suppresses possible increases in the NO emissions due to the increase in preheat temperature or oxygen availability.

5.4.5 Cycle time

In Figure 5.8(a) and (b) the CO and NO emissions were presented as a function of the cycle time for burner configuration C3, respectively. The NO emissions are not significantly affected by the change in cycle time. However, the CO emissions show a clear dependency with the cycle time; lower CO emissions are measured at longer cycle times.

This trend is due to the additional conversion of CO to CO_2 in the flue gas in the regenerators. Actually, the flue gas at the hot side of the regenerators has a temperature of around 850 °C, cf. the air preheat temperature, see also Figure 5.6(a). At these temperatures the above-mentioned reaction has significant rates [117].

In Figure 5.12(a) and (b) the temperature at the cold and hot side of the regenerators of one burner are presented for a period of three entire cycles for all values of t_{cycle}. The presented data is from configuration C3, but similar results were found for the other configurations. It is noted here that the presented temperatures were measured in a burner that regenerates the first half of the cycle, and fires the second half. It is observed that in case of longer cycle times, the maximum temperature of the flue gas entering the regenerators, i.e., the first half of the cycles in (b), is higher and that this maximum temperature is reached relatively faster. Also, the exit temperature of the flue gas is higher for longer cycle times, as can be seen in the first half of the cycles in (a). Thus, in the cases with longer cycle time, the flue gases cross the regenerators at higher temperatures and, relatively to the entire cycle time, for a longer time at these high temperatures. This explains the lower measured CO levels for longer cycle times.

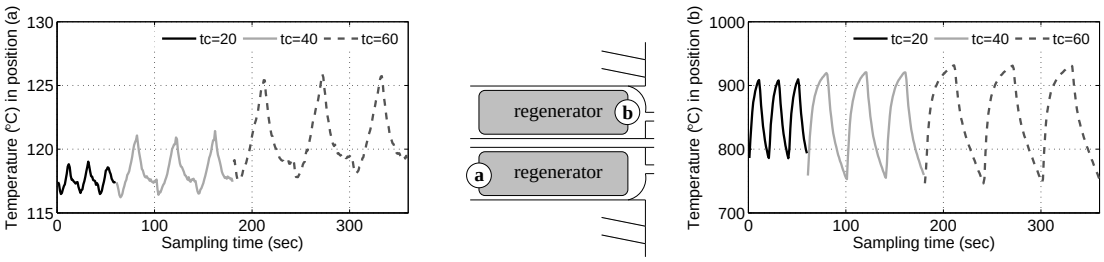

(a) (b)

Figure 5.12: Temperature (°C) at the cold side, position (a), and at the hot side, position (b), of the regenerator of one burner during configuration C3, parallel firing mode, λ = 1.2 and all cycle times. The actual measurement positions of Figures (a) and (b) are represented in the sketch of the burner by the encircled a and b, respectively. For every cycle time three entire cycles are presented, with the first half of the cycle a regenerating period.

As a next step, the relative emissions of CO and NO, at a constant value for the λ and t_{cycle}, are calculated with Equation 5.4,

$$\text{Relative emission} = \left(\frac{x_i}{x_{i,\max}} \right)_j \tag{5.4}$$

where x_i is the mole fraction (-) of species i (either CO or NO) and j represents either at constant λ or t_{cycle}. Every case is part of a series obtained by variation of λ (and thus at constant t_{cycle}), and part of a series obtained by variation of the cycle time (and thus at constant λ). The relative emission is calculated twice for each case, i.e., as part of one of these two series. For all cases the two relative emissions are plotted versus each other in Figure 5.13.

It is observed that the relative NO emissions are randomly scattered around the 'parity line', which indicates that none of the two effects (λ or t_{cycle}) has a significant larger influence than the other. Also, the values are close to unity, indicating that the differences in the NO emissions between the cases are small.

However, most of the CO relative emissions are below the 'parity line'. This clearly indicates that a change in the λ (along the x-axis) has a smaller effect on the CO emissions than a change in the cycle time (along the y-axis). In other words, while the cycle time has no effect on the NO emissions, it does affect the CO emissions, see also Figure 5.8. Moreover, the effect of the cycle time on the CO emissions is larger than the effect of the λ.

Finally, the cooling tube efficiency showed no relation with the variation of the cycle time.

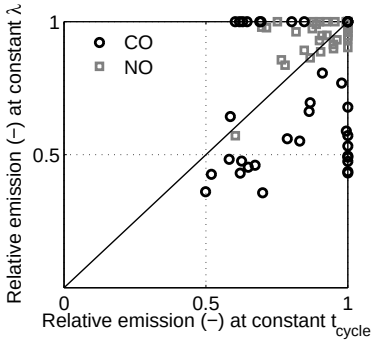

Figure 5.13: Relative CO and NO emissions (-) at constant t_{cycle} and λ, for all burner configurations in parallel firing mode.

5.4.6 Temperature uniformity

In many publications it is reported that flameless combustion is achieving a more uniform temperature distribution compared to conventional combustion and that this higher temperature uniformity results in higher efficiencies [35, 100].

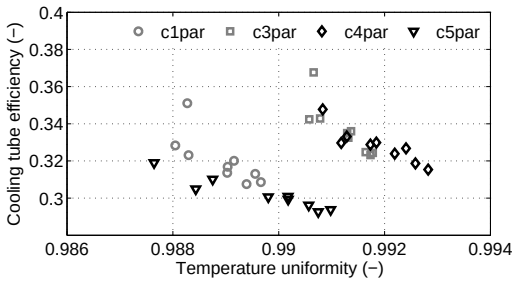

Figure 5.14: Cooling tube efficiency (-) versus temperature uniformity (-) for all burner configurations in parallel firing mode and all values for λ and cycle time.

To verify whether this hypothesis holds for different cases under flameless combustion conditions, the temperature uniformity is presented versus the cooling tube efficiency in Figure 5.14. Note that a value of unity for the temperature uniformity represents perfect uniformity, whereas a decreasing value of the temperature uniformity indicates an increase in the temperature gradients in the furnace.

Considering the burner configurations separately, the cooling tube efficiency shows a decrease with increasing temperature uniformity. This contradicts the general validity of the above mentioned hypothesis.

Furthermore, it is observed that burner configurations C1 and C5 together tend to a linear correlation with the temperature uniformity, as configurations C3 and C4 do. In

this view, a horizontal setup of the firing burners (C3 and C4) behaves differently from a triangular setup of the firing burners (C1 and C5, see Table 5.1). Additionally, the horizontal firing setup achieves higher cooling tube efficiencies, compared to the triangular firing setup, for the same values of the temperature uniformity. The same observation can be made in Figure 5.10. Therefore, the observed trends in Figure 5.14 are related to burner–burner interactions.

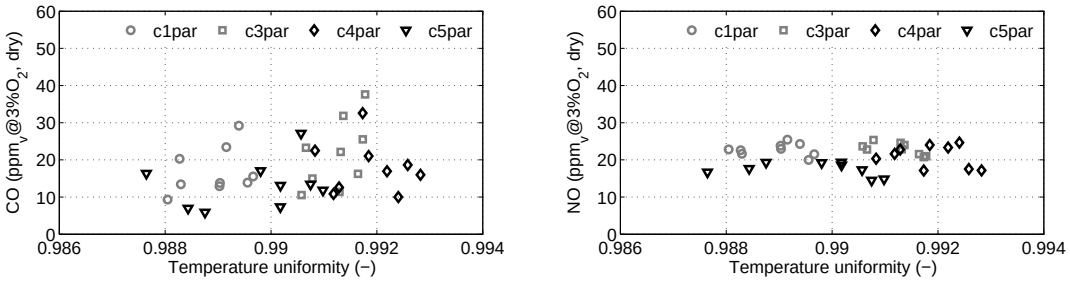

(a) (b)

Figure 5.15: (a) CO and (b) NO emissions (ppm_v@3%O_2, dry) versus the temperature uniformity (-) for all burner configurations in parallel firing mode and all values of the cycle time and λ.

Finally, in Figure 5.15(a) and (b) the CO and NO emissions are presented as a function of the temperature uniformity. For the formation of both pollutants no clear correlation with the temperature uniformity could be identified.

5.5 Conclusions

A parametric study has been performed on a multi-burner flameless combustion furnace with the objective of optimizing the furnace performance, i.e., maximizing the cooling tube efficiency and minimizing the emissions (CO and NO). From a first observation, regarding the difference in CO emissions in the flue gas from the regenerators and in the central stack, the present furnace is too small for the size of the burners.

For the optimization of the furnace performance, two conditions could be ruled out. First, staggered firing mode has been ruled out mainly due to higher NO emissions. Secondly, burner configuration C2 (see Table 5.1) was exempted, since the cooling tube efficiency was significantly lower compared to the other burner configurations.

Furthermore, it was observed that for burner configurations C4 and C5, with the burners positioned in the middle and lower levels in the furnace, the combustion air preheat and flue gas exit temperatures are higher than for burner configurations C1 and C3. However, this trend was not reflected in the CO emissions. Then, configurations C3 and C4,

with a horizontal setup of the firing burners, showed better cooling tube efficiencies than configurations C1 and C5, at comparable values of the temperature uniformity. It was also shown that with an increase in the λ, the cooling tube efficiency decreased. However, although both the oxygen availability and the internal flue gas recirculation are increased with an increasing λ, also the CO emissions increased. This was due to decreased temperatures in the regenerators. Finally, it was observed that for different cases under flameless combustion conditions, the cooling tube efficiency showed a decreasing trend with increasing temperature uniformities.

Although no distinct optimal case could be identified, some conditions could be exempted. Moreover, it was shown that the positioning of the burners, and thus the burner–burner and burner–stack interactions, influenced the performance of the furnace.

These experimental results will serve as validation data for a set of Computational Fluid Dynamics simulations of the furnace. The results of these simulations are presented in the next chapter.

Chapter 6

Numerical study on burner positioning in multi-burner furnace

In this chapter results are presented of a numerical study performed for four different burner configurations in a furnace equipped with three pairs of flameless combustion burners firing Dutch natural gas. The simulations have been validated against the experimental data presented in the previous chapter. The commercial Computational Fluid Dynamics (CFD) code Fluent 6.3 was used for the calculations. Using the Eddy Dissipation Concept (EDC) model for turbulence-chemistry interaction in combination with the realizable k-ε model for turbulence and a skeletal chemistry mechanism, the main furnace performance was consistently reproduced for all the investigated burner configurations. Moreover, it was found that predictions of the heat extraction rates of the cooling tubes were improved by treating the flow in the cooling tubes as laminar. Furthermore, the applied error tolerance of the ISAT procedure was insufficient for accurate species concentration predictions, however, based on analysis of the main species concentrations in the flue gas, this inaccuracy did not influence the overall predictions.

The most important experimental results have been investigated using the CFD simulations. Firstly, a longer path length from the firing burners to the stack, compared to the path length to the regenerating burners, explained the lower CO emissions in the flue gas in the stack. Secondly, a recirculation zone between the upper firing burners and the stack in configurations C4 and C5 resulted in a smaller fraction of the flue gases leaving the furnace via the stack. Thus, a larger fraction left the furnace via the regenerating burners and this resulted in higher preheat temperatures of the combustion air. Furthermore, more pronounced recirculation zones in configurations C3 and C4 led to higher temperature uniformities in the furnace. Finally, it was confirmed that the jets of the burners in configurations C1 and C3 showed similar merging behaviour, leading to similar NO emissions, as observed in the experiments.

The contents of this chapter have been published in *Applied Thermal Engineering*, Numerical investigation of burner positioning effects in a multi-burner flameless combustion furnace, B. Danon, E.-S. Cho, W. de Jong and D.J.E.M. Roekaerts, 2011;31(17-18):3885-3896.

6.1 Introduction

The industrial wish for higher energy efficiency of large-scale furnaces, and its associated fuel savings, has demanded for new combustion technologies, combining heat recirculation from the flue gas with low pollutant emissions. Flameless combustion (also known as flameless oxidation (FLOX) [8], HiTAC [5] or MILD combustion [21]) is such a novel combustion technique. In this technique the combustion air can be highly preheated, without increasing the pollutant emissions, in particular NO_x. The air and fuel are injected at high velocity and spatially separated. Due to this high-momentum injection, large quantities of hot flue gases are entrained into the jets before they mix with each other, lowering the oxygen availability in the reaction zone, thus, also lowering the local reaction rates and the peak temperatures. These low peak temperatures reduce the thermal NO emissions [16].

Since the introduction of flameless combustion in the early nineties of the last century, many universities and research departments of industry have made efforts in experimentally investigating this new technology. These studies have been performed on many different scales, from single open flames in jet-in-hot-coflow setups [15, 25] to (semi-) industrial scale test furnaces equipped with multiple burners [41, 45, 52, 54]. A focus is here on furnaces equipped with multiple flameless combustion burners.

Many of these experimental studies have been complemented with Computational Fluid Dynamics (CFD) simulations. In the following the quality of these simulations of furnaces with multiple flameless combustion burners and the choice of physical models in these simulations are discussed.

The 200 kW_{th} semi-industrial furnace at the Kungliga Tekniska Högskolan (KTH) has been simulated extensively using the STAR-CD CFD package [83]. Besides the standard k-ε turbulence model, several combustion models have been investigated, of which the combination of the Eddy Dissipation model and Finite Rate chemistry (ED/FR) turned out to give better results. A two-step chemical mechanism for the combustion of the fuel (LPG, i.e., propane), with CO as an intermediate, was used. Thermal radiation was calculated with the Discrete Transfer method and the absorption coefficient of the gases using the Weighted Sum of Gray Gases (WSGG) model. The cooling tubes were not incorporated in the simulation, but a temperature, based on measured temperatures, was set as a boundary condition. For the validation of the simulations measured heat fluxes, wall temperatures and in-furnace species concentrations were used [86]. The validation results were reasonable, however, the in-furnace temperatures, which this set of models is known to overpredict, were not compared. The three experimentally investigated firing modes, i.e., which combination of burners form a burner pair, were also investigated numerically. The main differences observed in the experiments were reproduced by the simulations. Initially, the analysis of the results was focused on the fundamental properties of flame-

less combustion. In a later study (firing natural gas) also the observed and reproduced differences between the firing modes were investigated numerically in more detail, see Chapter 4.

In 2004 Hekkens et al. simulated the experiments performed with the 1000 kW_{th} IFRF furnace firing natural gas using the Fluent CFD package [89, 90]. Again, the standard k-ε turbulence model was used. Three different combustion models were applied; two Probability Density Function (PDF) methods, assuming chemical equilibrium and laminar flamelets, and the ED/FR model. In this last model a two-step chemistry for the combustion of methane was used. Radiation was incorporated using the Discrete Ordinates method and the absorption coefficient was calculated with the domain based WSGG model. After detailed comparison of the numerical and experimental results, it turned out that the ED/FR model performed best regarding the species concentration predictions inside the furnace. The PDF methods were unable to correctly predict the temperatures inside the furnace, which can be explained by the fact that they assume (too) fast chemistry. However, also the ED/FR model overpredicted the peak temperatures inside the furnace, even though two model constants have been adjusted for flameless combustion purposes using previous IFRF measurements.

The 200 kW_{th} natural gas fired flameless combustion furnace at the Faculté Polytechnique de Mons has been simulated by Lupant et al. using the Fluent CFD package [51, 52, 91]. The standard k-ε turbulence model is applied, with a model constant adjusted for improved prediction of the spreading rate of the jets. Combustion modeling is done using both the PDF method assuming chemical equilibrium and the combinated ED/FR model. Again, as in the simulations for the IFRF furnace, two model constants in the ED/FR model were changed in order to improve the results. A one-step chemistry mechanism has been used for the combustion of methane. Radiative heat transfer is modeled using the Discrete Ordinates method and the WSGG model was used for the calculation of the absorption coefficient. Validation of the simulation is performed by comparison of the numerical results with in-furnace radiative heat flux, temperature and species measurements. Reasonable agreement was achieved for the heat fluxes, however, all simulations overpredicted the temperature inside the furnace. This difference was smaller in the simulation where the model constants in the ED/FR model were adjusted. Although the maximum concentrations of O_2 were predicted rather well, the concentration dropped too fast after its maximum. This indicates that the combustion reactions are too fast, which also explains the prediction of the temperatures being too high. Finally, it is noted that the modification of the model constant in the turbulence model improved the prediction of the delay in the reaction.

Several regenerative reheating furnaces at the NKK steel company firing Low Calorific Value gases were simulated by Ishii et al. using the Fluent CFD package [53, 54, 55]. Again, the standard k-ε model for turbulence is used. For the modeling

of the combustion the PDF method assuming chemical equilibrium is applied. Radiation is incorporated using the P-1 model and again the WSGG model was used for the absorption coefficient. Besides this standard set of models, a wide variety of models for turbulence, wall functions and PDF shapes were compared [92]. The simulations are validated against in-furnace temperature measurements [54]. The agreement is reasonable outside the combustion zone. Inside the combustion zone the temperatures are fairly overpredicted, as was observed also in the other simulations using a PDF method. After the validation of the simulation, several numerical investigations were performed [53, 55].

Generally, it can be concluded that combustion models assuming fast chemistry (e.g. PDF methods assuming chemical equilibrium) are not applicable for the simulation of flameless combustion. Also, a careful choice of the chemical mechanism is important.

At Delft University of Technology (DUT) a 300 kW_{th} furnace equipped with three pairs of flameless combustion burners, with the unique possibility to vary the positions of the burners in the furnace, has been investigated experimentally [65]. In this chapter the results of detailed CFD simulations of this furnace are presented. The objective of the simulations was to investigate and explain the observed trends in the furnace performance for the different burner configurations in the furnace.

6.2 Experimental setup

The furnace is equipped with three pairs of regenerative flameless burners. The burner pairs have a thermal power of 100 kW_{th} each, thus 300 kW_{th} in total. The furnace has inner dimensions of 1500 x 1500 x 1850 mm (length x width x height). The insulation consists of three layers of ceramic fire bricks, together 300 mm thick. In total 18 flanges for the burners are divided over two opposite sides of the furnace (nine each). In this way, it is possible to investigate different burner configurations in the furnace. The heat sink is made of eight single ended cooling tubes, four placed above the burners and four beneath, see also Figure 6.1 and Section 6.3.2.

The burners were manufactured by Wärmeprozesstechnik GmbH and are of the REGEMAT CD 200 type. Each burner has four combustion air/flue gas nozzles around a central fuel nozzle, with diameters of 20 mm and 12 mm, respectively. The burners have ceramic honeycomb heat exchangers (regenerators) incorporated. Eighty percent on mass basis of the flue gas is sucked by a fan via the air nozzles over these honeycombs (thus heating them) for regeneration of the heat, while the remaining twenty percent is leaving the furnace via the central stack at the roof. Three burners are firing simultaneously, while the other three burners are regenerating. After a preset time interval of 10 to 30 s they switch and the firing burners start regenerating, et vice versa. The cycle time (t_{cycle}) is defined as one periodic cycle, i.e., the sum of the firing and regenerating period for one burner. The experimental data with the highest cycle time (60 s) were taken for the present

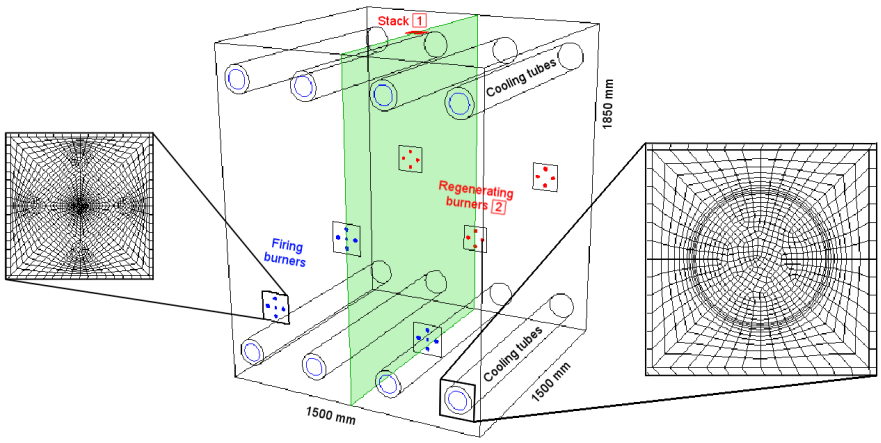

Figure 6.1: Furnace sketch, representing burner configuration C5 firing in parallel mode. The boxed numbers 1 and 2 indicate the two sample positions for the flue gas. Sampling point 2 is after the regenerators. The vertical symmetry plane is indicated by the (green) shaded plane. All dimensions are in mm. The two inserts show enlarged frontviews of the mesh around a burner (lefthand side) and a cooling tube (righthand side). The total mesh contains approximately 1.5 million hexahedral cells.

steady RANS simulations, since these experiments are considered to be closest to steady state operation. The data with an excess air ratio (λ) of 1.25 were used for the simulations. Dutch natural gas (DNG) was used as the fuel, which has a net (lower) calorific value of 31.669 MJ/m^3. The furnace operates at atmospheric pressure. Using an NDIR gas analyzer, the NO and CO concentrations in the flue gas from the stack and from the regenerators (boxed numbers 1 and 2 in Figure 6.1, respectively) were measured on-line. In the same positions the O_2 concentration was determined on-line paramagnetically for normalization purposes. More details on the experimental setup and results can be found in the previous chapter.

Four different burner configurations were investigated numerically. For all of these configurations the firing mode was parallel, indicating that all the firing burners are on one side of the furnace, while all the regenerating burners are on the other side of the furnace. In Figure 6.2 the simulated burner configurations are presented.

6.3 Numerical setup

A three-dimensional mesh of the furnace was generated using Gambit 2.4, see also Figure 6.1. The mesh contains approximately 1.5 million hexahedral cells. Exploiting the

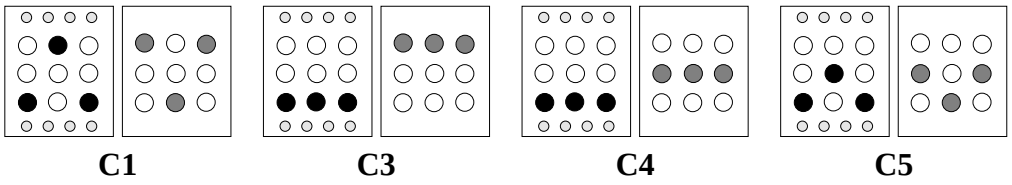

Figure 6.2: Overview of simulated burner configurations. The two rectangles represent the two side walls of the furnace with the burner flanges. The large circles represent the burner flanges, if filled black it is occupied by a firing burner, if filled gray it is occupied by a regenerating burner. The black and gray circles switch after a period of 30 s. The small circles denote the position of the cooling tubes.

symmetry of the furnace with respect to its vertical midplane, to reduce the computational time, only half of the furnace is meshed. The cooling tubes are entirely incorporated in the simulations.

The simulations were performed with the commercial code Fluent 6.3.26 [76]. The second order implicit steady solver was used with Green-Gauss cell based interpolation. A SIMPLE algorithm is used for pressure-velocity coupling.

The calculations were performed on a cluster with 4 dual core AMD Opteron 8222 (3.0 GHz) processors with 8 GB DRAM per processor, thus 32 GB in total. The simulations were calculated parallel on all eight nodes.

6.3.1 Furnace

For turbulence closure the realizable k-ε model was used. This model is shown to give improved results, compared to the standard k-ε model, for the prediction of round jets [97], as is the case in these burners.

For the combustion of the fuel the mechanism of Smooke et al. for the combustion of methane was applied [98]. This so-called skeletal mechanism consists of 16 species (resulting in 16 transport equations to be solved) and incorporates 46 reactions. It is noted here that a mechanism for the reaction of methane only is used. This implies that the Dutch natural gas (DNG) is replaced by a simulation fuel. This simulation fuel contains, as a fuel component, only methane, also replacing the higher hydrocarbons present in DNG, in such a way that the heat release per unit mass stays equal. In Table 6.1 the composition of the actual DNG and its simulation fuel is presented, see also Appendix A.

The turbulence-chemistry interaction is taken into account by using the Eddy Dissipation Concept (EDC) model [99]. The EDC model has been successfully applied for various turbulent and flameless combustion applications [100, 101]. Parente et al. compared results for flameless combustion with different turbulence-chemistry interaction models and chemistry mechanisms [102]. They concluded that the EDC model combined with a

Table 6.1: Composition of actual and simulation fuel for Dutch natural gas [116].

	DNG	
	Actual	Simulation
Component	%-mass	%-mass
CH_4	69.97	75.98
C_2H_6	4.63	-
C_3H_8	0.90	-
C_4H_{10}	0.47	-
C_5H_{12}	0.16	-
C_6H_{14}	0.23	-
O_2	0.02	0.02
N_2	21.52	21.87
CO_2	2.10	2.13

skeletal or full chemistry mechanism performed best. Additionally, Stefanidis et al. also compared the EDC model with the combined ED/FR approach [103]. They report that the main disadvantage of the ED/FR model is too fast reaction rates for the oxidization of the fuel. This disadvantage is especially undesired for flameless combustion applications, since in flameless combustion the reaction rates are relatively low. Finally, Kim et al. performed a study on the use of different chemistry mechanisms for the simulation of flameless combustion. The EDC model was used in all the test cases, since it was considered by the authors as a very suitable model for the simulation of flameless combustion [78].

The in situ adaptive tabulation (ISAT) procedure, for the efficient computation of homogeneous reactions in chemically reacting flows, has been applied [118]. The error tolerance of this procedure was stepwise decreased until a value of 10^{-4}. For one case, reported below, the error tolerance was decreased further to a value of 10^{-5}.

Radiative heat transfer is accounted for using the Discrete Ordinates method and the domain-based Weighted Sum of Gray Gases Model (WSGGM) for the absorption coefficient of the gas mixture. The mean beam length was based on the dimensions of the furnace since the flue gas composition inside the furnace is reasonably uniform and with this approach improved predictions of the radiation fluxes between the walls and cooling tubes are expected. The emissivity of steel was set to 0.8 and that of the firebrick insulation to 0.68.

The density of the mixture is calculated by the multicomponent ideal gas law using the low Mach number approximation $p = p_{ref}$. The molecular viscosity and thermal conductivity of the gas mixture are taken constant at 1.72×10^{-5} kg/ms and 0.0241 W/mK, respectively. The mass diffusivity is calculated by Fick's law with a constant and identical mass diffusion coefficient of 2.88×10^{-5} m^2/s for all species. Finally, the heat capacities

are determined per species with a temperature dependent piece-wise polynomial provided by Fluent, and for the mixture with the mixing law.

The heat losses through the walls were incorporated by calculating the convective and radiative heat flux to the environment. For a realistic value of the effective thermal conductivity of the walls, the predicted wall temperatures were compared with the experimental values.

In previous studies this set of models proved to be suitable for the simulation of flameless combustion in furnace environments [67, 119]. Additionally, De et al. performed a detailed comparison study of these and comparable models for experimental results of a jet-in-hot-coflow setup, which emulates flameless combustion [81]. Overall, the set of models was well capable of predicting flameless combustion. Moreover, it was shown that the realizable k-ε performed better than other two-equation turbulence models. Also, the use of the above-mentioned constant values for the viscosity and the species mass diffusivities showed no significant differences with simulations with a temperature dependent viscosity or using multi-component diffusion. The largest difference, compared to the experiments, was that the ignition was predicted to occur too early. Finally, a limitation of the use of the EDC model with a skeletal chemistry mechanism was demonstrated for flows with low turbulence Reynolds numbers. In the present furnace the Reynolds numbers were verified to be higher than the Reynolds numbers where these limitations become apparent.

6.3.2 Cooling tubes

In preliminary simulations of the furnace the heat extraction rate of the cooling tubes was fairly overpredicted. In order to investigate this difference a separate simulation was performed on a single cooling tube. The mesh of this single cooling tube is kept exactly the same as the mesh of a cooling tube in the mesh of the furnace. As a boundary condition the furnace temperature was set on the outer tube in this separate simulation.

Each cooling tube consists of two concentric annular tubes. Air was used as the cooling medium and enters the inner tube, turns at the end and flows back through the annulus between the inner and outer tubes. This setup was chosen to minimize the temperature gradients along the length of the outer tube, thus, creating an as uniform as possible heat extraction distribution. The inner tube has an internal diameter of 100 mm and penetrates 1282 mm into the outer tube, which in turn penetrates 1450 mm into the furnace and has a inner diameter of 150 mm. In Figure 6.3 a schematic representation of a single cooling tube is presented.

In order to characterize the flow regime inside the cooling tube the Reynolds number

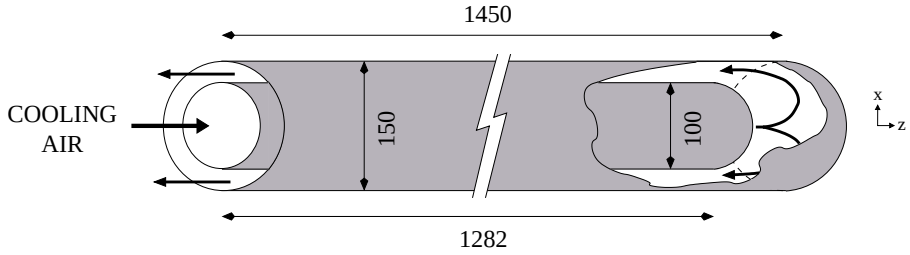

Figure 6.3: Schematic representation of a single cooling tube. All dimensions are in mm.

was calculated. The Reynolds number (Re) is defined in Equation 6.1,

$$\mathrm{Re} = \frac{\rho u d_h}{\mu} \tag{6.1}$$

where ρ is the mean density (kg/m^3), u the mean velocity magnitude (m/s), d_h the hydraulic diameter (m) and μ the molecular viscosity (kg/ms). The hydraulic diameter d_h is 0.1 m and 0.05 m for the inner tube and the annulus, respectively. The Reynolds number of the flow in the inner tube and annulus are around 20,000 and 10,000, respectively. These values indicate that the flow in the inner tube is turbulent, however, in the annulus it is in the range of Reynolds numbers that indicate the transition regime between laminar and turbulent flow.

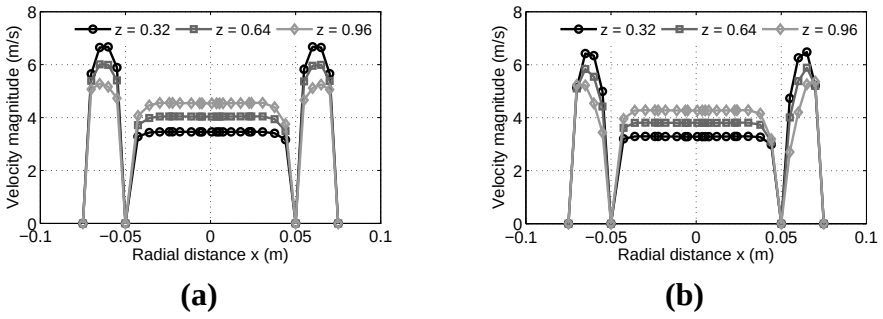

Figure 6.4: Predicted velocity magnitude profiles (m/s) in the cooling tube at three axial distances z (m) versus the radial distance x with x = 0 at the axis. (a) Realizable k-ε turbulence model and (b) laminar zone.

In order to further investigate the flow regime in the annulus, the predicted velocity magnitude profiles, using the turbulence model, in the cooling tube at three axial positions (z) are presented in Figure 6.4(a). Indeed, the velocity profile in the inner tube has the shape typical for turbulent pipe flow. However, the velocity profiles in the annulus tend to a parabolic form, which indicates laminar flow.

In a subsequent simulation the entire cooling tube has been treated as a laminar zone.

In Table 6.2 the numerical results for the single cooling tube (with boundary condition values taken from the C1 configuration experiment), treating the flow in the cooling tube either as turbulent or as laminar, are compared with the experimental values. It is observed that the predictions for both the total heat extraction rate (Q_{tube}) and for the temperature of the cooling air at the outlet ($T_{coolout}$) were closer to the experimental values when the cooling tubes were treated as laminar. This can be explained by the flow in the annulus to rather resemble laminar flow behavior and thus creating a sort of thermal resistance, limiting the total heat extraction rate of the cooling tube. In Figure 6.4(b) the velocity profiles using the laminar model are presented. It is observed that the velocity profiles in the annulus are more pronounced parabolic.

Table 6.2: Heat extraction rate (Q_{tube}) and temperature of the cooling air at the outlet ($T_{coolout}$) of a cooling tube from configuration C1.

Variable	Experiment	Turbulent CFD	Laminar CFD
Q_{tube} (kW)	12.3	18.9	14.6
$T_{coolout}$ (°C)	496	702	550

To conclude, in the furnace simulations, the flow in the cooling tubes is treated separately from the rest of the furnace and as laminar flow. The flow within the furnace itself is still treated as turbulent flow.

6.3.3 Data comparison

For comparison of the transient experimental data (due to the switching of the burners) and the steady state numerical results, averaging is required. In Figure 6.5 the furnace temperature, characterized by a thermocouple in the furnace side wall, and the preheat temperature of the combustion air in one burner are presented over a period of 5 entire cycles. These data are from the C3 burner configuration experiment.

It is noted that the transient behavior is well represented in the preheat temperature, while the furnace temperature is not showing any correlation with the cycle time. Actually, all the measurements used as boundary conditions or for validation of the simulations (wall temperatures, heat extraction rates of the cooling tubes, composition of the flue gas) show similar steady signals.

The preheat temperature of the combustion air is also used as a boundary condition for the simulations, since the regenerators are not incorporated in the simulations. Therefore, the data of the preheat temperature of an entire firing period is averaged and set as the boundary condition.

Furthermore, in order to have a similar spatial heat distribution in the simulations as in the experiments, two separate steady state simulations were performed for each con-

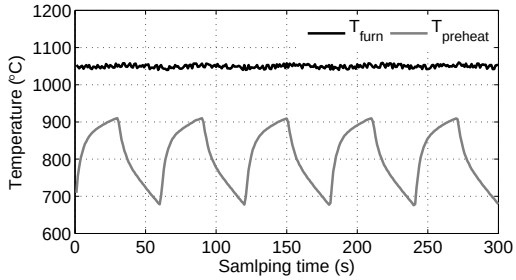

Figure 6.5: Furnace temperature (T_{furn}, °C) and preheat temperature of the combustion air ($T_{preheat}$, °C) over a period of 5 entire cycles from the C3 burner configuration experiment.

figuration. For both parts of an entire cycle a steady simulation was performed, i.e., one simulation with one set of burners firing and one simulation with the other set of burners firing was performed, see also Figure 6.2. For the final comparison of the experimental and numerical results, the results of these two simulations were averaged.

6.4 Results and Discussion

6.4.1 Validation

In Table 6.3 the main results of the experiments are compared with the numerical results for all the configurations. It is noted here that all the four configurations are simulated with the exact same set of physical models and settings, as described above.

Table 6.3: Comparison of main variables between experiments (EXP) and simulations (CFD) for the four different burner configurations (C1, C3, C4 and C5).

	C1		C3		C4		C5	
Variable	EXP	CFD	EXP	CFD	EXP	CFD	EXP	CFD
T_{furn} (°C)	1036	1121	1051	1113	1074	1142	1052	1128
Q_{cool} (kW)	99	104	97	101	98	102	90	99
Q_{loss} (kW)	145	110	122	108	141	110	150	110
T_{stack} (°C)	-	1182	-	1192	-	1216	-	1195
Q^{*}_{loss} (kW)	137	-	112	-	134	-	144	-
O_2 (%-vol) dry	3.48	3.22	3.95	4.76	3.22	3.47	3.79	3.43
O_2^{th} (%-vol) dry	3.66	3.64	5.58	5.56	4.16	4.14	4.03	4.01

The furnace temperature is overpredicted in the simulations with around 70 °C, however, these differences are considered to be acceptable.

The heat extraction by the cooling tubes (Q_{cool}) is predicted reasonably accurately. The predicted values are slightly higher for all configurations, but the values are close. The other heat losses (Q_{loss}), mainly through the walls, are underpredicted in the simulations. This is partly due to the calculation method of this value in the experiments. In the analysis of the experimental results, the heat flux through the stack is calculated assuming that the flue gas leaving the furnace via the stack is at a temperature equal to the furnace temperature. However, comparing the furnace temperature (T_{furn}) and the flue gas temperature in the stack (T_{stack}) in the simulations, the latter is consistently higher. This indicates that by taking the furnace temperature as the stack flue gas temperature, the experimental heat flux through the stack is underestimated. The values for the experimental heat losses calculated with the predicted temperature of the gas in the stack (Q^*_{loss}) show that this error explains only part of the difference.

Finally, the oxygen concentration (O_2) in the flue gas is considered. In Table 6.3 the measured and predicted values of the O_2 concentration in the flue gas from the stack are presented. Additionally, the theoretical value (O_2^{th}) calculated from the measured flows of comburants for complete combustion, both using the actual fuel (DNG) and using the simulation fuel (only containing CH_4 as a hydrocarbon, see above), are reported. In the first place, the measured values are compared with the theoretical values for the experiments. All the measured O_2 values are lower than the theoretical values. These differences are, besides the error in the measurement of the oxygen concentration itself, due to errors in the measurement of the comburant mass flows. Secondly, comparing the theoretical values for the actual fuel (DNG) and the simulation fuel, it is noted that they are very similar. Finally, comparing the predicted values in the simulations with the theoretical values for the simulation fuel, it is noted that the predicted values are systematically lower. This is due to the integration of the chemistry in the simulations. As stated before, the ISAT procedure was used for shorter computational times. Gordon et al. investigated the maximal value for the ISAT error tolerance (IET) for several mechanisms [120], concluding a maximal value of 10^{-6} for the Smooke mechanism is required. Due to too long computational times, this value was not supportable for the current mesh in combination with the current cluster.

To verify the impact of the error due to this deficiency, one case (configuration C5 with the black burners firing, see Figure 6.2) was run with IET 10^{-5}. In Figure 6.6 the main results, as presented in Table 6.3, are plotted for the simulations with the different values of the IET. It is noted that a large difference in the main results is observed between the simulations with IET 10^{-3} and 10^{-4}. In case of IET 10^{-5} the results do improve, however, relatively marginally. It is concluded here, that these simulations would improve by additional calculation with IET 10^{-5}, however, considering the time investment versus the expected improvement, this was not performed.

Additionally, in Figure 6.6, the results of the simulation with IET 10^{-4} with both

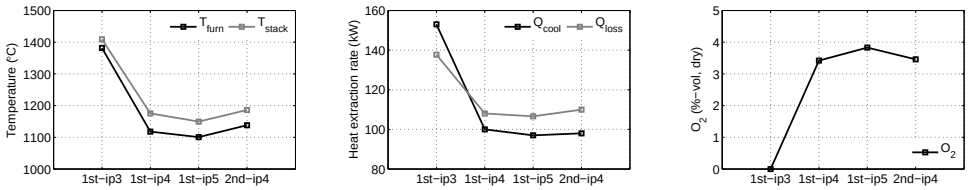

(a) **(b)** **(c)**

Figure 6.6: Main predicted results for configuration C5 parallel versus ISAT error tolerance (IET) and discretization scheme; ip4 = IET of 10^{-4}, ip5 = IET of 10^{-5}, 1st = first order discretization and 2nd = second order discretization. (a) Furnace temperature (T_{furn}, °C) and flue gas temperature in the stack (T_{stack}, °C). (b) Heat extraction rate of the cooling tubes (Q_{cool}, kW) and other heat losses (Q_{loss}, kW). (c) Oxygen concentration in the flue gas from the stack (%-vol, dry).

first order and second order discretization schemes are compared. It is noted that the differences in main results between these two simulations are marginal.

Finally, in Figure 6.7 the mass fractions of the main species in the flue gas in the stack are compared for the simulations of configuration C5 with IET 10^{-4} and 10^{-5}. It is noted that in the simulation with IET 10^{-4} lower O_2 concentrations and higher CO_2 and H_2O concentrations are predicted. In the case of IET 10^{-5} the O_2 content is slightly higher and the CO_2 and H_2O contents are lower. Thus, by decreasing the IET the oxygen concentration is tending towards the experimental and theoretical values. For both cases, the concentrations of CO and CH_4 are very low; they are in the order of 10 and 10^{-4} ppm, respectively. It can be concluded that in the simulation with the higher value of IET (10^{-4}) the combustion is complete, i.e., there is hardly any CO and CH_4 left in the flue gas. Therefore, no large errors in the total heat distribution in the furnace due to integration errors are to be expected.

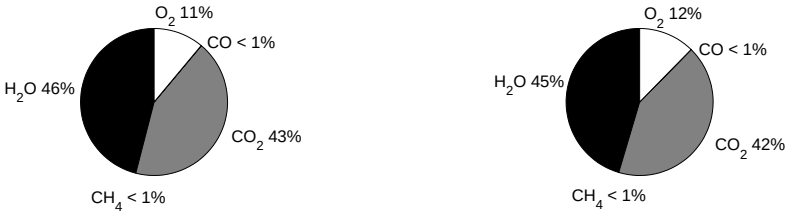

(a) IET = 10^{-4} **(b)** IET = 10^{-5}

Figure 6.7: Main species mass fractions (-) in the flue gas in the stack with burner configuration C5 for (a) IET = 10^{-4} and (b) IET = 10^{-5}.

Although no in-furnace measurements were performed for a detailed validation, the

consistency of the predictions for all the four investigated configurations confirmed the suitability of the set of physical models for a numerical investigation of this furnace.

6.4.2 Carbon monoxide emissions

In Figure 6.8 the concentrations of CO in the flue gas from the stack and from the regenerators are presented for the experiments and the simulations. For these two flue gas sampling locations, see the boxed numbers in Figure 6.1.

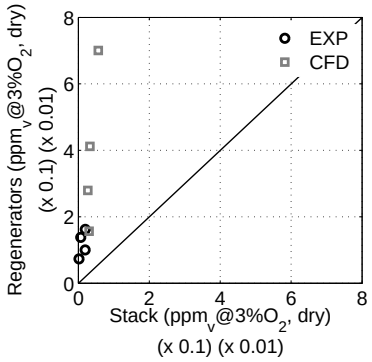

Figure 6.8: Comparison of experimental values for CO concentration (0.1 x $ppm_v@3\%O_2$, dry, EXP) and predicted values from the simulations (0.01 x $ppm_v@3\%O_2$, dry, CFD) in the flue gas from the stack and from the regenerators for all four burner configurations firing in parallel mode.

All the predicted values of the CO concentration are much higher than the measured values. This is a deficiency of the used chemistry mechanism and has also been mentioned as such by the developers of the mechanism [98]. Additionally, in the simulations the CO concentrations in the flue gas from the regenerators are taken before the regenerators (at the hot side), whereas in the experiments this CO concentration is measured after the regenerators (at the cold side). Thus, part of the excess CO observed in the numerical results would have been converted to CO_2 in the regenerators if simulated.

However, the trend in the difference between the values in the flue gas from the stack and from the regenerators is reproduced correctly; in the stack flue gas, relatively small amounts of CO are predicted, whereas in the regenerator flue gas larger amounts of CO are predicted.

The difference in the CO concentrations in the two exits is related to the path length of the mean flow to these exits. In Figure 6.9(a) the pathlines along the streamlines of the mean velocity (taken from the CFD simulations) of the gases flowing from the middle firing burner in configuration C5, to the opposing regenerating burners and to the stack are presented. The burners and the stack are indicated by the arrows. It is observed that the pathlines to the stack are longer than those to the regenerating burner. Also, it is noted

that part of the gases not immediately leaves the furnace, but is recirculated to the root of the comburants jet.

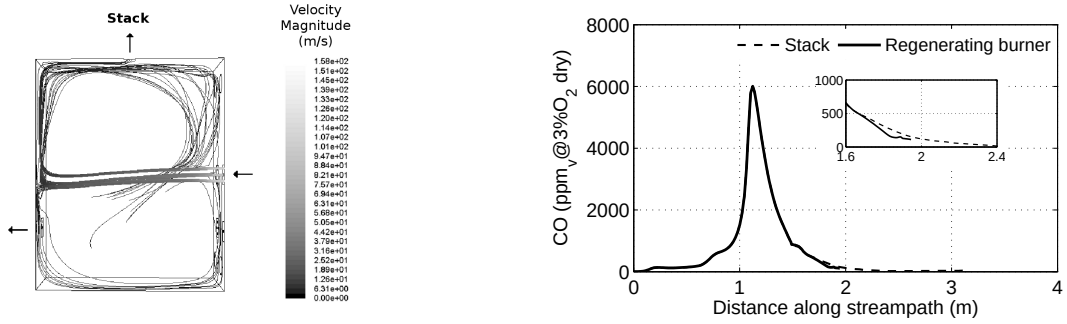

(a) **(b)**

Figure 6.9: (a) Sideview of the furnace showing the pathlines from the nozzles of a firing burner in configuration C5. Pathlines are coloured by the velocity magnitude (m/s). (b) CO concentration ($ppm_v@3\%O_2$, dry) versus distance along the paths from the firing burner to the opposing regenerating burner (solid line) and to the stack (dashed line). Results from CFD simulations.

Based on the observed pathlines from CFD, the approximate path lengths of the mean flow were calculated exploiting only straight lines and right angles. The recirculating gases were not included in this calculation since they join the jet again at its root. Furthermore, it can be assumed that the gases that immediately leave the furnace, either via a regenerating burner or via the stack, account for the largest part of the observed CO concentrations.

The path lengths between all firing burners and all regenerating burners were calculated and subsequently averaged. The same was done for the path lengths between the firing burners and the stack. The averaged path lengths from the firing burners to the regenerating burners and to the stack are approximately 2.0 m and 3.0 m, respectively. For the firing burner in Figure 6.9(a) these path lengths were converted to residence times by division with the local velocity. The residence time of the gases from this burner to the regenerating burner was 0.2 s. From the firing burner to the stack the residence time was 0.5 s. Again, these values include the direct paths only, excluding recirculation.

In Figure 6.9(b) the CO concentration along the considered paths from the firing burner to the opposing regenerating burner and to the stack are presented from the simulations. The initial 1.5 m is identical for both paths, since in both cases the gases cross the furnace width first. The peak in CO concentration, which can be regarded as the center of the combustion zone, is at approximately 1.2 m from the burner nozzles. After this point, the CO concentration decreases steadily. It is observed that the CO in the gases to the regenerating burner is not fully converted before reaching the exit point. On the other

hand, in the gases traveling towards the stack, the CO concentration further decreases (see insert with enlargement in Figure 6.9(b)) .

Thus, it is concluded that the flue gas leaving the furnace via the stack had a long enough residence time (due to its longer path length) to have most of the CO converted to CO_2.

6.4.3 Combustion air preheat temperature

In the experiments a difference in the preheat temperature of the combustion air was observed for the different burner configurations. In Figure 6.10(a) the experimental values of the preheat temperature of the combustion air are presented. It was observed that the preheat temperatures for the C4 and C5 configurations are higher than those for configurations C1 and C3.

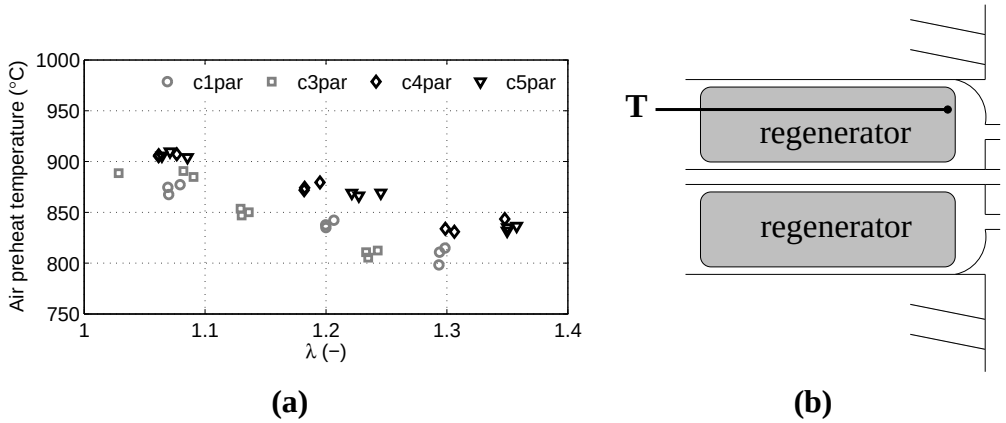

Figure 6.10: (a) Experimental values of the combustion air preheat temperatures (°C) for all configurations, parallel firing mode, all values of λ and cycle time [65]. (b) Position of thermocouple in regenerators.

In Figure 6.11 the maximum value of the normalized temperature (τ) at the hot side of the regenerator in the experiments is compared with the predicted flue gas temperature entering the regenerating burners. The normalized temperature τ is defined in Equation 6.2,

$$\tau = \frac{T}{T_{\text{ref}}} \tag{6.2}$$

where T is the temperature (K) and T_{ref} the reference temperature (273.15 K).

The numerical values are higher than the experimental values. This is due to two reasons. In the first place, the thermocouples inserted in the regenerators only penetrate until the end of the regenerators, while in the simulations the flue gas temperature is taken at the nozzle, see also Figure 6.10(b). In the second place, the measured temperatures

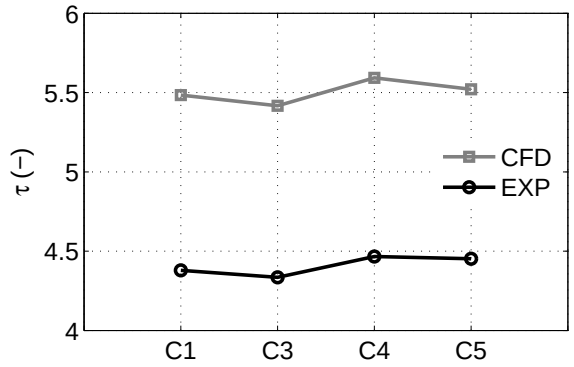

Figure 6.11: Comparison of the maximum value of τ (-) at the hot side of the regenerators in the experiments and the predicted τ (-) of the flue gas entering the regenerating burners.

Table 6.4: Measured mass percentage (%-mass) of flue gas leaving the furnace via the stack.

	C1	C3	C4	C5
Mass percentage stack (%-mass)	27.3	31.2	22.1	22.1

will be slightly lower than the actual gas temperatures due to radiative heat losses of the thermocouples. The reported experimental measurements were not corrected for these radiative losses.

However, in both the experiments and the simulations the values of τ are higher for configurations C4 and C5. This is explained by the amount of flue gas leaving the furnace via the stack. In Table 6.4 the experimental values of the mass percentage of flue gas leaving the furnace via the stack is presented for the four configurations. It is noted here that the mass percentage of flue gas to the stack is set as a boundary condition in the simulations.

It is observed that for both C1 and C3 relatively larger percentages of the flue gases leave the furnace via the stack. This is due to the fact that in these configurations the three higher burners are positioned in the upper level, whereas in C4 and C5 they are positioned in the middle level, see also Figure 6.2.

In Figure 6.12 pathlines along the streamlines of the mean velocity are presented from all grid cells of the firing burner inlets of all the configurations, colored by the local temperature. It is observed that in configuration C4 and C5, as expected, less of these pathlines leave the furnace via the stack in the roof. This is due to an additional recirculation zone above the firing burners compared to configuration C1 and C3.

It is concluded that in configurations C1 and C3, due to the firing burners positioned

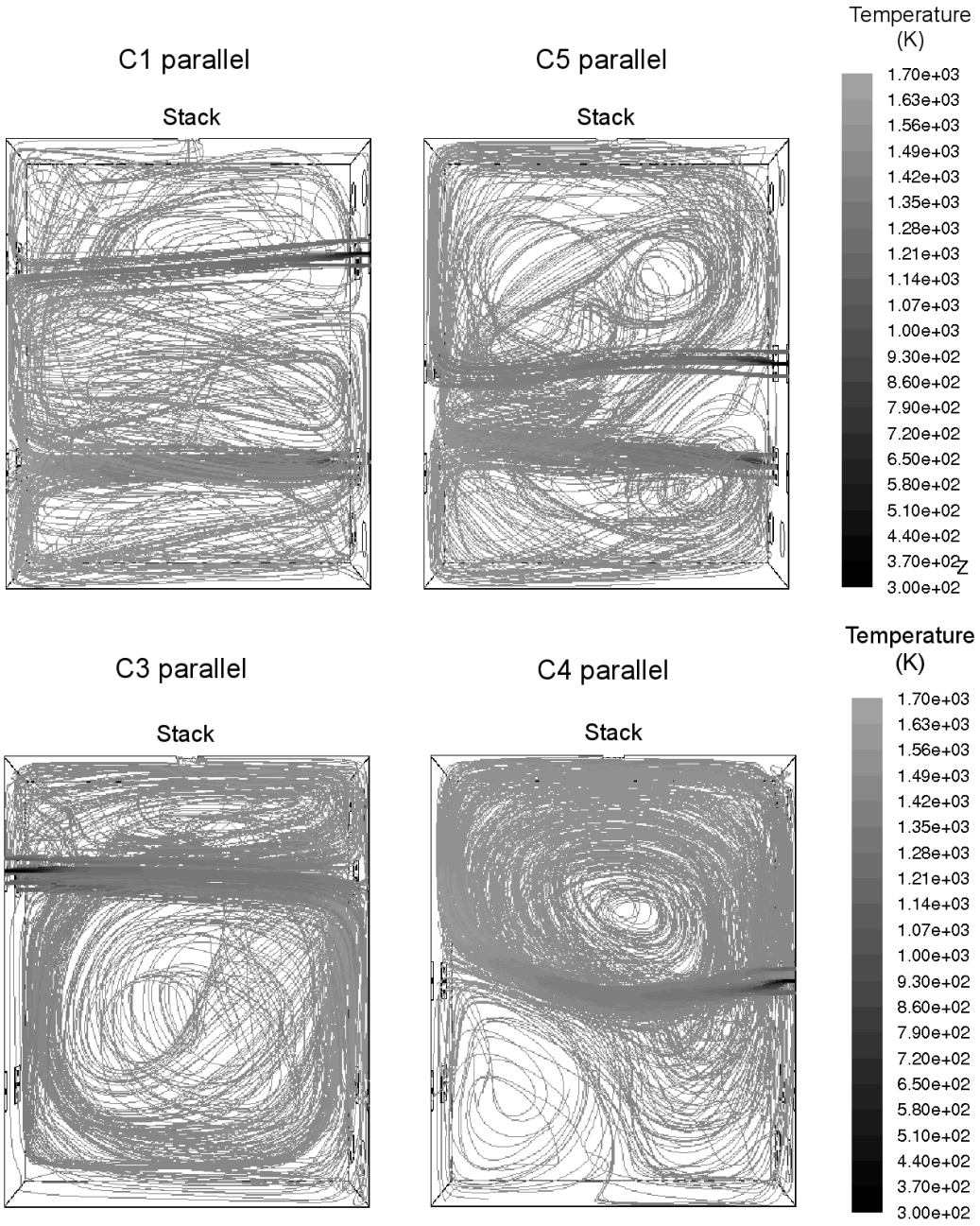

Figure 6.12: Pathlines from all grid cells of the firing burner inlets of all configurations colored by the local temperature (K) viewed towards the vertical midplane of the furnace.

closer to the stack and the absence of a recirculation zone between these firing burners and the stack, significantly more flue gas leaves the furnace via the stack and relatively less hot flue gas is available for regeneration, leading to lower preheat temperatures of the combustion air.

6.4.4 Cooling tube heat extraction

In Figure 6.13 the experimental and numerical values of the cooling tube heat extraction rate of the four configurations are compared. The predicted values are slightly higher than the experimental. However, the trend between the different cases is well captured by the simulations.

The cooling tube heat extraction is directly related to the total mass flow of cooling air to the cooling tubes. In the total mass flow of cooling air the same trend is observed as in Figure 6.13. Since the measured total cooling air mass flows are set as boundary conditions in the simulations, the trends in the total cooling tube heat extraction rates are also reproduced in the simulations.

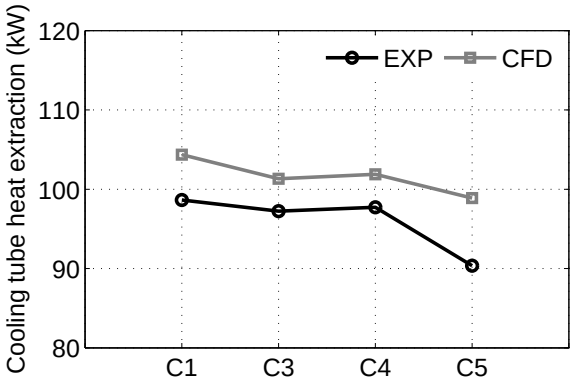

Figure 6.13: Cooling tube heat extraction rates (kW) comparison for the experiments (EXP) and simulations (CFD).

6.4.5 Temperature uniformity

In Figure 6.14 the experimental and numerical values of the temperature uniformity of the four configurations are compared. The temperature uniformity (T_u) is defined as in the following equation,

$$T_u = 1 - \sqrt{\frac{1}{N}\sum_{i=1}^{N}\left(\frac{(T_i - \bar{T})}{T}\right)^2} \tag{6.3}$$

where N is the total number of temperature measurement positions, T_i is the temperature in the ith position and $\overline{T}$ is the mean of all the temperature measurements. The value of the T_u is between 0 and 1, where the value 1 indicates a perfectly uniform furnace.

The trend in the temperature uniformities agrees well between the experiments and simulations. Especially, the observation that configurations C3 and C4 achieve higher temperature uniformities, compared to configurations C1 and C5, is reproduced. However, there is an opposing trend in the temperature uniformities of C3 versus C4 and C1 versus C5.

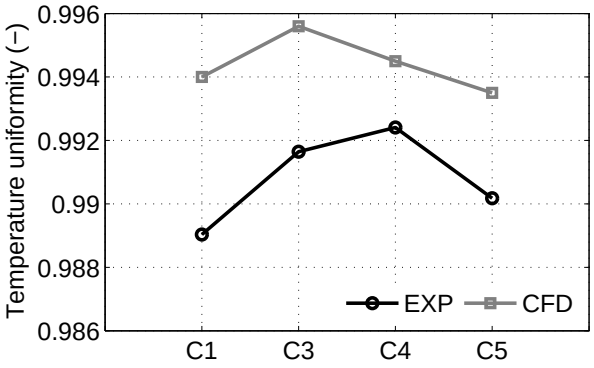

Figure 6.14: Temperature uniformity (-) comparison for experiments (EXP) and simulations (CFD).

In Figure 6.15 the predicted values for the wall temperatures are presented for burner configuration C4 and C5. The exact positions of the thermocouples are denoted in the drawings of the four side walls of the furnace.

It can be observed, comparing the thermocouples in the highest level (numbers 1, 3 and 5) with those in the middle or lower level (numbers 2, 4 and 6), that the difference in the temperature is larger for configuration C5, which resulted in a lower temperature uniformity. Actually, in configuration C4, thermocouples 1, 3 and 5 have relatively higher values. This is due to the fact that a stronger recirculation zone in this configuration results in higher temperatures in the upper zone of the furnace, see also Figure 6.12. This also explains the lower temperature uniformity in configuration C1, where the least pronounced recirculation zones can be identified. For the values of the thermocouples in the opposite wall (numbers 10 to 15) the same behavior can be observed.

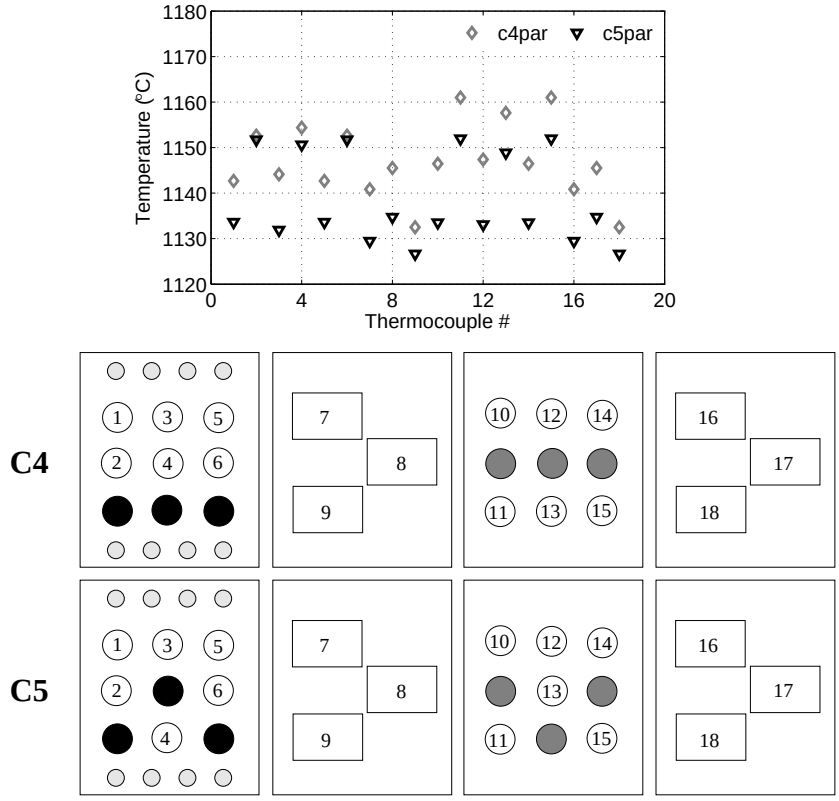

Figure 6.15: Predicted temperatures (K) for all thermocouples in burner configurations C4 and C5. The four large rectangles represent the four side walls of the furnace with the numbers indicating the positions of the thermocouples.

6.4.6 Temperature uniformity versus cooling tube heat extraction

In the experimental results, a linear correlation was observed between the cooling tube heat extraction and temperature uniformity [65]. In Figure 6.16 these values are plotted for both the experiments and the simulations. It is observed that the decreasing trend in the cooling tube heat extraction rate with increasing value of the temperature uniformity is not reproduced. Due to the choice of experiments that have been simulated it is not possible to either confirm or contradict the observations of the experimental results. In order to be able to do this, additional simulations of cases exploiting more variation in the values of the cooling tube heat extraction and the temperature uniformity are required. Due to time limitations, these additional simulations are currently not performed.

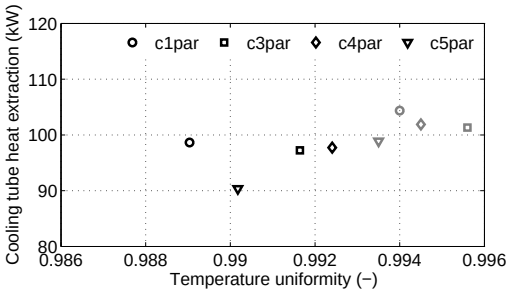

Figure 6.16: Cooling tube heat extraction rate (kW) versus temperature uniformity (-) for all burner configurations in parallel firing mode. Black symbols are the experimental values, gray symbols represent the numerical values.

6.4.7 Point of confluence

In a previous study on a comparable furnace [67] the point of confluence of the comburant jets was indicated as an important factor for the NO formation. In this study the NO emissions were similar for all configurations and operating conditions [65]. To verify whether the jets show similar merging behavior in this furnace the firing burners in the lowest level of configurations C1 and C3 are compared.

In Figure 6.17 the velocity in the (axial) z-direction, the temperature and the mixture fraction are plotted on lines at three distances from the nozzles of these burners. The distance from the burner nozzles z is normalized by the diameter of the air nozzles d (0.02 m). The fuel nozzles are positioned at x = 0.295 m and 0.75 m and are surrounded by four high momentum air nozzles, two of which are captured by the lines. The mixture fraction was calculated by applying Bilger's formula [121].

The point of confluence is defined as the point where the low-momentum jet is fully absorbed by the high momentum jet(s) [115]. The further the point of confluence from the nozzles, the more internal flue gas recirculation is present before the fuel and oxidizer jets merge and the lower the NO emissions are expected to be.

For the burner at x = 0.295 m no clear differences can be observed between configuration C3 and C1, both seem to have a point of confluence at z/d = 6. The burner at x = 0.75 m has a point of confluence at z/d = 8 in both configurations (only configuration C3 is shown in Figure 6.17, but the burner of configuration C1 showed the same value). Concluding, it is confirmed that the jets of the burners in configurations C1 and C3 show similar merging behavior, which is in agreement with the proposed explanation for the similar NO concentrations in their flue gases. Also, no distinct differences in the maximum temperatures could be identified between the two configurations. Finally, it can be expected that the middle burner (at x = 0.75 m) produces less NO than the two outer burners.

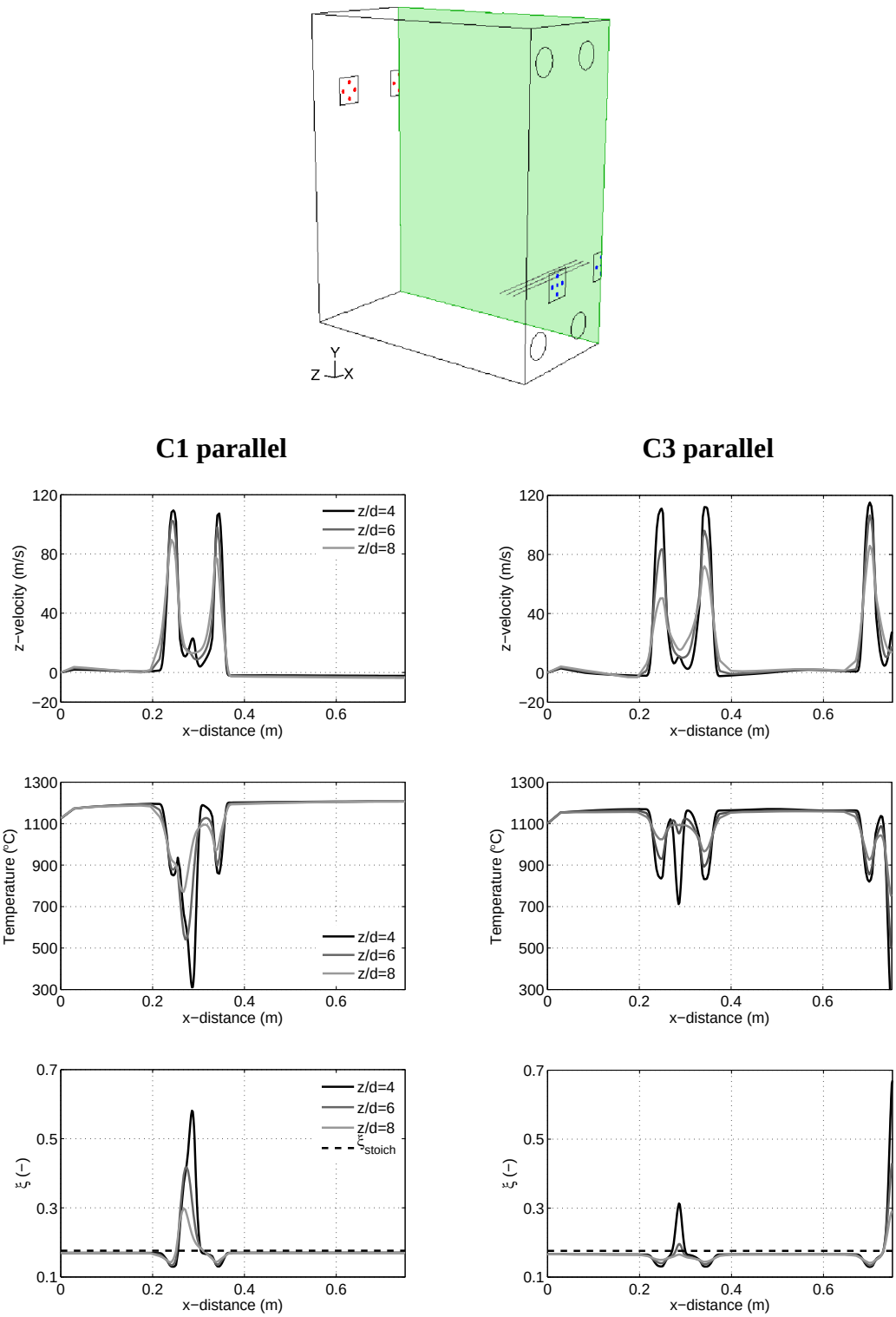

Figure 6.17: Development of the velocity in the z-direction (m/s), temperature (°C) and mixture fraction (ξ, -) for the lower burners in configurations C1 and C3 parallel. The data are plotted over the three gray lines depicted in the sketch of the numerical domain of configuration C3. The (green) shaded plane is the vertical symmetry plane.

6.5 Conclusions

A numerical study has been performed for four different burner configurations in a furnace equipped with three pairs of flameless combustion burners. A carefully selected set of physical models proved to be adequate to reproduce the main results observed in the furnace experiments. The simulations have been validated against the main results of the furnace experiments and by consistently capturing the trends in these results for the different burner configurations. Moreover, it was found that due to relatively low Reynolds numbers in the cooling air flow in the annulus of the cooling tubes, predictions of the heat extraction rates of these cooling tubes were improved by treating the flow in the cooling tubes as laminar. Furthermore, the applied error tolerance of the ISAT procedure was shown to be insufficient for accurate species concentration predictions, however, based on analysis of the main species concentrations in the flue gas, this inaccuracy did not influence the overall predictions.

The most important experimental results have been investigated using the simulations. In the first place, a longer path length from the firing burners to the stack, compared to the path length to the regenerating burners, explained the lower CO emissions in the flue gas in the stack. Secondly, it was found that a recirculation zone between the upper firing burners and the stack in configurations C4 and C5 resulted in a smaller fraction of the flue gases leaving the furnace via the stack compared to the other configurations. Thus, a larger fraction left the furnace via the regenerating burners and this resulted in higher preheat temperatures of the combustion air. Furthermore, the total cooling tube heat extraction was directly related to the total amount of cooling air. In the fourth place, more pronounced recirculation zones in configurations C3 and C4 led to higher temperature uniformities in the furnace. Finally, it was confirmed that the jets of the burners in configurations C1 and C3 showed similar merging behavior, leading to similar NO emissions, as have indeed been observed in the experiments.

It can be concluded that by the numerical study more insight is attained regarding the effects of burner positioning in a multi-burner flameless combustion furnace. In the future, the simulations can be improved by further decreasing the error tolerance of the ISAT procedure. Also, in order to verify the observation in the experiments of a decreasing cooling tube heat extraction with increasing temperature uniformity, additional simulations are required.

Chapter 7

Gas turbine combustor firing LCV gases

A prototype flameless combustion gas turbine combustor has been investigated experimentally and numerically. The combustor was operated with various Low Calorific Value (LCV) gases. At the outlet main component and emission measurements (CO and NO) have been performed. The influence of several parameters (i.e. fuel composition, outlet temperature and nozzle diameter) on the emissions have been investigated. Ultra-low emissions (single-digit) have been achieved. Moreover, axial temperature profiles in the combustion chamber have been measured with a suction pyrometer.

The combustor has been simulated with a commercial CFD code (Fluent 6.3) to gain insight in the combustion characteristics. Using the Eddy Dissipation Concept (EDC) model for turbulence-chemistry interaction in combination with the Reynolds Stress model for turbulence and two different chemistry mechanisms, the measured temperature profiles have been reasonably well reproduced. In post-processing mode different NO formation paths have been studied.

The contents of this chapter have been published in *Combustion Science and Technology*, Experimental and numerical investigation of a flox combustor firing low calorific value gases, B. Danon, W. de Jong and D.J.E.M. Roekaerts, 2010;182(9):1261-1278.

7.1 Introduction

Nowadays, two issues are gaining attention worldwide: the search for a substitute for fossil fuels and curbing emissions from combustion applications. Biomass has been identified as such a substitute. To be able to use this solid phase energy resource in existing (combustion) applications, gasification is an obvious choice. Biomass gasification using air produces Low Calorific Value (LCV) product gases, containing large amounts of H_2 and CO. Simultaneously, novel combustion techniques have been developed to curb the emissions of CO, CO_2 and NO. Flameless combustion, also mentioned in the literature as flameless oxidation (FLOX, [8]), MILD combustion [21] or HiTAC [5], is such a low emission combustion technique.

The flameless combustion technique is based on high momentum injection of the fuel and/or oxidizer. Furthermore, it has been reported that low calorific value gases mix more slowly under flameless conditions, as compared to natural gas, also resulting in zones of higher axial strain and vorticity [122]. In this way large amounts of flue gas are internally recirculated into the flame zone. The mixing of the flue gas with the comburants before combustion results in an extended reaction zone with lower oxygen concentrations and lower peak temperatures [5]. This lowers the NO formation via the thermal pathway.

In this chapter the results are reported of a research project combining the developments of using LCV gas and flameless combustion. A prototype flameless gas turbine combustor was fired with LCV gases (representing typical biomass gasification gases) under ultra-low emission combustion. In the combustor the fuel and air are introduced (partially) premixed, a design that is currently widely applied in industry. This [123] and similar [124] combustors have also been tested at high pressures, however this study is at atmospheric pressure only. The results of the experiments and the CFD simulations will be compared with similar research reported in the literature [123, 124, 125, 126, 127, 128, 129]. The effect of the combustor outlet temperature, the fuel gas composition and the inlet velocity on the CO and NO emissions have been analyzed experimentally. As a second step, measured axial temperature profiles have been used for the validation of the CFD simulations. The validated simulations gave detailed insight (e.g. flame shape and recirculation zones) in the physical and physicochemical phenomena of flameless combustion applied to such low calorific value gases and can lead to improved design of combustors for different applications.

7.2 Experimental setup

In Figure 7.1 schematic representations of (a) the experimental setup and (b) the combustion chamber are presented.

For the experiments a catalytic Auto Thermal Reforming (ATR) unit was used for the

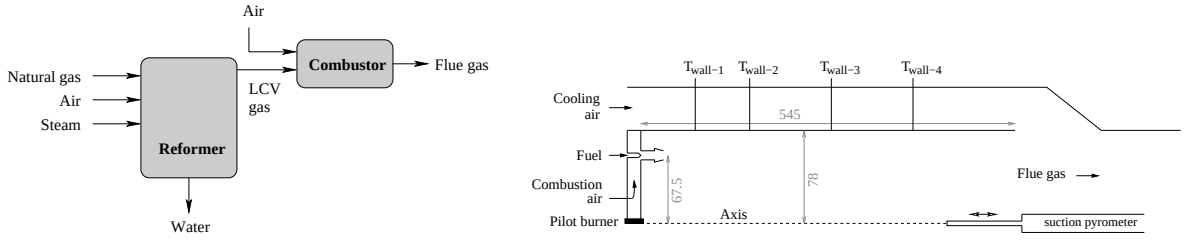

Figure 7.1: Schematic representation of (a) experimental setup (b) combustion chamber (dimensions are in mm).

production of the LCV gases. In this unit, desulphurized Dutch natural gas (containing about 14 %-vol nitrogen) is reformed (with steam and air) to a mixture of CH_4, CO, CO_2, N_2 and H_2 via catalytic partial oxidation and the watergas shift reaction. The gas is dried by cooling it down to 25 °C. The composition of the LCV gas is varied by adjusting the initial ratios of natural gas, steam and air. Different mixing ratios led to differences in the heat of combustion of the LCV gases.

In Table 7.1 the dry gas composition of some of the produced fuels is presented. The fuel with a lower heat of combustion value of 6.5 MJ/m_n^3 was used as the standard fuel.

Table 7.1: Fuel gas composition and lower heat of combustion values for some of the studied fuels.

H_{comb} MJ/m_n^3	CH_4 %-vol dry	CO %-vol dry	CO_2 %-vol dry	H_2 %-vol dry	N_2 %-vol dry
5.9	1.67	11.65	6.28	35.62	44.78
6.1	2.82	10.82	6.64	34.92	44.81
6.5	4.23	9.54	7.22	34.90	44.11
7.0	7.15	7.90	7.55	31.93	45.47
7.7	10.55	6.81	7.68	28.34	46.62
8.6	15.47	5.20	7.38	22.63	49.32

The LCV gas was subsequently burned in a prototype flameless gas turbine combustor manufactured by WS Wärmeprozesstechnik, see also [130]. The combustor consists of 12 fuel nozzles that inject the fuel in 12 mixing ducts, as can be seen in Figure 7.2. The nozzles are positioned in a circle with a diameter of 125 mm.

The air is introduced centrally and mixes with the fuel in the mixing ducts. Finally, the mixed fuel and air flow through the main inlet nozzles into the combustion chamber. Two different sizes of main inlet nozzles were used during the experiments in order to vary the inlet velocity (v_{in}); the inner diameter (d_n) of these main inlet nozzles used in an experiment was either 11 mm or 6.75 mm.

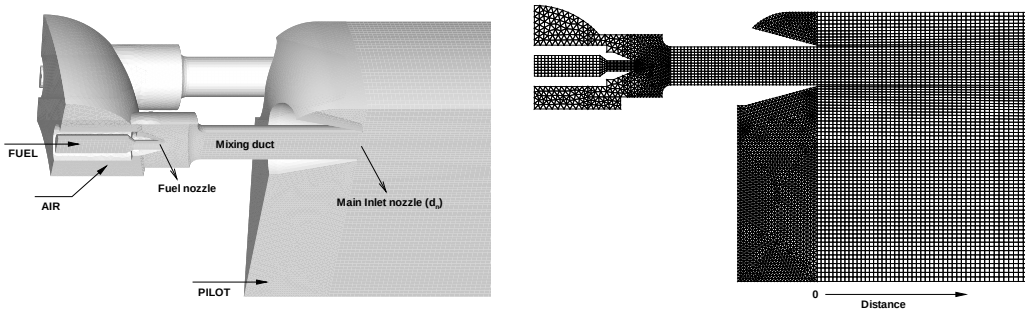

(a) **(b)**

Figure 7.2: (a) Detailed view of the nozzles and the mixing duct, a sector of 30 degrees containing one nozzle is depicted. (b) Surface mesh of the planes with symmetry boundary conditions in the region close to the nozzles.

The combustion chamber is cylindrical, with an inner diameter of 156 mm. On two sides of the combustion chamber there is a flat window for optical access. The casing is double, allowing cooling air to flow through the annulus. On four positions (between 75 and 400 mm from the main nozzle tip) the temperature of the inner casing was measured. These measured temperatures were used as boundary conditions in the CFD simulations.

The combustor is operated at atmospheric pressure. The thermal power input (P_{th}) was chosen to be either 67 kW_{th} or 100 kW_{th}. For the 67 kW_{th} cases the outlet temperature (T_{out}) was varied in a few steps between 950 °C and 1050 °C and could be controlled by changing the amount of cooling air in the combustion chamber casing. When not mentioned otherwise, the standard LCV gas is used in the experiments, which is the gas with heat of combustion (H_{comb}) of 6.5 MJ/m^3_n. Furthermore, for the 67 kW_{th} cases, different LCV gases with different values of H_{comb} were tested. In Table 7.2 an overview is presented with the different cases.

Table 7.2: Investigated cases.

Case	P_{th} (kW_{th})	d_n (mm)	H_{comb} (MJ/m^3_n)	T_{out} (°C)
67n11	67	11	6–8.5	950–1050
67n675	67	6.75	6–8.5	950–1050
100n11	100	11	6.5	1050
100n675	100	6.75	6.5	1050

The excess air ratio (λ) was kept constant at approximately 1.5 for all experiments (corresponding to an equivalence ratio ϕ = 0.67), with only a minor deviation of at most 10%. Furthermore, the combustion air (T_a) was preheated to 300 °C, representing the air temperature after the compressor in a gas turbine. During operation the pilot burner,

located on the central axis (see Figure 7.1(b) and 7.2(a)), was switched off, though a small ambient air flow (about 2 m_n^3/h) is maintained on the pilot burner to protect the equipment. The diameter of the pilot nozzle is 25 mm, leading to an injection velocity of 1.2 m/s.

Various on-line measurements were performed during the experiments. The NO, CO and CO_2 concentrations were measured using an NDIR analyzer, while the oxygen concentration was determined paramagnetically. Axial profiles of the gas temperature were measured by the downstream insertion of a suction pyrometer probe. In this device a type S thermocouple was mounted. The pyrometer was traversed over the central axis of the combustion chamber. Note that the axis is not in the main combustion reaction zone, since the nozzles are positioned on a circle around the central axis.

For four different cases the axial temperature profiles were measured and the associated simulations were performed. These are with thermal power input P_{th} of 67 and 100 kW_{th} and main inlet nozzle diameter of 11 and 6.75 mm. In all these cases the outlet temperature was 1050 °C.

It is known that the insertion of a suction pyrometer influences the flow field and thus alters the combustor behaviour. To verify that this influence is acceptable, an additional simulation, with the cold suction pyrometer fully inserted, was performed. In Figure 7.3 the axial temperature profile of this additional simulation is compared with the simulation without the suction pyrometer for the 100n11 case. It was concluded that the disturbance due to the insertion of the suction pyrometer is acceptable.

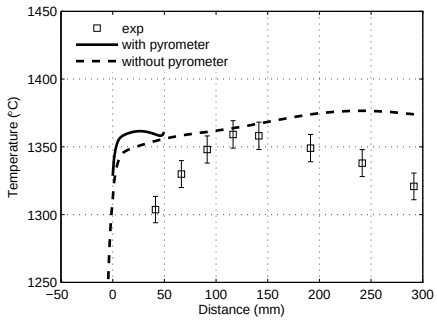

Figure 7.3: Axial temperature profiles of the simulations with and without the insertion of the suction pyrometer for the 100n11 case.

Also, gas temperatures measured with a suction pyrometer are known to be lower than the actual gas temperatures due to radiation losses of the pyrometer. To estimate this difference, the efficiency of the suction pyrometer has been determined with the dynamic response method [131]. The efficiency was calculated to be 0.88 for the current setup and the temperatures were corrected with 10–15 K. The errorbars indicate the error of the mounted type S thermocouple.

7.3 Numerical setup

A three dimensional mesh was generated using Gambit 2.3. The mesh contains approximately 500.000 hexahedral and tetrahedral cells. Exploiting the axial symmetry of the combustor, to reduce the computational time, only one twelfth of the combustor is meshed. The two planes with symmetry boundary conditions are slicing two nozzles through their middle, see Figure 7.2(b).

The simulations were performed with Fluent 6.3.26. The implicit pressure based steady solver was used with Green-Gauss node based interpolation. For turbulence closure the Reynolds Stress model (RSM) and the realizable k-ε model (RKE) were used. The realizable k-ε model is shown to give improved results, compared to the standard k-ε model, for the prediction of round jets, as is the case in this combustor geometry [97]. For the combustion of the LCV gas two different kinetic mechanisms were applied and compared; a combination of the standard Fluent kinetic mechanisms for methane and hydrogen (SFM, 7 species, 4 reactions) and a detailed mechanism (SMO, 16 species, 46 reactions, [98]). The SFM mechanism is the combination of the methane-air-two-step [132] and hydrogen-air-one-step [133] mechanisms. The chemistry-turbulence interaction is taken into account by using the Eddy Dissipation Concept model [99]. The EDC model was found earlier to give good predictions for flameless combustion [102]. Radiative heat transfer is accounted for using the Discrete Ordinates model and the cell-based Weighted Sum of Gray Gases model for the absorption coefficient of the gas mixture [134]. The emissivity of the steel casing was set to 0.8.

The density of the mixture is calculated by the multicomponent ideal gas law. The molecular viscosity and thermal conductivity are taken constant, after a check that calculating their values with kinetic theory showed no significant change in the results. The mass diffusivity is calculated with the constant dilute approximation. Finally, the heat capacities are determined per species with a temperature dependent piece-wise polynomial, and for the mixture with the mixing law.

As mentioned before, the measured wall temperatures of the inner casing were used as boundary conditions for the CFD simulations. These temperatures were introduced in the simulations as a second order polynomial fit of the axial distance. In Figure 7.4 the measured temperatures and the polynomials are presented for all cases. It is noted that in the 100 kW_{th} cases lower temperatures are observed further along the axis. This is due to the increased amount of cooling air.

The NO formation is studied in post-processing mode. Calculations have been made for thermal (including N_2O pathway) and prompt NO for all cases, using standard Fluent models [112]. The reburning of NO was not included.

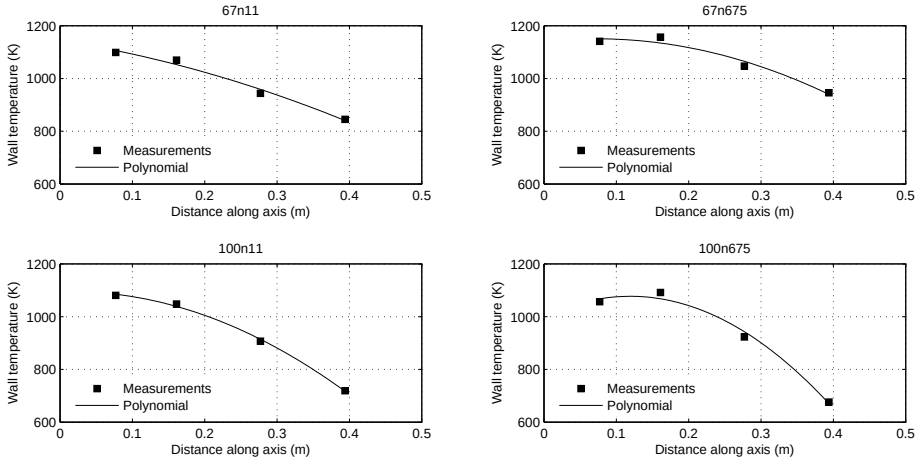

Figure 7.4: Measured wall temperatures (K) and polynomials for boundary conditions.

7.4 Results and Discussion

7.4.1 Experiments

In Figure 7.5 the flame shapes are presented for the combustor firing at 67 kW_{th} and the outlet temperature kept at 1050 °C for the two different inlet velocities. Both pictures were taken with the same camera adjustments. The white arrows denote the flow direction from the main inlet nozzles. The flame was stable and characterized by low noise levels (also reported for similar fuels [135]). A clear difference in flame colour can be observed between the two pictures. In the case of higher inlet velocities (b) the flame becomes less bluish and more transparent. This is a trend that is expected in the line of flameless combustion [8]. However, the flame is not fully invisible, thus the term flameless would be inappropriate here; the flame is tending towards the flameless regime.

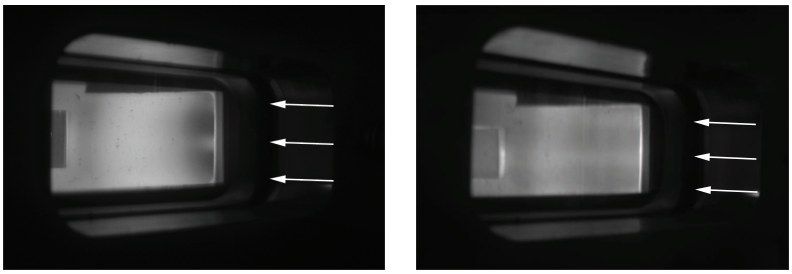

(a) **(b)**

Figure 7.5: Flame shapes at different inlet velocity; (a) v_{in} = 51 m/s and (b) v_{in} = 135 m/s. White arrows indicate the flow direction. T_a=300°C, λ=1.5, p=1atm, P_{th}=67kW_{th}, T_{out}=1050°C, H_{comb}=6.5MJ/m_n^3.

In Figure 7.6 the measured NO and CO concentrations are plotted versus the outlet temperature. Unfortunately, due to a measurement error in the low velocity case, Figure 7.6(a), CO measurements at the two highest outlet temperatures were unreliable. At these temperatures only the NO measurements are included in the Figure. The current single-digit emission results are compared with results from similar research reported in the literature and were found to be comparable [123, 125, 126, 127] or even lower [124, 128, 129]. Thus, it is plausible to characterize this system as ultra-low emission combustion.

The NO and CO concentrations show opposite trends. The NO concentration increases with higher outlet temperatures. This is due to increased NO formation via the thermal (or Zel'dovich) mechanism. In contrast, higher outlet temperatures lead to faster CO to CO_2 reactions, causing the CO concentration to drop.

In the case of higher inlet velocities, Figure 7.6(b), the observed increase of NO with increasing outlet temperature is enormously decreased. This reduction of a characteristic of thermal NO formation is attributed to the flame tending more towards flameless combustion, i.e. broadening of the reaction zone and lowering of the peak temperatures, causing reduction of the thermal NO formation. This trend has been reported in the literature before [124].

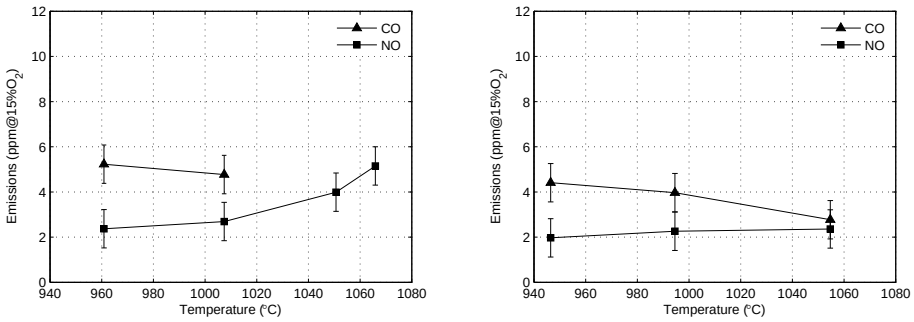

(a) **(b)**

Figure 7.6: Emissions versus outlet temperature; (a) v_{in} = 51 m/s and (b) v_{in} = 135 m/s. T_a=300°C, λ=1.5, p=1atm, P_{th}=67kW$_{th}$, H_{comb}=6.5MJ/m^3_n.

Next, the effect of changing the composition of the fuel (and thus its heat of combustion) on the CO and NO emissions was investigated. In Table 7.1 the composition of some different fuels are overviewed (characterized by their lower heat of combustion, H_{comb}).

In Figure 7.7 the results for the emission measurements are presented. It is generally noted that the production of both CO and NO increase with increasing H_{comb}. The increase of CO is explained by the higher concentration of C-containing comburants (methane and CO) in the fuels (see Table 7.1, from approximately 10%-vol to 20%-vol).

The increase of NO is mainly due to thermal NO formation, since no prompt NO is expected under these fuel lean conditions. Two important influencing parameters con-

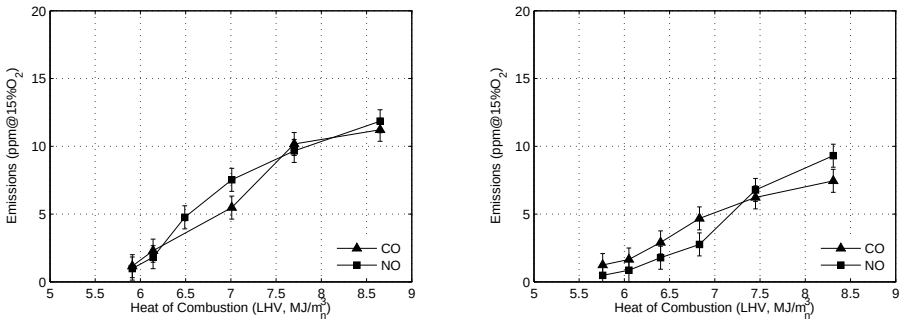

Figure 7.7: Emissions versus fuel composition; (a) lower v_{in} and (b) higher v_{in}. T_a=300°C, λ=1.5, p=1atm, P_{th}=67kW$_{\text{th}}$, T_{out}=1050°C.

cerning thermal NO formation are the oxygen availability and the adiabatic equilibrium temperature, see e.g. Landman et al. [136]. In Figure 7.8 (a) the adiabatic flame temperature (T_{adiab}) for the used fuel-air mixtures are presented (calculated using Chemkin 4.1.1 using the GRIMECH 3.0 mechanism). In Figure 7.8 (b) the oxygen fractions in these mixtures are presented. Both the T_{adiab} and oxygen fraction show an increase for the fuels with increasing H_{comb} values. However, the fuels with a heat of combustion value, above 8 MJ/m^3_n, show an opposite trend; the T_{adiab} is decreasing while the oxygen fraction is comparatively strongly increasing. This is due to the higher fraction of C-containing species in these fuels, which also results in higher specific heat of the flue gas. These trends also have an opposite effect on the thermal NO formation. Referring to Figure 7.7, it is observed that these opposite effects on the thermal NO formation result in a continuation of the increasing trend in the emissions production.

Comparing the lower and higher inlet velocities, both the CO and NO emissions decrease with higher inlet velocities, regardless of the heat of combustion. This is attributed to the flames tending more towards the flameless regime. For NO, the lower peak temperatures curb the thermal NO formation. In the case of CO, it is assumed that the improved mixing of the flameless regime enhances the CO reacting towards CO_2.

7.4.2 CFD simulations

In order to optimally simulate the experiments, different turbulence models and chemistry mechanisms were evaluated.

For turbulence the realizable k-ε (RKE) and Reynolds Stress (RSM) models were investigated. Both models were combined with the Smooke mechanism and the turbulence chemistry interaction was incorporated using the Eddy Dissipation Concept model. These first simulations were performed using the 100n11 case, see Table 7.2.

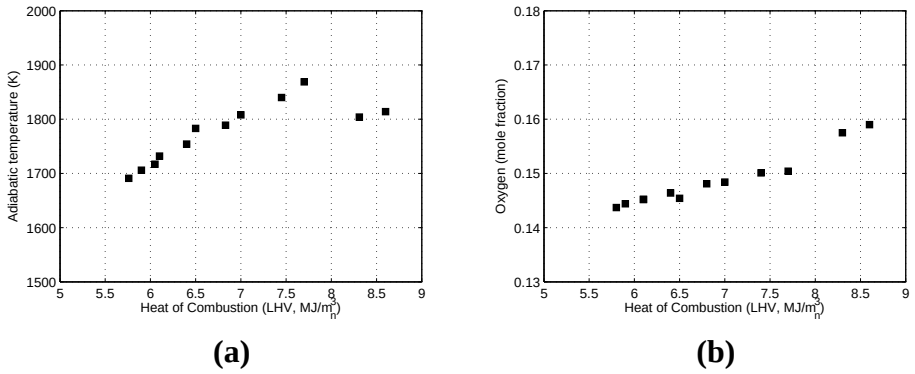

Figure 7.8: Adiabatic equilibrium temperatures (a) and oxygen fractions (b) in the fuel-air mixtures.

Flow and temperature fields

In Figure 7.9 the O_2 mole fraction is displayed for the incoming fuel and air flows. In this Figure the extent of mixing can be seen. It is observed that towards the end of the mixing duct a non-uniform O_2 concentration profile is present. Thus, the fuel and air mixture enters the combustion chamber partially mixed.

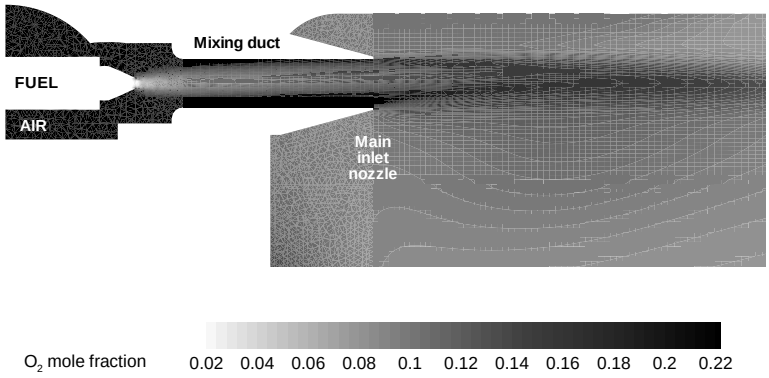

Figure 7.9: O_2 mole fraction (-) in the mixing duct and main inlet nozzles for the 100n11 case.

In Figure 7.10 the experimental and computational results for the axial profile of the mean temperature are presented. The measurement points are at the central axis of the combustor, not in the main combustion zone, with zero corresponding to the height of the tip of the inlet nozzle, see also Figure 7.2(b). The error bars consist of the measurement error of the thermocouple. All measured temperatures were corrected for the error due to radiation and conduction losses of the suction pyrometer [131]. The pilot nozzle injecting

ambient air is located at axial distance -50 mm, explaining the lower temperature at low axial distance.

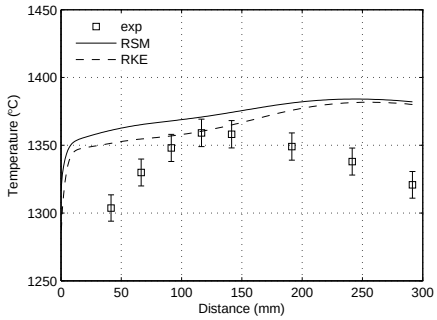

Figure 7.10: Axial temperature profiles. Experiments versus simulations with Smooke chemistry mechanism selecting different turbulence models (RSM = Reynolds Stress model, RKE = realizable k-ε model).

On the basis of the results shown in Figure 7.10 it is not possible to conclude that either RSM or RKE performs better. Both calculations seem to miss some essential features of the experimental profile. Because of the known capability of the RSM to describe flows with recirculation zones well [137] and since the computational time of the simulation was not increased significantly by the change from realizable k-ε to Reynolds Stress it was decided to use the latter model.

In Figure 7.11 the measured and simulated axial temperature profiles are presented for all four cases. Two different chemistry mechanisms are used; the Smooke mechanism (SMO) and the combination of the standard available Fluent mechanisms (SFM). This latter mechanism is the combination of the in Fluent incorporated methane-air-2-step and hydrogen-air mechanisms [76].

Some essential trends seen in the measurements are reproduced by the calculations. Comparing the upper two figures with the lower two it can be seen that higher thermal input causes higher temperatures. Contrarily, comparing the figures on the left hand side with those at the right hand side, it can be seen that higher inlet velocities reduce the temperatures. In the case of lower inlet velocity the shape of the simulated temperature profiles is somewhat better captured than in the case of higher inlet velocity.

The SFM simulations tend to be closer to the measurements, especially between x = 50 mm and x = 150 mm. This is related to higher internal flue gas circulation, see Figure 7.12, in which the axial z-velocity is plotted on the axis. The more negative this velocity is, the stronger the recirculation zone is. This higher recirculation is due to much higher inlet velocities of the comburants, as can be seen in Table 7.3, where the experimental and simulated inlet velocities of the fuel-air mixtures are presented. The experimental values are calculated from the measured flows and temperatures of fuel and air.

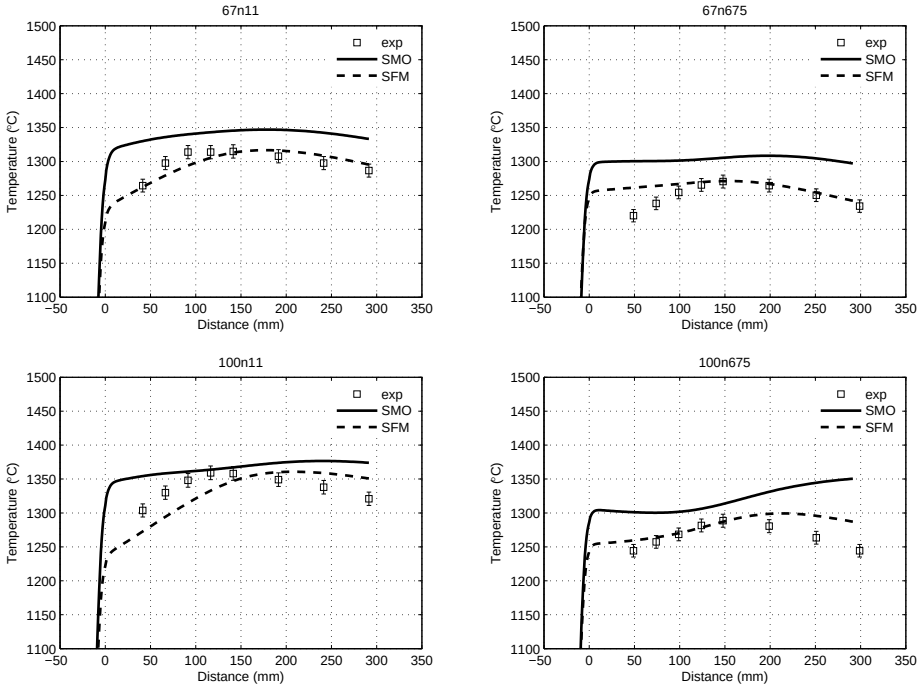

Figure 7.11: Axial temperature profiles using Reynolds Stress model selecting different chemistry mechanisms (SMO = Smooke mechanism, SFM = Standard Fluent Mechanisms).

As expected, for increasing thermal power input and for decreasing inlet nozzle diameter the inlet velocity rises. This trend is observed for experiments as well as for the simulations. Small differences in inlet velocities found in the simulations using the SMO mechanism and the experiments can be attributed to small differences between simulation and experiment in the thermal wall boundary conditions in the nozzle.

However, the inlet velocities in the SFM simulations are much higher than the experimental values. In the following analysis an explanation was found for these high velocities.

In Figure 7.13 the temperature contours are presented for the 100n11 case for both mechanisms. In the SMO simulation (on the righthand side) it is observed that a broad flame front is present in the combustion chamber, as could be expected looking at Figure 7.5. On the other hand, the SFM simulations, with their temperature profiles closer to the measurements, predict reactions to take place within the mixing duct of the nozzles (flashback). However, flashback in these experiments is very unlikely, since the turbulent flame speed of the mixtures is much smaller than the inlet velocities calculated from the experiments. For this reason the SFM simulations must be considered inaccurate.

However, it was observed that due to the flashback the internal flue gas recirculation increased and thus the shape of the axial temperature profiles were improved. This raised

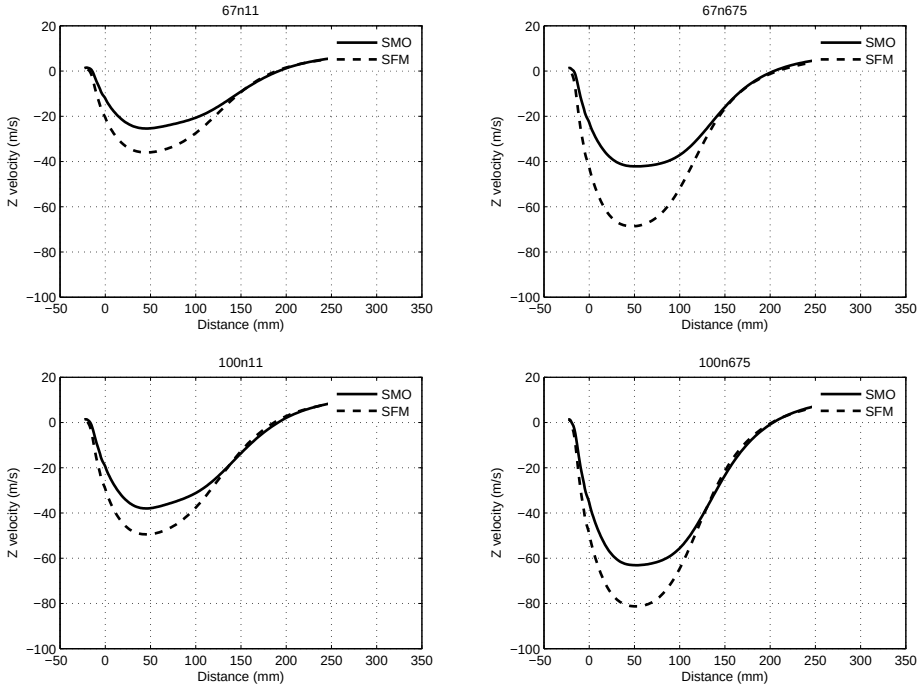

Figure 7.12: Axial z-velocity profiles using Reynolds Stress model selecting different chemistry mechanisms (SMO = Smooke mechanism, SFM = Standard Fluent Mechanisms).

the question whether there are model changes that could improve the prediction of the recirculation. It is known that the predicted entrainment by jets and consequently the strengths of recirculation zones in the neighborhood of jets depends on the values of some of the model constants. In this respect, it is known that a change in the value of the model constant $C_{\varepsilon 1}$ can improve the prediction of the spreading rate of round jets [75]. Therefore, additional simulations were performed with the $C_{\varepsilon 1}$ of the Reynolds Stress model increased from its standard value of 1.44 to 1.6, a recommended value found in [138].

In Figure 7.14 results are presented for the SMO mechanism in the 100n11 case for $C_{\varepsilon 1}$ = 1.44 and for $C_{\varepsilon 1}$ = 1.6. The experimental values of the temperature are between the the predicted temperature profiles of the simulations with and without the adjusted value of $C_{\varepsilon 1}$. The *z*-velocity profiles show, as expected, that an increase in $C_{\varepsilon 1}$ causes the internal recirculation to increase. It is concluded that the discrepancies between the measured and simulated temperatures are within the range of uncertainty in what are optimal values of model constants in the turbulence model. Fine tuning the turbulence model was out of the scope of this research, and the standard RSM was retained.

Next, the shape and position of the recirculation areas in the combustion chamber are presented in Figure 7.15 for the SMO simulations. The streamlines show that two recircu-

Table 7.3: Experimental and simulated values of mixture inlet velocities v_{in} (m/s) for different cases.

		67n11	67n675	100n11	100n675
v_{in} *experiments*	*m/s*	*51*	*135*	*76*	*201*
v_{in} SMO	m/s	51	140	75	208
v_{in} SFM	m/s	120	329	160	335

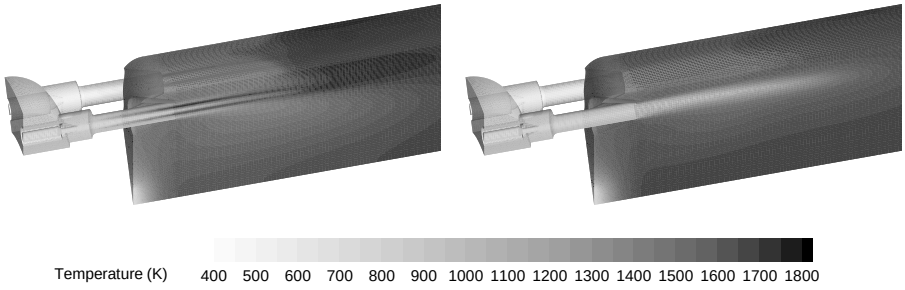

Figure 7.13: Temperature (K) for standard Fluent mechanisms (left) and Smooke mechanism (right).

lation areas are present; the main zone under the nozzle (in the middle of the combustion chamber) and a second (minor) area between the wall and the nozzles. This has been observed before in a similar flameless burner [124]. In the cases with lower inlet velocity the minor recirculation area is not present. However, in the 100n675 case this minor recirculation zone is similar to such zones observed in the literature.

In order to get a good insight in the predicted recirculation at different axial positions, radial profiles of the *z*-velocity are plotted in Figure 7.16. In this figure, as in Figure 7.15, for the 100n11 case no recirculation zone is observed between the nozzle and the wall, where in the 100n675 case this zone can be observed. In Figure 7(a) in [129] there is also a small recirculation zone observed between the nozzle and wall. This was found by Duwig et al. using LES simulations and here with RANS. The additional recirculation zone explains the observed lower emissions in these cases. Since the total recirculation is increased, more inert flue gases are mixed into the flame zone, thus lowering the peak temperatures and the thermal NO production there. A second advantage of the additional recirculation zone is the improved mixing in the combustion chamber, thus increasing the CO to CO_2 conversion. In Figure 7.16 it is observed that the minor recirculation zone pushes the jet from the wall. In both cases the main internal recirculation zone looks similar.

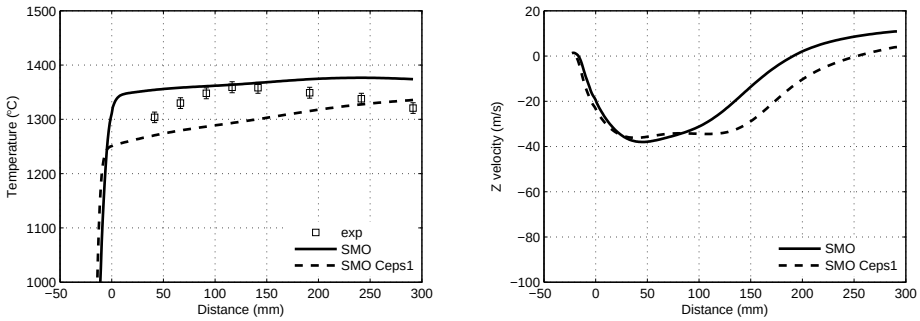

(a) **(b)**

Figure 7.14: Axial profiles for (a) temperature and (b) z-velocity for 100n11 case, using Smooke mechanism; with $C_{\varepsilon 1}$ 1.44 (SMO) and 1.6 (SMO Ceps1).

Emissions

In Table 7.4 the predicted values of the main components in the flue gas are compared with the experimental values after data reconciliation.

Table 7.4: Outlet species concentrations for experiments (italic) and simulations.

		67n11	67n675	100n11	100n675
O_2 calculated	*%-vol (dry)*	*6.9*	*7.5*	*6.6*	*7.1*
O_2 SMO	%-vol (dry)	7.1	7.6	6.9	7.6
CO_2 calculated	*%-vol (dry)*	*7.9*	*7.4*	*8.0*	*7.7*
CO_2 SMO	%-vol (dry)	7.7	7.3	7.8	7.3
CO measured	*ppm@15%O_2*	*1*	*1*	*4*	*2*
CO SMO	ppm@15%O_2	25	35	78	95
NO measured	*ppm@15%O_2*	*5*	*none*	*5*	*none*
NO SMO	ppm@15%O_2	5	5	8	7

The oxygen and carbon dioxide predictions in the flue gas agree reasonably well with the simulations. For CO there are large discrepancies, the simulated CO concentrations are much higher than the measured. It remains to be investigated whether these discrepancies are due to the chemical mechanism used or due to the model used for the turbulence chemistry interaction (EDC). Results from the NO post-processing calculations agree well with measured values, all values are single-digit. In post-processing mode thermal, prompt and N_2O pathways were calculated separately and simultaneously. The simulated NO production was mainly via the N_2O pathway; around 90% of the reported values are formed via the N_2O pathway (for all cases). Formation of NO via this pathway is plausible under the current operational conditions [16] and similar observations for flameless combustion have been reported in the literature [70]. No prompt NO

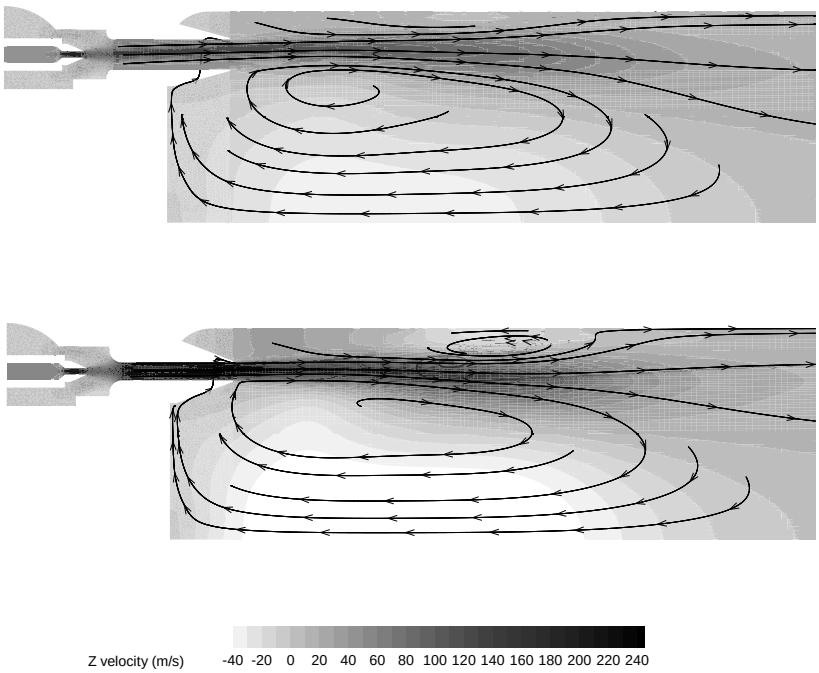

Figure 7.15: Contours of the z-velocity (m/s) with streamlines for 100n11 (top) and 100n675 (bottom) cases using the Smooke mechanism.

was formed, also previously observed [70, 139]. This was expected, since prompt NO is formed under fuel rich conditions [16]. The remaining 10% of the formed NO was via the thermal (or Zel'dovich) pathway.

7.5 Conclusions

A prototype flameless combustion gas turbine combustor was successfully fired with different LCV gases. Ultra-low emission combustion was achieved. Two visually different combustion regimes have been observed for two different inlet velocities. Clear trends have been observed for the effect of the outlet temperature, fuel composition and inlet velocity on the emissions of CO and NO. Most trends in the emission production could be explained based on the concept of flameless combustion.

The combustor has successfully been simulated with a standard set of CFD models. The simulations have been validated with measured axial mean temperature profiles.

Different turbulence models and chemistry mechanisms have been compared to get the best results. The simulations using standard Fluent mechanisms showed better axial mean temperature profiles than in the case using the more detailed Smooke mechanism. This

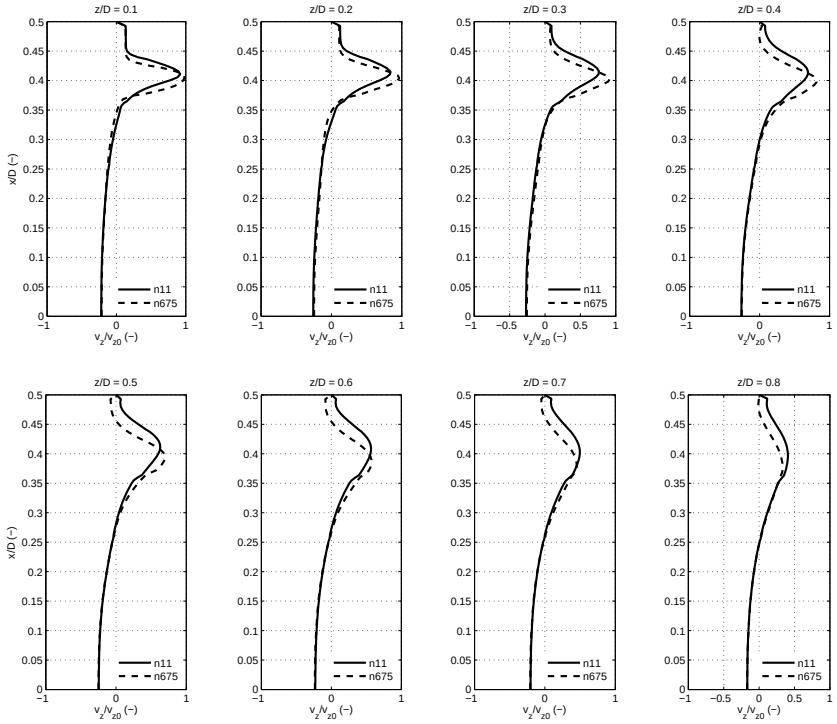

Figure 7.16: v_z/v_{z0} (-) at different distances from the burner. D is the combustion chamber diameter (156 mm), the nozzle is positioned at 0.4 x/D.

improvement turned out to be caused by flashback in the main inlet nozzle, which was not considered realistic. However, the analysis of the consequences of flashback stressed the importance of internal recirculation of flue gas. By changing the model constant $C_{\varepsilon 1}$ in the turbulence model the recirculation predictions could be significantly influenced. It was concluded that the discrepancies between the measured and simulated temperatures are within the range of uncertainty in what are optimal values of the model constants. The predicted species concentrations in the flue gas agree reasonably well with the experimental values.

Some restrictions of using standard CFD models have been encountered, e.g., CO concentration predictions and proper estimation of the internal flue gas recirculation. However, the simulations offered the opportunity to get a more detailed insight into the combustion regimes. Two different recirculation zones were identified, as has been reported earlier in the literature. From NO calculations, ultra-low emission combustion was confirmed in the simulations. It turned out that 90% of the NO was formed via the N_2O pathway and the remaining 10% via the thermal pathway.

Appendix A

Simulation fuel

In the CFD simulations of the furnaces in Chapters 4 and 6 a chemistry mechanism for the combustion of methane is used. Since in the actual (Dutch) natural gas used in the experiments also higher hydrocarbons are present, a 'simulation fuel', only containing methane as a hydrocarbon, has been calculated and used in the simulations.

For the calculation of the composition of these simulation fuels first the total heating value (ΔH [MJkg^{-1}]) of all the hydrocarbons of one kilogram of fuel is calculated with Equation A.1,

$$\Delta H = \sum_{i}^{N} \Delta H_i \, y_i \tag{A.1}$$

where N is the total number of hydrocarbons, y_i is the mass fraction of hydrocarbon i in the actual fuel [-] and ΔH_i is the lower heating value of pure hydrocarbon i [MJkg^{-1}]. It was decided to average based on the mass fractions here since the mass flow of fuel is set as a boundary condition of the simulations. For the used values of ΔH_i see Table A.1.

In the next step, the CH_4 mass fraction in one kilogram of simulation fuel is calculated,

Table A.1: ΔH_i [MJkg^{-1}] of hydrocarbons present in the natural gases [116].

Component	ΔH_i (MJ/kg)
CH_4	-50.016
C_2H_6	-47.489
C_3H_8	-46.357
C_4H_{10}	-45.742
C_5H_{12}	-45.351
C_6H_{14}	-45.105

such that this fuel has the same total heating value ΔH as the actual fuel,

$$Y_{\mathrm{CH_4}} = \frac{\Delta H}{\Delta H_{CH_4}} \tag{A.2}$$

where $Y_{\mathrm{CH_4}}$ is the CH_4 mass fraction in the simulation fuel [-].

Finally, the remaining mass content of the simulation fuel is divided over the inert species (N_2, CO_2 and O_2), weighted to their ratios as calculated from their mass fractions in the actual fuel,

$$Y_j = (1 - Y_{\mathrm{CH_4}}) \left[\frac{y_j}{\sum_j^M y_j} \right] \tag{A.3}$$

where Y_j is the mass fraction of inert species j in the simulation fuel [-], y_j is the mass fraction of inert species j in the actual fuel [-] and M is the total number of inert species.

In Table A.2 the composition of the actual fuels and their computed simulation fuels are presented. The simulation fuel of Dutch natural gas (DNG) is used in Chapter 6 and that of natural gas (NG) in Chapter 4.

Table A.2: Composition of actual and simulation fuels for Dutch natural gas (DNG, [116]) and natural gas (NG, composition supplied by supplier).

	DNG		NG	
	Actual	Simulation	Actual	Simulation
Component	%-mass	%-mass	%-mass	%-mass
CH_4	69.97	75.98	78.76	96.64
C_2H_6	4.63	-	9.61	-
C_3H_8	0.90	-	5.55	-
C_4H_{10}	0.47	-	2.89	-
C_5H_{12}	0.16	-	0.79	-
C_6H_{14}	0.23	-	0.28	-
O_2	0.02	0.02	-	-
N_2	21.52	21.87	0.43	0.68
CO_2	2.10	2.13	1.69	2.68

Finally, it is noted here that the measured mass flows of fuel and combustion air are maintained in the simulations. Therefore, the composition of the flue gases of the actual and its accompanying simulation fuel are not equal; small differences in CO_2 and O_2 contents are expected (around 0.2%-mass). However, this inaccuracy in the simulations is regarded acceptable, since the alternative would be using an extremely more extensive chemistry mechanism, which would increase the computational times far too much compared to its added accuracy.

Appendix B

Data analysis routine

The raw data output of all the measurements in and around the furnace at DUT are stored every second by a data acquisition system. In this appendix the data analysis routine, programmed in Matlab R2009b, is elucidated.

As a general first step, the beginning of a cycle was identified. Then, the data of each experiment was truncated so as to encompass a round number of entire cycles.

Mass Balance

Fuel flow

The volume flow of fuel to the burners is characterized by differential pressure measurements (Δp [Pa]) over an orifice plate at every burner. This Δp is converted to a volume flow ($\Phi^{\circ}_{\mathrm{v,fuel}}$ [$\mathrm{m^3 s^{-1}}$]) at normal conditions (T° is [273.15 K] and p° is [101325 Pa]) by the following equation,

$$\Phi^{\circ}_{\mathrm{v,fuel}} = C_j \sqrt{\Delta p} \tag{B.1}$$

where C_j is the calibrated conversion constant [$\mathrm{m^3 s^{-1} Pa^{-1/2}}$] for orifice plate j. The molar mass of the fuel (M_{fuel} [kg/mol]) is calculated by the weighted sum of all the components in Dutch natural gas (DNG, [116]),

$$M_{\mathrm{fuel}} = \sum_{i}^{N} M_i \, x_i \tag{B.2}$$

where N is the number of components in the fuel, M_i is the molar mass of component i [kg/mol] and x_i is the molar fraction of component i in DNG [-]. Then, the density ($\rho^{\circ}_{\mathrm{fuel}}$ [$\mathrm{kgm^{-3}}$]) at normal conditions is calculated with the ideal gas law,

$$\rho^{\circ}_{\mathrm{fuel}} = \frac{p^{\circ} \, M_{\mathrm{fuel}}}{R \, T^{\circ}} \tag{B.3}$$

where R is the universal gas constant (8.314472 [Jmol^{-1}K^{-1}]), T° is the reference temperature [273.15 K] and p° is the reference pressure [101325 Pa], which is equal here to the furnace pressure. Finally, the normal volume flow is converted to a mass flow ($\Phi_{\mathrm{m,fuel}}$ [kgs^{-1}]) using the normal density,

$$\Phi_{\mathrm{m,fuel}} = \Phi^{\circ}_{\mathrm{v,fuel}}\, \rho^{\circ}_{\mathrm{fuel}} \tag{B.4}$$

Combustion air flow

The volume flow of combustion air is also characterized by differential pressure measurements over orifice plates. However, since no reliable conversion constants were available, first the actual volume flow ($\Phi_{\mathrm{v,air}}$ [m^{3}s^{-1}]) is calculated with the following equation [140],

$$\Phi_{\mathrm{v,air}} = Y\, K\, A_{\mathrm{or}}\, \frac{\sqrt{(2\, \Delta p\, \rho_{\mathrm{air}})}}{\rho_{\mathrm{air}}} \tag{B.5}$$

where K is a dimensionless constant (0.65), A_{or} is the area of the orifice hole [m^2] and ρ_{air} is the density of air at actual conditions [kgm^{-3}]. The dimensionless variable Y is defined as,

$$Y = 1 - \left(\frac{1-r}{k}\right)\, \left[0.41 + 0.35 \left(\frac{d}{D}\right)^2\right] \tag{B.6}$$

where r is the ratio of the upstream and downstream pressure of the orifice plate [-], k is the ratio of C_p/C_v for air (1.4 [-]), d the diameter of the orifice hole [m] and D the diameter of the tube [m]. Subsequently, the actual flow was converted to normal conditions using the ideal gas law,

$$\Phi^{\circ}_{\mathrm{v,air}} = \Phi_{\mathrm{v,air}} \left(\frac{p_{\mathrm{air}}}{p^\circ}\right) \left(\frac{T^\circ}{T_{\mathrm{air}}}\right) \tag{B.7}$$

where p_{air} is the pressure of the air at the orifice plate [Pa] and T_{air} the temperature of the air measured directly after the air fan [K]. In these calculations the combustion air is assumed to be dry. Finally, the normal volume flow of air was converted to a mass flow ($\Phi_{\mathrm{m,air}}$ [kgs^{-1}]) in the same way as has been elaborated for the fuel flow, see above. For the molar mass of air a value of 0.0288 [kg/mol] is used based on its dry composition [141].

Flue gas flow

The actual volume flow of the flue gas leaving the furnace via the regenerators was measured. In the same location the local pressure and temperature were measured, with which the actual flow was converted to normal conditions, as in Equation B.7. Next, the normal volume flow of the flue gas is converted using the density, as in Equation B.3, which in

turn was calculated using the ideal gas law, see Equation B.2. For this, the molar mass of the flue gas (M_{flue}) had to be calculated, and thus the composition of the flue gas is required. The composition was calculated assuming complete combustion of one mole of fuel (n_{fuel} [mol]) with such an amount of air (n_{air} [mol]) that the same excess air ratio as in the experiment was achieved. The amounts of mole of the main species in the flue gas are defined in the following equations,

$$n_{\text{CO}_2} = n_{\text{fuel}} \sum_{j}^{N} x_{j,\text{fuel}}\ \xi_{\text{j,C}} + n_{\text{air}}\ x_{\text{CO}_2,\text{air}} \tag{B.8}$$

$$n_{\text{H}_2\text{O}} = n_{\text{fuel}}\ \frac{1}{2} \sum_{j}^{N} x_{j,\text{fuel}}\ \xi_{\text{j,H}} \tag{B.9}$$

$$n_{\text{O}_2} = n_{\text{fuel}}\ x_{\text{O}_2,\text{fuel}} + (\lambda - 1)\ \gamma\, n_{\text{fuel}}\ x_{\text{O}_2,\text{air}} \tag{B.10}$$

$$n_{\text{N}_2} = n_{\text{fuel}}\ x_{\text{N}_2,\text{fuel}} + n_{\text{air}}\ x_{\text{N}_2,\text{air}} \tag{B.11}$$

where n_i is the amount of species i in the flue gas [mol], N is the total number of species j in the fuel and air, $\xi_{\text{j,C}}$ and $\xi_{\text{j,H}}$ are the number of carbon or hydrogen atoms in species j, $x_{\text{O}_2,\text{fuel}}$ and $x_{\text{O}_2,\text{air}}$ the oxygen fractions in pure fuel and air [-], respectively, $x_{\text{N}_2,\text{fuel}}$ and $x_{\text{N}_2,\text{air}}$ the nitrogen fractions in pure fuel and air [-], respectively, and γ is the stoichiometric required amount of air [8.528 mol/mol] [116]. The excess air ratio (λ [-]) has been calculated from the measured oxygen concentration in the flue gas ($[\text{O}_2]$ [%-vol]) with the following equation,

$$\lambda = \frac{x_{\text{O}_2,\text{air}}}{x_{\text{O}_2,\text{air}} - [\text{O}_2]} \tag{B.12}$$

where $[\text{O}_2]$ is the molar oxygen concentration on dry basis in the flue gas. The amounts of moles are then converted to mole fractions,

$$x_i = \frac{n_i}{\sum_i^N n_i} \tag{B.13}$$

Then, using the weighted molar mass of the flue gas, the density was calculated, allowing the conversion of the normal volume flow to a mass flow of flue gas leaving the furnace via the regenerators ($\Phi^{\text{regen}}_{\text{m,flue}}$ [kgs^{-1}]).

Finally, the flue gas flow through the stack ($\Phi^{\text{stack}}_{\text{m,flue}}$ [kgs^{-1}]) was calculated by closing the total mass balance, as presented in the following equation,

$$\frac{\partial m}{\partial t} = 0 = \Phi_{\text{m,fuel}} + \Phi_{\text{m,air}} - \Phi^{\text{regen}}_{\text{m,flue}} - \Phi^{\text{stack}}_{\text{m,flue}} \tag{B.14}$$

Heat Balance

All the heat flows are calculated relative to normal conditions, i.e., at T° = 273.15 [K] and p° = 101325 [Pa].

Fuel heat flow

The heat flow of the fuel (Q_{fuel} [W]) consists of two components, the sensible heat and the chemical energy of the fuel, represented by the two terms in the square brackets in the following equation, respectively,

$$Q_{\text{fuel}} = \Phi_{\text{m,fuel}} \left[\left(c_{\text{p,fuel}}\, T_{\text{fuel}} - c^\circ_{\text{p,fuel}}\, T^\circ \right) + \Delta H_{\text{fuel}} \right] \tag{B.15}$$

where ΔH_{fuel} is the lower heating value of Dutch natural gas (38,018,007 [Jkg^{-1}]) from [116], $c_{\text{p,fuel}}$ the specific heat capacity of the fuel at actual conditions and $c^\circ_{\text{p,fuel}}$ the specific heat capacity of the fuel at normal conditions [Jkg^{-1}K^{-1}]. For the calculation of the specific heat capacities of the fuel at a certain temperature (T [K]), first, the specific heat capacity of all the components separately ($c_{\text{p},i}$ [Jkg^{-1}K^{-1}]) at this temperature T is calculated, using the following equation,

$$c_{\text{p},i} = c1 + c2 \left(\frac{\frac{c3}{T}}{\sinh(\frac{c3}{T})} \right)^2 + c4 \left(\frac{\frac{c5}{T}}{\cosh(\frac{c5}{T})} \right)^2 \tag{B.16}$$

where the constants $c1$ to $c5$ were taken for every species from [140]. Next, the total specific heat capacity is the molar weighted average of all the species,

$$c_{\text{p,fuel}} = \sum_{i}^{N} c_{\text{p},i}\, x_i \tag{B.17}$$

Combustion air heat flow

The heat flow of the combustion air is calculated with Equation B.18,

$$Q_{\text{air}} = \Phi_{\text{m,air}} \left(c_{\text{p,air}}\, T_{\text{air}} - c^\circ_{\text{p,air}}\, T^\circ \right) \tag{B.18}$$

The temperature-dependent specific heat capacity of air is calculated using the following equation,

$$c_{\text{p,air}} = \left(A + B\, T + D\, T^2 \right) E \tag{B.19}$$

where the constants A, B, D and E were taken from [142] and T is either the temperature of the air or the reference temperature. It is noted here that the regenerators are within in

the calculation domain of the mass and heat balance, and thus the (cold) air temperature before the regenerators is used.

Flue gas heat flow

The heat flow of the flue gas flows exiting via the regenerators ($Q^{\text{regen}}_{\text{flue}}$ [W]) and stack ($Q^{\text{stack}}_{\text{flue}}$ [W]) are calculated with Equation B.20,

$$Q^{*}_{\text{flue}} = \Phi^{*}_{\text{m,flue}} \left(c^{*}_{\text{p,flue}}\, T^{*}_{\text{flue}} - c^{\circ}_{\text{p,flue}}\, T^{\circ} \right) \tag{B.20}$$

where the asterisk represents either via the regenerators or via the stack, $c_{\text{p,flue}}$ is the specific heat capacity of the flue gas [Jkg^{-1}K^{-1}] and T_{flue} is the temperature of the flue gas [K]. For the temperature of the flue gas from the regenerators thermocouple measurements directly after the regenerators are used, while the general furnace temperature (T_{furn} [K]) was used as an approximate of the temperature of flue gas leaving the furnace via the stack. The specific heat capacities of the flue gas are calculated in the same way as for the fuel, using Equations B.16 and B.17. For the composition of the flue gas, again, the theoretical composition after complete combustion is used, as has been elaborated for the mass flow calculations.

Cooling tubes heat flow

The heat flow extracted by the cooling tubes is calculated by the difference in heat flow of the cooling air at the inlets and outlets of the cooling tubes,

$$Q^{*}_{\text{cool}} = \Phi^{*}_{\text{m,cool}} \left(c^{*}_{\text{p,cool}}\, T^{*}_{\text{cool}} - c_{\text{p,air}}\, T_{\text{air}} \right) \tag{B.21}$$

where the asterisk represents either upper or lower cooling tubes, T_{cool} the temperature of the cooling air at the exit of the cooling tubes [K] and $c_{\text{p,cool}}$ the specific heat capacity of the cooling air at the exit of the cooling tubes [Jkg^{-1}K^{-1}]. The total cooling air flows to the four upper and four lower cooling tubes ($\Phi^{\text{upper}}_{\text{m,cool}}$ and $\Phi^{\text{lower}}_{\text{m,cool}}$ [kgs^{-1}]) are measured separately using two thermal mass flow meters. For the temperature of the cooling air at the inlets the same temperature as for the combustion air is used (T_{air} [K]). At the outlets of all the individual cooling tubes the temperature is measured, and these temperatures are averaged for the upper and lower tubes. The specific heat capacities of the cooling air at the inlet ($c_{\text{p,air}}$ [Jkg^{-1}K^{-1}]) and outlets ($c_{\text{p,cool}}$ [Jkg^{-1}K^{-1}]) are calculated in the same way as for the combustion air, using Equation B.19. The total heat extraction of the cooling tubes is calculated by summing the heat extraction rates for the upper and lower tubes,

$$Q_{\text{cool}} = Q^{\text{upper}}_{\text{cool}} + Q^{\text{lower}}_{\text{cool}} \tag{B.22}$$

Heat losses

Finally, the unknown, or at least unquantified, heat losses (Q_{loss} [W]) are calculated by closing the overall heat balance,

$$\frac{\partial q}{\partial t} = 0 = Q_{\text{fuel}} + Q_{\text{air}} - Q_{\text{flue}}^{\text{regen}} - Q_{\text{flue}}^{\text{stack}} - Q_{\text{cool}} - Q_{\text{loss}} \tag{B.23}$$

This general heat loss term Q_{loss} includes heat losses to the environment, conduction losses, losses of hot flue gases through cracks, heat stored in the ceramic walls, to name a few.

Miscellaneous

Air momentum

The momentum flux of the combustion air jet is calculated for investigation purposes. It is assumed that exactly one-third of the total combustion air is entering via each burner. The momentum flux (G [N]) is then calculated with the following equation,

$$G = \frac{RT_{\text{preheat}}(\Phi_{\text{m,air}}^{\text{burner}})^2}{p^{\circ} M_{\text{air}} A_{\text{n}}} \tag{B.24}$$

where $\text{T}_{\text{preheat}}$ represents the measured temperature of the preheated combustion air [K], $\Phi_{\text{m,air}}^{\text{burner}}$ the mass flow of air through one burner [kgs^{-1}] and A_{n} the total area of the burner's four air nozzles [m^2]. Again, for the molar mass of air a value of 0.0288 [kg/mol] is used.

Cooling tube efficiency

For the investigation of the furnace performance the cooling tube efficiency (η_{cool} [-]) is considered. This efficiency is defined as in Equation B.25,

$$\eta_{\text{cool}} = \frac{Q_{\text{cool}}}{(Q_{\text{fuel}} + Q_{\text{air}})} \tag{B.25}$$

Emissions

The emissions of CO and NO are measured in both flue gas streams. The measurement is in ppm_v on dry basis. With the following equation these values are normalized to a theoretical content of 3%-vol of oxygen in the flue gas,

$$x_i = x_i^m \lambda \left(\frac{x_{\text{O}_2,\text{air}} - 0.03}{x_{\text{O}_2,\text{air}}} \right) \tag{B.26}$$

where x_i is the normalized mole fraction of species i [ppm$_v$@3%O_2, dry] and x_i^m the mole fraction of species i in the flue gas as measured [ppm$_v$, dry].

Temperature uniformity

The temperature uniformity (T_u [-]) is presented in the following equation, based on a definition proposed by Yang [143],

$$T_u = 1 - \sqrt{\frac{1}{N}\sum_{i=1}^{N}\left(\frac{(T_i - \bar{T})}{\bar{T}}\right)^2} \tag{B.27}$$

where N is the total number of temperature measurements positions in the furnace, T_i is the temperature in the i^{th} position and $\bar{T}$ is the mean of all the temperature measurements. The value of T_u is between 0 and 1, where the value 1 indicates a perfectly uniform furnace. In the furnace the temperature was measured with type S thermocouples in 18 different positions divided over all the furnace side walls.

Appendix C

Chemistry mechanism

In the CFD simulations the chemical mechanism for the combustion of methane developed by Smooke et al. is used [98]. This mechanism consists of 16 different species and 46 reactions. In the table below the rate coefficients of these reactions are presented. The coefficients are in the form of an Arrhenius equation,

$$k = AT^{\beta}\exp\left(\frac{E_{\mathrm{a}}}{RT}\right) \tag{C.1}$$

where k is the rate constant [kmols^{-1}m^{-3}], A is the pre-exponential factor [kmols^{-1}m^{-3}K$^{-\beta}$], T is the temperature [K], β is the power factor of the temperature [-], E_{a} is the activation energy [Jkmol^{-1}] and R is the universal gas constant (8314.472 [Jkmol^{-1}K^{-1}]).

[a]Third body efficiencies: H_2O = 21, H_2 = 3.3, N_2 = O_2 = 0.
[b]Third body efficiencies: H_2O = 6, H = 2, H_2 3.
[c]Third body efficiency: H_2O = 20.

	REACTION	A	β	E_a
(1)	$CH_4 + M \leftrightharpoons CH_3 + H + M$	1.00e14	0.000	3.5982e08
(2)	$CH_4 + O_2 \leftrightharpoons CH_3 + HO_2$	7.90e10	0.000	2.3430e08
(3)	$CH_4 + H \leftrightharpoons CH_3 + H_2$	2.20e01	3.000	3.6610e07
(4)	$CH_4 + O \leftrightharpoons CH_3 + OH$	1.60e03	2.360	3.0962e07
(5)	$CH_4 + OH \leftrightharpoons CH_3 + H_2O$	1.60e03	2.100	1.0293e07
(6)	$CH_2O + OH \leftrightharpoons HCO + H_2O$	7.53e09	0.000	6.9873e05
(7)	$CH_2O + H \leftrightharpoons HCO + H_2$	3.31e11	0.000	4.3932e07
(8)	$CH_2O + M \leftrightharpoons HCO + H + M$	3.31e13	0.000	3.3890e08
(9)	$CH_2O + O \leftrightharpoons HCO + OH$	1.81e10	0.000	1.2895e07
(10)	$HCO + OH \leftrightharpoons CO + H_2O$	5.00e09	0.000	0
(11)	$HCO + M \leftrightharpoons H + CO + M$	1.60e11	0.000	6.1505e07
(12)	$HCO + H \leftrightharpoons CO + H_2$	4.00e10	0.000	0
(13)	$HCO + O \leftrightharpoons OH + CO$	1.00e10	0.000	0
(14)	$HCO + O_2 \leftrightharpoons HO_2 + CO$	3.00e09	0.000	0
(15)	$CO + O + M \leftrightharpoons CO_2 + M$	3.20e10	0.000	-1.7573e07
(16)	$CO + OH \leftrightharpoons CO_2 + H$	1.51e04	1.300	-3.1715e06
(17)	$CO + O_2 \leftrightharpoons CO_2 + O$	1.60e10	0.000	1.7154e08
(18)	$CH_3 + O_2 \leftrightharpoons CH_3O + O$	7.00e09	0.000	1.0733e08
(19)	$CH_3O + M \leftrightharpoons CH_2O + H + M$	2.40e10	0.000	1.2055e08
(20)	$CH_3O + H \leftrightharpoons CH_2O + H_2$	2.00e10	0.000	0
(21)	$CH_3O + OH \leftrightharpoons CH_2O + H_2O$	1.00e10	0.000	0
(22)	$CH_3O + O \leftrightharpoons CH_2O + OH$	1.00e10	0.000	0
(23)	$CH_3O + O_2 \leftrightharpoons CH_2O + HO_2$	6.30e07	0.000	1.0878e07
(24)	$CH_3 + O_2 \leftrightharpoons CH_2O + OH$	5.20e10	0.000	1.4466e08
(25)	$CH_3 + O \leftrightharpoons CH_2O + H$	6.80e10	0.000	0
(26)	$CH_3 + OH \leftrightharpoons CH_2O + H_2$	7.50e09	0.000	0
(27)	$HO_2 + CO \leftrightharpoons CO_2 + OH$	5.80e10	0.000	9.5956e07
(28)	$H_2 + O_2 \leftrightharpoons 2\ OH$	1.70e10	0.000	1.9991e08
(29)	$OH + H_2 \leftrightharpoons H_2O + H$	1.17e06	1.300	1.5171e07
(30)	$H + O_2 \leftrightharpoons OH + O$	2.20e11	0.000	7.0291e07
(31)	$O + H_2 \leftrightharpoons OH + H$	1.80e07	1.000	3.6928e07
(32)	$H + O_2 + M \leftrightharpoons HO_2 + M^a$	2.10e15	-1.000	0
(33)	$H + O_2 + O_2 \leftrightharpoons HO_2 + O_2$	6.70e16	-1.420	0
(34)	$H + O_2 + N_2 \leftrightharpoons HO_2 + N_2$	6.70e16	-1.420	0
(35)	$OH + HO_2 \leftrightharpoons H_2O + O_2$	5.00e10	0.000	4.1840e06
(36)	$H + HO_2 \leftrightharpoons 2\ OH$	2.50e11	0.000	7.9496e06
(37)	$O + HO_2 \leftrightharpoons O_2 + OH$	4.80e10	0.000	4.1840e06
(38)	$2\ OH \leftrightharpoons O + H_2O$	6.00e05	1.300	0
(39)	$H_2 + M \leftrightharpoons H + H + M^b$	2.23e09	0.500	3.8744e08
(40)	$O_2 + M \leftrightharpoons O + O + M$	1.85e08	0.500	3.9982e08
(41)	$H + OH + M \leftrightharpoons H_2O + M^c$	7.50e20	-2.600	0
(42)	$H + HO_2 \leftrightharpoons H_2 + O_2$	2.50e10	0.000	2.9288e06
(43)	$HO_2 + HO_2 \leftrightharpoons H_2O_2 + O_2$	2.00e09	0.000	0
(44)	$H_2O_2 + M \leftrightharpoons OH + OH + M$	1.30e14	0.000	1.9037e08
(45)	$H_2O_2 + H \leftrightharpoons HO_2 + H_2$	1.60e09	0.000	1.5899e07
(46)	$H_2O_2 + OH \leftrightharpoons H_2O + HO_2$	1.00e10	0.000	7.5312e06

Appendix D

Combustion air water content

The water content of the combustion air was estimated, since it might have an influence on the radiative properties at high preheat temperatures. The average of the measured temperature of the cold combustion air of all the experiments, i.e., 34 °C, was used in these calculations.

First the saturated water vapour pressure (p_{sat} [Pa]) was calculated with Equation D.1 following Bolton [144],

$$p_{\text{sat}} = 611.2 \exp\left(\frac{17.67\, T_{\text{air}}}{T_{\text{air}} + 243.5}\right) \tag{D.1}$$

where T_{air} is the temperature of the combustion air [°C].

Next, using the ideal gas law, the molar fraction of water vapour is defined as in Equation D.2,

$$x_w = \frac{p_{\text{sat}}}{p - p_{\text{sat}}} \tag{D.2}$$

where x_w is the molar fraction of water vapour [-] and p is the total pressure [Pa]. The total pressure p is 101325 Pa (atmospheric) in this case.

Finally, the mole fractions were converted to mass fractions for implementation as boundary conditions in the simulations. In Table D.1 the composition of the wet combustion air at 34 °C is presented in mass percentages.

Table D.1: Composition of combustion air including water vapour at 34 °C.

Component	y_i (%-mass)
N_2	74.03
CO_2	0.04
O_2	22.43
H_2O	3.49

Appendix E

Air leakage

The furnace pressure in the KTH furnace is found to be below zero for a recurring time frame in every cycle. During these pressure dips surrounding air is sucked into the furnace through cracks, small openings and alike.

In Figure E.1 the furnace pressure is plotted for both firing modes for a period of 200 s. In both firing modes the pressure dip is directly after the switching of the burners, but in the Figure they are phased for better visibility. It is observed that in parallel mode these negative pressure peaks are significantly larger than in staggered mode.

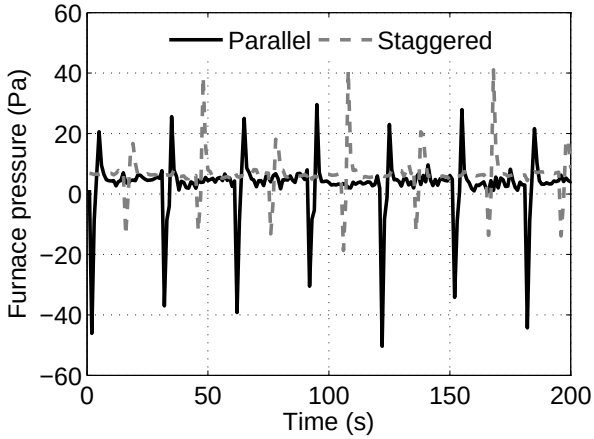

Figure E.1: Furnace (gauge) pressure (Pa) for a period of 200 s for parallel and staggered firing mode.

It is verified whether these peaks can explain the difference in the oxygen percentage between the experiments and the CFD simulations. Since the CFD simulations are steady state, these peaks (and thus the leakage) are not incorporated. From mass balance calculations it is known that an amount of around 1.9 $m_n^3 h^{-1}$ of air would compensate for the difference in the O_2 concentrations.

The expected amount of air leakage due to the pressure difference over a crack is calculated using Bernoulli's law,

$$\frac{1}{2}\rho v^2 + \rho hg + p = \text{constant} \tag{E.1}$$

where ρ is the density (kgm^{-3}), v the velocity (m/s), h the height (m), g the gravitational acceleration (ms^{-2}) and p the pressure (Pa). This equation is set up for two positions, i.e., outside the furnace wall (position a) and inside the furnace (position b). Since the total energy should be conserved the two equations should balance,

$$\frac{1}{2}\rho_a v_a^2 + p_a = \frac{1}{2}\rho_b v_b^2 + p_b \tag{E.2}$$

assuming no differences in the height. It is assumed that the surrounding air is quiescent (v_a = 0) and that the density remains constant. After rearrangement Equation E.2 is rewritten as follows,

$$v_b = \sqrt{\frac{2\Delta p}{\rho}} \tag{E.3}$$

where Δp is $p_a - p_b$. The density of the ambient surrounding air is 1.293 kg/m^3 and the Δp is estimated from Figure E.1 to be 40 Pa. This leads to a velocity v_b of around 7.9 m/s.

Subsequently, the volume flow ϕ_v^{air} (m^{3}h^{-1}) can be calculated with the following equation,

$$\phi_v^{\text{air}} = A v_b \tag{E.4}$$

where A is the area (m^2). If the area of all the cracks and openings in the furnace together measure 0.001 m^2 (e.g. an area of 4 cm by 2.5 cm), the total amount of air leakage into the furnace is 1.89 m^{3}h^{-1}. This includes the fact that the negative pressure only holds for a period of 2 seconds per cycle of 30 seconds.

Therefore, it can be concluded that the leakage of surrounding air explains the difference between the measured O_2 concentration and the O_2 concentration merely based on the comburant flows.

Bibliography

[1] C.W. Siemens. On a regenerative gas furnace, as applied to glass-houses, puddling, heating, etc. *Journal of the Franklin Institute*, 74:243–251, 1862.

[2] N. Rafidi and W. Blasiak. Thermal performance analysis on a two composite material honeycomb heat regenerators used for HiTAC burners. *Applied Thermal Engineering*, 25:2966–2982, 2005.

[3] A. Touzet, P.J. Lhomme, and A. Quinqueneau. New efficient technologies with very low NO_x emissions available for the industry: two recent examples in the French metallurgy field. In *Proceedings of the 4th High Temperature Air and Gasification Conference (HTACG)*, Rome, Italy, 26-30 November 2001.

[4] M. Flamme, M. Brune, U. Konold, A. Al-Halbouni, A. Scherello, and R. Giese. Optimization of the energy efficiency of industrial furnaces. In *Proceedings of the 4th High Temperature Air and Gasification Conference (HTACG)*, Rome, Italy, 26-30 November 2001.

[5] H. Tsuji, A.K. Gupta, T. Hasegawa, M. Katsuki, K. Kishimoto, and M. Morita. *High Temperature Air Combustion: from energy conservation to pollution reduction*. CRC Press, 2003.

[6] Y. Zel'dovich. The oxidation of nitrogen in combustion and explosions. *Acta Physiochimica U.S.S.R.*, XXI:(4), 1946.

[7] R. Weber. *The spirit of IJmuiden*. IFRF, 1998.

[8] J.A. Wünning and J.G. Wünning. Flameless oxidation to reduce thermal NO-formation. *Prog. Energy Combust. Sci.*, 23:81–94, 1997.

[9] J. Sudo and T. Hasegawa. Advanced HRS technology and its industrial applications. In *Proceedings of the 4th High Temperature Air and Gasification Conference (HTACG)*, Rome, Italy, 26-30 November 2001.

[10] S. Giammartini, G. Girardi, and A. Milani. Combustione senza fiamma: stato dell'arte in Italia. *Rassegne scientifiche e techniche*, 57:127–137, 2003.

[11] S. Kumar, P.J. Paul, and H.S. Mukunda. Studies on a new high-intensity low-emission burner. *Proceedings of the Combustion Institute*, 29:1131–1137, 2002.

[12] C. Rottier, C. Lacour, G. Godard, B. Taupin, A.M. Boukhalfa, and D. Honoré. An aerodynamic way to reach mild combustion regime in a laboratory-scale furnace. In G. Skevis, editor, *Proceedings of the 3rd European Combustion Meeting*, Chania, Greece, 11-13 April 2007.

[13] G.G. Szegö, B.B. Dally, and G.J. Nathan. Operational characteristics of a parallel jet MILD combustion burner system. *Combustion and Flame*, 156:429–438, 2009.

[14] T. Plessing, N. Peters, and J.G. Wünning. Laseroptical investigation of highly preheated combustion with strong exhaust gas recirculation. In *Proceedings of the 27th Symposium (International) on Combustion*, pages 3197–3204, Boulder, United States of America, 2-7 August 1998.

[15] P.R. Medwell, P.A.M. Kalt, and B.B. Dally. Simultaneous imaging of OH, formaldehyde, and temperature of turbulent nonpremixed jet flames in a heated and diluted coflow. *Combustion and Flame*, 148:48–61, 2007.

[16] J.A. Miller and C.T. Bowman. Mechanism and modeling of nitrogen chemistry in combustion. *Prog. Energy Combust. Sci.*, 15:287–338, 1989.

[17] I.B. Özdemir and N. Peters. Characteristics of the reaction zone in a combustor operating at mild combustion. *Experiments in Fluids*, 30:683–695, 2001.

[18] S. Murer, B. Pesenti, and P. Lybaert. Characterization of flameless combustion of natural gas in a laboratory scale furnace. In *Proceedings of the 2nd European Combustion Meeting*, Louvain-la-Neuve, Belgium, 3-6 April 2005.

[19] W. Blasiak, M. Mörtberg, N. Rafidi, N. Krishnamurthy, W. Yang, S. Kalisz, and D. Szewczyk. Study and application of high temperature air combustion for gas fuels and wastes. In *Proceedings of the 14th IFRF members' conference*, Noordwijkerhout, the Netherlands, 12-14 May 2004.

[20] F.J. Weinberg. Combustion temperatures: the future? *Nature*, 233:239–241, 1971.

[21] A. Cavaliere and M. de Joannon. Mild combustion. *Prog. Energy Combust. Sci.*, 30:329–366, 2004.

[22] A.K. Gupta. Thermal characteristics of gaseous fuel flames using high temperature air. *Journal of Engineering for Gas Turbines and Power*, 126:9–19, 2004.

[23] http://dictionary.cambridge.org/dictionary/british/flame_1, visited on February 16th, 2011.

[24] http://www.merriam-webster.com/dictionary/flame, visited on February 16th, 2011.

[25] E. Oldenhof, M.J. Tummers, E.H. van Veen, and D.J.E.M. Roekaerts. Ignition kernel formation and lift-off behaviour of jet-in-hot-coflow flames. *Combustion and Flame*, 157(6):1167–1178, 2010.

[26] E. Oldenhof, M.J. Tummers., E.H. van Veen, and D.J.E.M. Roekaerts. Role of entrainment in the stabilisation of jet-in-hot-coflow flames. *Combustion and Flame*, 158:1553–1563, 2011.

[27] R.L. Gordon, A.R. Masri, and E. Mastorakos. Simultaneous Rayleigh temperature, OH- and CH_2O-LIF imaging of methane jets in a vitiated coflow. *Combustion and Flame*, 155:181–195, 2008.

[28] D. Lupant, B. Pesenti, and P. Lybaert. Detailed characterization of flameless oxidation on a laboratory scale furnace. In G. Skevis, editor, *Proceedings of the 3rd European Combustion Meeting*, Chania, Greece, 11-13 April 2007.

[29] C. Rottier, C. Lacour, G. Godard, B. Taupin, L. Porcheron, R. Hauguel, S. Carpentier, A.M. Boukhalfa, and D. Honoré. On the effect of air temperature on mild flameless combustion regime of high temperature furnace. In *Proceedings of the 4th European Combustion Meeting*, Vienna, Austria, 14-17 April 2009.

[30] B.B. Dally, E. Riesmeier, and N. Peters. Effect of fuel mixture on moderate and intense low oxygen dilution combustion. *Combustion and Flame*, 137:418–431, 2004.

[31] H. Kobayashi, K. Oono, E.-S. Cho, H. Hagiwara, Y. Ogami, and T. Niioka. Effects of turbulence on flame structure and NO_x emission of turbulent jet non-premixed flames in high-temperature air combustion. *JSME International Journal, Series B*, 48(2):286–292, 2005.

[32] R. Weber, A.L. Verlaan, S. Orsino, and N. Lallemant. On emerging furnace design methodology that provides substantial energy savings and drastic reductions in CO_2, CO and NO_x emissions. *Journal of the Institute of Energy*, 72:77–83, 1999.

[33] R. Weber, S. Orsino, N. Lallemant, and A. Verlaan. Combustion of natural gas with high-temperature air and large quantities of flue gas. *Proceedings of the Combustion Institute*, 28:1315–1321, 2000.

[34] R. Weber. Combustion of natural gas, oil and coal with air preheated to temperatures in excess of 1000°C. In *Proceedings of the 4th High Temperature Air and Gasification Conference (HTACG)*, Rome, Italy, 26-30 November 2001.

[35] R. Weber, J.P. Smart, and W. van de Kamp. On the MILD combustion of gaseous, liquid, and solid fuels in high temperature preheated air. *Proceedings of the Combustion Institute*, 30:2623–2629, 2005.

[36] P. Pronk, P. Hoppesteyn, and B. Lewis. Application of high efficiency combustion in reheat furnaces. *STW Brandbrief*, 16:8–12, 2009.

[37] J. Engdahl, A. Lugnet, G. Moroz, and J. von Schéele. Industrial experiences from flameless oxyfuel operation in walking beam furnaces. In *AISTech 2009 Proceedings - Volume II*, 2009.

[38] W. Blasiak and H. Thunman. High temperature air combustion (HTAC) test furnace at KTH, final report. Technical Report JÄST 00/1, KTH, 2000.

[39] W. Blasiak, T. Dobski, S. Lille, M. Mörtberg, and N. Rafidi. Combustion tests in a test furnace equipped with high temperature air combustion mode. In *Proceedings of the 4th High Temperature Air and Gasification Conference (HTACG)*, Rome, Italy, 26-30 November 2001.

[40] M. Mörtberg, N. Rafidi, and W. Blasiak. Measurements of temperature, heat flux and flue gas composition in HTC flame. In *Proceedings of Challenges in Reheating Furnaces*, London, United Kingdom, 28-29 October 2002.

[41] N. Rafidi and W. Blasiak. Heat transfer characteristics of HiTAC heating furnace using regenerative burners. *Applied Thermal Engineering*, 26:2027–2034, 2006.

[42] W. Blasiak, W.H. Yang, and N. Rafidi. Physical properties of a LPG flame with high-temperature air on a regenerative burner. *Combustion and Flame*, 136:567–569, 2004.

[43] P. Hoppesteyn and M. Boss. High efficiency combustion programme development HEC phases 1 and 2 planning report. Technical Report D108/y/1, IFRF Research Station, 2002.

[44] P. Hoppesteyn, F. Frinking, and W. van de Kamp. Commissioning report HEC-EEC furnace and burners (Part 1 of 2). Technical Report C108/y/1, IFRF Research Station, 2003.

[45] J.B. Adolfi, M. Boss, and S. Santos. Commissioning report HEC-EEC furnace and burners (Part 2 of 2). Technical Report C108/y/2, IFRF Research Station, 2004.

[46] J.B. Adolfi, C. Ellul, S. Santos, F. Frinking, and P. Hoppesteyn. Experimental results from the HEC-EEC furnace and burners firing natural gas. Technical Report F108/y/2, IFRF Research Station, 2004.

[47] F. Frinking, S. Santos, and P. Hoppesteyn. LSV and LDA measurements of the HEC-EEC burners and furnace. In *Proceedings of the 14th IFRF members' conference*, Noordwijkerhout, the Netherlands, 12-14 May 2004.

[48] B.T. Burggraaf, B. Lewis, P.D.J. Hoppesteyn, N. Fricker, S. Santos, and B.K. Slim. Towards industrial application of high efficiency combustion. Technical Report K70/y/156, IFRF Research station, 2005.

[49] B.T. Burggraaf, B. Lewis, P.D.J. Hoppesteyn, N. Fricker, S. Santos, and B.K. Slim. Towards industrial application of high efficiency combustion. *IFRF Combustion Journal*, (200704), 2007.

[50] B. Pesenti, P. Evrard, and P. Lybaert. NO_x production and radiative heat transfer from an autoregenerative flameless oxidation burner. In *Proceedings of the 4th High Temperature Air and Gasification Conference (HTACG)*, Rome, Italy, 26-30 November 2001.

[51] D. Lupant, B. Pesenti, P. Evrard, and P. Lybaert. Numerical and experimental characterization of a self-regenerative flameless oxidation burner operation in a pilot-scale furnace. In *Proceedings of the 6th High Temperature Air and Gasification Conference (HTACG)*, Essen, Germany, 17-19 October 2005.

[52] D. Lupant, B. Pesenti, P. Evrard, and P. Lybaert. Numerical and experimental characterization of a self-regenerative flameless oxidation burner operation in a pilot-scale furnace. *Combustion Science and Technology*, 179:437–453, 2007.

[53] T. Ishii, C. Zhang, and S. Sugiyama. Numerical simulations of highly preheated air combustion in an industrial furnace. *Journal of Energy Resources Technology*, 120:276–284, 1998.

[54] C. Zhang, T. Ishii, Y. Hino, and S. Sugiyama. The numerical and experimental study of non-premixed combustion flames in regenerative furnaces. *Journal of Heat Transfer*, 122:287–293, 2000.

[55] T. Ishii, C. Zhang, and Y. Hino. Numerical study of the performance of a regenerative furnace. *Heat Transfer Engineering*, 23:23–33, 2002.

[56] E. Masson, D. Honoré, A. Boukhalfa, L. Porcheron, S. Maurel, F. Aguilé, P. Meunier, and A. Quinqueneau. An experimental characterization of flameless combustion at semi-industrial scale. In *Proceedings of the 14th IFRF members' conference*, Noordwijkerhout, the Netherlands, 12-14 May 2004.

[57] A. Quinqueneau, F. Aguile, L. Porcheron, A. Touzet, and F. Milcent. Flameless oxidation applied to high temperature process - overview of Gaz de France R&D activities on the subject. In *Proceedings of the 22nd World Gas Conference*, Tokyo, Japan, 1-5 June 2003.

[58] M. Flamme. Low NO_x combustion technologies for high temperature applications. *Energy Conversion and Management*, 42:1919–1935, 2001.

[59] M. Kösters, M. Flamme, A. Scherello, H. Kremer, and M. Boß. Reduction of NO_x emissions at glass melting furnaces with staged and flameless oxidation. In *Proceedings of the 4th High Temperature Air and Gasification Conference (HTACG)*, Rome, Italy, 26-30 November 2001.

[60] T. Yokomori, S. Mochida, T. Araake, and K. Maruta. Electrostatic probe measurement in an industrial furnace for high-temperature air conditions. *Combustion and Flame*, 150:369–379, 2007.

[61] P.M. Hughes, R.J. Lacelle, A. Idris, M. Legere, D. Percy, J. Wong, and T. Parameswaran. CARS and heat flux measurements in regenerative and conventional industrial-scale burners. *IFRF Industrial Combustion*, (200901), 2009.

[62] N. Krishnamurthy, P.J. Paul, and W. Blasiak. Studies on low-intensity oxy-fuel burner. *Proceedings of the Combustion Institute*, 32:3139–3146, 2009.

[63] A.F. Colorado, B.A. Herrera, and A.A. Amell. Performance of a flameless combustion furnace using biogas and natural gas. *Bioresource Technology*, 101:2443–2449, 2010.

[64] B. Danon, W. de Jong, and D.J.E.M. Roekaerts. Thermal capacity of the MEEC heat sink. Technical Report ET-2209, Delft University of Technology, 2006.

[65] B. Danon, E.-S. Cho, W. de Jong, and D.J.E.M. Roekaerts. Parametric optimization study of a multi-burner flameless combustion furnace. *Applied Thermal Engineering*, 31:3000–3008, 2011.

[66] B. Danon, E.-S. Cho, W. de Jong, and D.J.E.M. Roekaerts. Numerical investigation of burner positioning effect in a multi-burner flameless combustion furnace. *Applied Thermal Engineering (in press)*, 2011.

[67] B. Danon, A. Swiderski, W. de Jong, W. Yang, and D.J.E.M. Roekaerts. Emission and efficiency comparison of different firing modes in a furnace with four HiTAC burners. *Combustion Science and Technology*, 183(7):686–703, 2011.

[68] N. Rafidi. *Thermodynamic aspects and heat transfer characteristics of HiTAC furnaces with regenerators*. PhD thesis, Kungliga Tekniska Högskolan, 2005.

[69] T. Ishii, C. Zhang, and S. Sugiyama. Effects of NO models on the prediction of NO formation in a regenerative furnace. *Journal of Energy Resources Technology, Transactions of the ASME*, 122(1-4):224–228, 2000.

[70] D. Tabacco, C. Innarella, and C. Bruno. Theoretical and numerical investigation on flameless combustion. *Combustion Science and Technology*, 174(7):1–35, 2002.

[71] B.F. Magnussen and B.H. Hjertager. On mathematical modeling of turbulent combustion with special emphasis on soot formation and combustion. *Proceedings of the Symposium (International) on Combustion*, 16(1):719–729, 1977.

[72] P.J. Coelho and N. Peters. Numerical simulation of a mild combustion burner. *Combustion and Flame*, 124:503–518, 2001.

[73] S. Murer, B. Pesenti, and P. Lybaert. Simulation of flameless combustion of natural gas in a laboratory scale furnace. *Turkish Journal of Engineering and Environmental Sciences*, 30:135–143, 2006.

[74] C. Galletti, A. Parente, and L. Tognotti. Numerical and experimental investigation of a mild combustion burner. *Combustion and Flame*, 151:649–664, 2007.

[75] C. Galletti, A. Parente, and L. Tognotti. CFD simulations of MILD combustion. In *Proceedings of the 8th European Conference on Industrial Furnaces and Boilers*, Vilamoura, Portugal, 2008.

[76] Fluent, Lebanon - New Hampshire. *Fluent 6.3 User's Guide*, 2006.

[77] C. Duwig, R.-Z. Szasz, and L. Fuchs. Modelling of flameless combustion using large eddy simulation. In *Proceedings of ASME Turbo Expo*, number GT2006-90063, 2006.

[78] J.P. Kim, U. Schnell, and G. Scheffknecht. Comparison of different global reaction mechanisms for mild combustion of natural gas. *Combustion Science and Technology*, 180:565–592, 2008.

[79] W.P. Jones and R.P. Lindstedt. Global reaction schemes for hydrocarbon combustion. *Combustion and Flame*, 73:233–249, 1988.

[80] T. Panne, A. Widenhorn, and M. Aigner. Comparison of combustion models and reaction mechanisms for flox combustion. In *Proceedings of ASME Turbo Expo*, number GT2009-59075, 2009.

[81] A. De, E. Oldenhof, P. Sathiah, and D.J.E.M. Roekaerts. Numerical simulation of Delft-Jet-in-Hot-Coflow (DJHC) flames using the Eddy Dissipation Concept model for turbulence-chemistry interaction. *Flow, Turbulence and Combustion (in press)*, 2011.

[82] W. Yang, D. Wei, and W. Blasiak. Mathematics modeling for high temperature air combustion (HiTAC). Technical Report D 800, Royal Institute of Technology, 2003.

[83] W. Yang and W. Blasiak. CFD as applied to high temperature air combustion in industrial furnaces. *IFRF Combustion Journal*, (200603), 2006.

[84] W. Yang and W. Blasiak. Combustion performance and numerical simulation of a high-temperature air-LPG flame on a regenerative burner. *Scandinavian Journal of Metallurgy*, 33:113–120, 2004.

[85] W. Yang and W. Blasiak. Numerical simulation of properties of a LPG flame with high-temperature air. *Int. Jour. Therm. Sci.*, 44:973–985, 2005.

[86] W. Yang, M. Mörtberg, and W. Blasiak. Influence of flame configurations on flame properties and NO emissions in combustion with high-temperature air. *Scandinavian Journal of Metallurgy*, 34:7–15, 2005.

[87] Z. Rudnicki, A. Sachajdak, W. Blasiak, and W. Yang. Transient simulation of HTAC processes. In *Proceedings of 7th international symposium on High Temperature Air Combustion and Gasification (HTACG)*, Phuket, Thailand, January 13-16, 2008.

[88] R.H. Hekkens. Isothermal CFD modeling of HEC burner and furnace. Technical Report G108/y/1, IFRF Research Station, 2004.

[89] R.H. Hekkens and M. Mancini. Non-isothermal CFD model of the HEC burner and furnace. Technical Report G108/y/2, IFRF Research Station, 2004.

[90] R.H. Hekkens. Non-isothermal CFD model of the HEC burner and furnace (additional calculation). Technical Report G108/y/3, IFRF Research Station, 2004.

[91] D. Lupant, B. Pesenti, and P. Lybaert. Assessment of combustion models of a self-regenerative flameless oxidation burner. In *Proceedings of the 19th Journees d'etudes of the Belgian Section of the Combustion Institute*, Mons, Belgium, 31 May - 1 June 2006.

[92] N. Stockwell, C. Zhang, T. Ishii, and Y. Hino. Numerical simulations of turbulent non-premixed combustion in a regenerative furnace. *ISIJ International*, 41(10):1272–1281, 2001.

[93] M. Mancini, P. Swöppe, R. Weber, and S. Orsino. On mathematical modelling of flameless combustion. *Combustion and Flame*, 150:54–59, 2007.

[94] M. Mancini and R. Weber. CFD method and detailed mechanisms modelling in predicting NO_x in MILD combustion. In *Proceedings of the 7th international symposium on High Temperature Air Combustion and Gasification (HTACG)*, Phuket, Thailand, 13-16 January 2008.

[95] M. Mancini, N. Schaffel-Mancini, and R. Weber. NO_x modeling in HTAC combustion. In *Proceedings of the 8th international symposium on High Temperature Air Combustion and Gasification (HTACG)*, Poznan, Poland, 5-7 July 2010.

[96] M. Mancini, R. Weber, and U. Bollettini. Predicting NO_x emissions of a burner operated in flameless oxidation mode. *Proceedings of the Combustion Institute*, 29:1155–1163, 2002.

[97] T.-H. Shih, W. Liou, A. Shabbir, Z. Yang, and J. Zhu. A new k-ε eddy viscosity model for high Reynolds number turbulent flows. *Computers Fluids*, 24:227 – 238, 1995.

[98] M.D. Smooke, I.K. Puri, and K. Seshadri. A comparison between numerical calculations and experimental measurements of the structure of a counterflow diffusion flame burning diluted methane in diluted air. In *Twenty-First Symposium (International) on Combustion*, volume 21, pages 1783–92, 1986.

[99] I.S. Ertesvåg and B.F. Magnussen. The eddy dissipation turbulence energy cascade model. *Combustion Science and Technology*, 159:213–235, 2000.

[100] F.C. Christo and B.B. Dally. Modeling turbulent reacting jets issuing into a hot and diluted coflow. *Combustion and Flame*, 142:117–129, 2005.

[101] Ju Pyo Kim, U. Schnell, G. Scheffknecht, and A.C. Benim. Numerical modelling of mild combustion for coal. *Progress in Computational Fluid Dynamics*, 7:337–346, 2007.

[102] A. Parente, C. Galletti, and L. Tognotti. Effect of the combustion model and kinetic mechanism on the MILD combustion in an industrial burner fed with hydrogen enriched fuels. *International Journal of Hydrogen Energy*, 33:7553–7564, 2008.

[103] G.D. Stefanidis, B. Merci, G.J. Heynderickx, and G.B. Marin. CFD simulations of steam cracking furnaces using detailed combustion mechanisms. *Computers and Chemical Engineering*, 30:635–649, 2006.

[104] G.G. De Soete. Overall reaction rates of NO and N_2 formation from fuel nitrogen. In *Proceedings of the fifteenth Symposium (International) on Combustion*, volume 15, pages 1093–1102, 1975.

[105] F. Bachmaier, K.H. Eberius, and Th. Just. The formation of nitric oxide and the detection of HeN in premixed hydrocarbon-air flames at 1 atmosphere. *Combustion Science and Technology*, 7:77–84, 1973.

[106] P.C. Malte and D.T. Pratt. Measurement of atomic oxygen and nitrogen oxides in jet-stirred combustion. In *Proceedings of the fifteenth Symposium (International) on Combustion*, volume 15, pages 1061–1070, 1975.

[107] C.T. Bowman. *Fossil Fuel Combustion*, chapter Chemistry of gaseous pollutant formation and destruction. J. Wiley and Sons, 1991.

[108] B. Danon, E.-S. Cho, L. Arteaga Mendez, W. de Jong, and D.J.E.M. Roekaerts. Emission measurements in a multi-burner flox furnace. In P. Szentannai, editor, *Proceedings of the 4th European Combustion Meeting*, number 810113, pages 1–6, Vienna, 2009.

[109] B. Danon, B. Venneker, W. de Jong, and D.J.E.M. Roekaerts. Numerical analysis of a multi-burner FLOX combustion furnace at different configurations. *VDI-Berichte*, 1988:339–344, 2007.

[110] E.-S. Cho, B. Danon, L.D. Arteaga Mendez, W. de Jong, and D.J.E.M. Roekaerts. Characteristics of multi-burner positioning and operating mode in a flox furnace. In *Proceedings of the International Conference on Sustainable Fossil Fuels for Future Energy (S4FE)*, Rome, Italy, July 6-10, 2009.

[111] M.F. Modest. *Radiative Heat Transfer*. Academic press, 2nd edition, 2003.

[112] G.G. Szegö, B.B. Dally, and G.J. Nathan. Scaling of NO_x emissions from a laboratory-scale mild combustion furnace. *Combustion and Flame*, 154:281–295, 2008.

[113] A. Vouros and Th. Panidis. Influence of a secondary, parallel, low Reynolds number, round jet on a turbulent axisymmetric jet. *Experimental Thermal and Fluid Science*, 32:1455–1467, 2008.

[114] A. Sobiesiak, S. Rahbar, and H.A. Becker. Performance characteristics of the novel low-NO_x CGRI burner for use with high air preheat. *Combustion and Flame*, 115:93–125, 1998.

[115] E.W. Grandmaison, I. Yimer, H.A. Becker, and A. Sobiesiak. The strong-jet/weak-jet problem and aerodynamic modeling of the CGRI burner. *Combustion and Flame*, 114:381–396, 1998.

[116] *Physical Properties of natural gases*. Nederlandse Gasunie N.V., 1980.

[117] D.L. Baulch and D.D. Drysale. An evaluation of the rate data for the reaction CO + OH $\rightarrow$ CO_2 + H. *Combustion and Flame*, 23:215–225, 1974.

[118] S.B. Pope. Computationally efficient implementation of combustion chemistry using in situ adaptive tabulation. *Combustion Theory and Modelling*, 1:41–63, 1997.

[119] B. Danon, W. de Jong, and D.J.E.M. Roekaerts. Experimental and numerical investigation of a flox combustor firing low calorific value gases. *Combustion Science and Technology*, 182(9):1261–1278, 2010.

[120] R.L. Gordon, A.R. Masri, S.B. Pope, and G.M. Goldin. Transport budgets in turbulent lifted flames of methane autoignition in a vitiated co-flow. *Combustion and Flame*, 151:495–511, 2007.

[121] R.W. Bilger, S.H. Stårner, and R.J. Kee. On reduced mechanisms for methane-air combustion in nonpremixed flames. *Combustion and Flame*, 80:135–149, 1990.

[122] M. Mörtberg, W. Blasiak, and A.K. Gupta. Combustion of normal and low calorific fuels in high temperature and oxygen deficient environment. *Combustion Science and Technology*, 178:1345–1372, 2006.

[123] D.C. Vaz, A.R.J. Borges, J.P. van Buijtenen, and H. Spliethoff. On the stability range of a cylindrical combustor for operation in the FLOX regime. In *Proceedings of ASME Turbo Expo*, number GT2004-53790, 2004.

[124] R. Lückerath, W. Meier, and M. Aigner. FLOX® combustion at high pressure with different fuel compositions. *Journal of Engineering for Gas Turbines and Power*, 130:011505–1–7, 2008.

[125] M. Flamme. New combustion systems for gas turbines (NGT). *Applied Thermal Engineering*, 24:1551–1559, 2004.

[126] H. Schütz, R. Lückerath, T. Kretschmer, B. Noll, and M. Aigner. Analysis of the pollutant formation in the FLOX® combustion. *Journal of Engineering for Gas Turbines and Power*, 130:011503–1–9, 2008.

[127] S. Honnet and N. Peters. Simulation of pollutant formation in MILD combustion using the Eulerian Particle Flamelet Model with detailed and reduced chemistry. In G.Skevis, editor, *Proceedings of the 3rd European Combustion Meeting (ECM)*, Chania, Greece, 2007.

[128] G. Li, E.J. Gutmark, N. Overman, M. Cornwell, D. Stankovic, L. Fuchs, and M. Vladimir. Experimental study of a flameless gas turbine combustor. In *Proceedings of ASME Turbo Expo*, number GT2006-91051, 2006.

[129] C. Duwig, D. Stankovic, L. Fuchs, G. Li, and E. Gutmark. Experimental and numerical study of flameless combustion in a model gas turbine combustor. *Combustion Science and Technology*, 180:279–295, 2008.

[130] D.C. Vaz. *Towards the application of flameless combustion to micro gas turbines*. PhD thesis, Universidade Nova de Lisboa, 2007.

[131] A.W.D. Hills and A. Paulin. The construction and calibration of an inexpensive microsuction pyrometer. *Journal of Scientific Instruments*, 2(2):713–717, 1969.

[132] C.K. Westbrook and F.L. Dryer. Simplified reaction mechanisms for the oxidation of hydrocarbon fuels in flames. *Combustion Science and Technology*, 27:31–43, 1981.

[133] K. Hsu and A. Jemcov. Numerical investigation of detonation in premixed hydrogen-air mixture - assessment of simplified chemical mechanisms. Fluids 2000 conference and exhibit, American Institute of Aeronautics and Astronautics, Denver, CO, June 2000.

[134] P.J. Coelho. Accuracy issues in the modelling of radiative transfer in industrial furnaces and boilers. In *Proceedings of the 8th European Conference on Industrial Furnaces and Boilers*, Vilamoura, Portugal, 2008.

[135] P. Kutne, I. Boxx, M. Stöhr, and W. Meier. Experimental analysis of the combustion behaviour of low calorific syngas mixtures in a gas turbine model combustor. In G.Skevis, editor, *Proceedings of the 3rd European Combustion Meeting (ECM)*, Chania, Greece, 2007.

[136] M.J. Landman, M.A.F. Derksen, and J.B.W. Kok. Effect of combustion air dilution by water vapor or nitrogen on NO_x emission in a premixed turbulent natural gas flame: an experimental study. *Combustion Science and Technology*, 178:1–12, 2006.

[137] K. Hanjalic. Second-moment turbulence closures for CFD: Needs and prospects. *International Journal of Computational Fluid Dynamics*, 12(1):67–97, 1999.

[138] G. Li, B. Naud, and D.J.E.M. Roekaerts. Numerical investigation of a bluff-body stabilised nonpremixed flame with differential Reynolds-stress models. *Flow, Turbulence and Combustion*, 70:211–240, 2003.

[139] F. Donatini, M. Schiavetti, G. Gigliucci, P. Gheri, M. Monticelli, R. Mangione, A. Paulozza, and J. Riccardi. CFD simulation and experimental tests on a natural gas/hydrogen mixture-fired flameless combustor. In *Proceedings of the 8th European Conference on Industrial Furnaces and Boilers*, Vilamoura, Portugal, 2008.

[140] R.H. Perry. *Perry's Chemical Engineers' Handbook*. McGraw-Hill, seventh edition, 1997.

[141] L.P.B.M. Janssen and M.M.C.G. Warmoeskerken. *Transport phenomena data companion*. Delftse Universitaire Pers, third edition, 1997.

[142] J.M.Smith, H.C. Van Ness, and M.M. Abbot. *Introduction to Chemical Engineering Thermodynamics*. McGraw-Hill Book Company, 6th edition, 2001.

[143] W. Yang and W. Blasiak. Numerical study of fuel temperature influence on single gas jet combustion in highly preheated and oxygen deficient air. *Energy*, 30:385–398, 2005.

[144] D. Bolton. The computation of equivalent potential temperature. *Monthly Weather Review*, 108:1046–1053, 1980.

About the author

Bart Danon was born on November 10th 1978 in Delft, the Netherlands. After his secondary education at the Gymnasium Haganum in 's Gravenhage from 1991 to 1997, he started studying Chemistry at the Rijksuniversiteit Leiden. However, after one year, he decided to explore the world, and moved to Firenze (Italy) where he studied the Italian language at the Universitá degli Studi di Firenze for the period of one year. Then, he returned to the Netherlands in the fall of 1999 to continue his studies at the Rijksuniversiteit Groningen, now in the subject of Chemical Engineering. After his graduation in 2005, he started to work on his doctoral research at the Technische Universiteit Delft under supervision of Wiebren de Jong and Dirk Roekaerts, during which Bart has been selected for a visiting research project at the Kungliga Tekniska Högskolan in Stockholm, Sweden. The PhD research has partly been performed in part-time, allowing Bart to follow a three-year acting curriculum at the theatre institute de Trap in Amsterdam.

List of publications

- B. Danon, E.-S. Cho, W. de Jong and D.J.E.M. Roekaerts. Numerical investigation of burner positioning effects in a multi-burner flameless combustion furnace. *Applied Thermal Engineering* 31(17-18):3885-3896, 2011.
- E.-S. Cho, B. Danon, W. de Jong and D.J.E.M. Roekaerts. Behavior of a 300 kW_{th} regenerative multi-burner flameless oxidation furnace. *Applied Energy* 88(12):4952-4959, 2011.
- B. Danon, E.-S. Cho, W. de Jong and D.J.E.M. Roekaerts. Parametric optimization study of a multi-burner flameless combustion furnace. *Applied Thermal Engineering* 31(14-15):3000-3008, 2011.
- B. Danon, A. Swiderski, W. de Jong, W. Yang and D.J.E.M. Roekaerts. Emission and efficiency comparison of different firing modes in a furnace with four HiTAC burners. *Combustion Science and Technology* 183(7):686-703, 2011.
- B. Danon, W. de Jong and D.J.E.M. Roekaerts. Experimental and numerical investigation of a FLOX combustor firing low calorific value gases. *Combustion Science and Technology* 182(9):1261-1278, 2010.
- B. Girisuta, B. Danon, R. Manurung, L.P.B.M. Janssen, H.J. Heeres. Experimental and kinetic modelling studies on the acid-catalysed hydrolysis of the water hyacinth plant to levulinic acid. *Bioresource Technology* 99(17):8367-8375, 2008.

zie ommezijde